The Chemical and Physical Mechanisms Determining the Morphology of Wet-Chemically Etched Si(100)

by Brandon Scott Aldinger

THE CHEMICAL AND PHYSICAL MECHANISMS DETERMINING THE MORPHOLOGY OF WET-CHEMICALLY ETCHED Si(100)

A Dissertation

Presented to the Faculty of the Graduate School

of Cornell University

In Partial Fulfillment of the Requirements for the Degree of

Doctor of Philosophy

by

Brandon Scott Aldinger

August 2010

THE CHEMICAL AND PHYSICAL MECHANISMS DETERMINING THE MORPHOLOGY OF WET-CHEMICALLY ETCHED Si(100)

Brandon Scott Aldinger, Ph. D.

Cornell University 2010

Because harsh cleaning processes roughen silicon wafers, etchants that can produce smooth Si(100) surfaces have been a long-standing goal of the microelectronics industry. In this work, scanning tunneling microscopy was used to investigate the morphologies of wet-chemically-etched Si(100) surfaces, whereas the chemical composition was studied using infrared absorption spectroscopy coupled with a polarization deconvolution technique. Using this combined approach, aqueous ammonium fluoride etching of Si(100) is shown to produce near-atomically flat surfaces consisting of alternating rows of silicon dihydrides. A new assignment of the vibrational modes accounts for the presence of both strained and unstrained adsorbates on the etched surface. This smooth morphology was easily disrupted by the accumulation of hydrogen bubbles on the surface during etching. Roughening mechanisms created raised circular pillars and microfaceted etch pits if bubbles were not removed via one of several bubble-reduction techniques.

In addition, density functional theory was used to predict the vibrational modes for a variety of hydrogen-terminated silicon surfaces. The calculated mode energies highlight the sensitivity of vibrational frequencies to interadsorbate strain, though in general, the calculated frequencies were not accurate enough to predict vibrational frequencies without substantial experimental confirmation.

Lastly, the *p*H-dependence of buffered hydrofluoric acid (BHF) etching of Si(100) was examined. Below the critical *p*H of 7.8, etched surfaces became progressively rougher

and covered with hillocks, whereas surfaces etched in solutions above this *p*H exhibit no change from the flat missing-row structure. Prominent stretching modes for the BHF-etched H/Si(100) surfaces were also assigned based on trends observed in the *p*H-modified Si(100) spectra and previously well-characterized morphologies.

BIOGRAPHICAL SKETCH

Brandon Aldinger was born and raised among the suburbs and rolling farmlands of southeastern Pennsylvania. Although his early childhood is lost to the murky depths of time, it is known that he went through phases marked by obsession with construction trucks, dinosaurs, and snakes. Eventually, Brandon became broadly interested in the natural sciences, spending numerous happy Saturday mornings in the driveway melting crayons and burning tanbark with a magnifying glass. Like many future chemists, he was also fascinated by fireworks and blithely ignored the warnings against their disassembly. Brandon and his father first attempted to bond during weekend fishing trips, but managed to attract more mosquitoes than bass. Intrigued by a polished geode given to him by his grandmother, he decided to pursue rock collecting as a more promising hobby. Many trips to quarries, road cuts, and the dumps at Cornwall Iron Mine shifted Brandon's interests into geology (along with the ton of rocks that went into the basement). In 1997, his parents "persuaded" him to spend some accumulated allowance money on a 10″ telescope instead of on Legos or Super Nintendo games. After nearly freezing his fingers off viewing comet Hale-Bopp, he would spend regular observing sessions in the backyard—mostly in the summer. These two pursuits, geology and astronomy, have consumed much of his discretionary time and spending ever since.

Meanwhile, at Palmyra Area High School, a string of superb science teachers and terrible English teachers steered Brandon toward the scientific enterprise. He quickly decided upon chemistry because of its ties to both of his hobbies, its remunerative potential, and the tantalizing perk of blowing stuff up. Not realizing the difference between chemical engineering and chemistry, Brandon used the terms interchangeably on his college applications and ended up being offered a scholarship for the latter at Pennsylvania State University's Schreyer Honors College, thereby sealing his fate.

During undergraduate research at Penn State, an incident with a loose condenser hose and SO_2 inhalation convinced him that his happiness and life expectancy would be greater after bidding organic chemistry a misty-eyed farewell (SO_2 also causes eye irritation). An exploratory tour through the PSU labs revealed that chemistry could be done with wrenches rather than test tubes, and he joined a physical chemistry group his sophomore year. Many hours struggling with a 1970s-era chamber in the A. Will Castleman Jr. lab taught Brandon the fundamentals of vacuum technology and mass spectrometry. An unfortunately-timed move to a new building cut short his dreams of publishing while at Penn State, but did provide him with many odd jobs of plumbing, wiring, and interior decoration.

After visiting graduate schools during a hectic senior year, Brandon decided to attend Cornell University in Ithaca, NY. In his new apartment, he eventually experienced several plagues of biblical proportions, ranging from a millipede infestation and an invasion of wild turkeys, to a slightly unhinged hippie taking up residence in the parking lot. Through it all, Brandon worked diligently towards his Ph.D. in the lab of Melissa A. Hines. While pursuing his chemistry doctorate, he simultaneously earned the degree of Jedi Master by machining six lightsaber hilts (seven, if you count the toddler-sized saber he made for a baby shower).

Job applications and thesis work swelled to fill most of 2010, culminating in a successful B-Exam in July. Within the next few months, Brandon will begin a new life as part of what he affectionately calls "the real world."

ACKNOWLEDGMENTS

I would first like to thank my adviser, Melissa A. Hines, for her guidance and ingenuity over the course of my Cornell career. My coworkers, Ian "Highly Non-ideal" Clark, Ankush "My Heart Will Go On" Gupta, and Marc "Mama Mia!" Faggin, were an integral part of this experience. Together, we navigated the rocky shores of STM repair, REU training, and the purchasing department. I also wish to thank Sned and Nate, the two guardians of the machine shop during my time at Cornell, for humoring many strange questions regarding the esoteric aspects of lightsaber manufacture. Richard Hennig, professor and burgeoning rock hound, also deserves my gratitude for training me in the ways of DFT, as does the silicon-surface pioneer, Yves Chabal, for allowing me to work in his lab during August 2009.

The Graduate Christian Fellowship has been an important source of personal growth for me while in Ithaca. Ray, Heather, Kristina, Vince, Steve K., Steve H., Joanna, Becky, Phil, Emily, and Heidi are only some of my good GCF friends who I will dearly miss. I also look back with fondness on the clear, cold Friday nights spent on the windy roof of Fuertes Observatory. Astronomy club members came and went, but Art, Mike, and Shianne stuck with it for the long haul.

My parents, though separated from me by ~222 miles, were still very much a part of my career, both through their encouragement and the frozen dinners schlepped up from home. Finally, I believe that God brought me to Cornell for a reason. In the years to come, I hope to understand more of that purpose as I reflect on my time in Ithaca and all the people I met here.

TABLE OF CONTENTS

LIST OF FIGURES

LIST OF TABLES

Chapter 1

Introduction

Silicon plays an indispensable role in our high-technology society. From computer chips to solar cells to microelectromechanical systems, silicon has retained its dominance as the substrate of choice for almost all electronic devices. Despite this history of success, new technological hurdles inevitably arise as silicon-based devices are forced to become simultaneously smaller, cheaper, and more efficient.[1] Although the purity of commercial silicon crystals is almost indistinguishable from 100%, the very act of cutting the silicon crystal, along with subsequent processing steps, introduces harmful roughness and contamination that can degrade the performance of an electronic device. For that reason, the surface chemistry of silicon, especially the cleaning and etching chemistry, continues to be of the utmost importance.

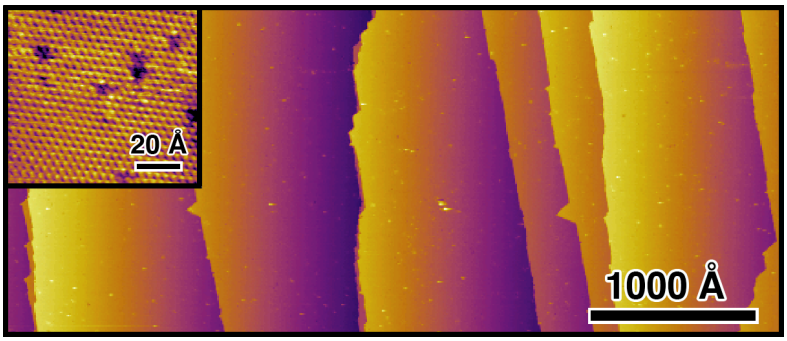

Figure 1.1. STM image of a Si(111) surface etched for 8 min in 40% $NH_4F(aq)$, which has atomically flat terraces terminated by an ideal monolayer of silicon monohydrides. The inset of an atomically-resolved portion of a terrace shows the arrangement of monohydrides on the Si(111) crystal face.

Of the major silicon faces, the (111) face has received the most attention from academic researchers. In 1989, researchers conclusively showed that Si(111) etched in a

fluoride-based solution was passivated with a monolayer of hydrogen—not fluorine-terminated as originally thought.[2] Moreover, the etched Si(111) surface was ideally H-terminated with atomically flat terraces, as shown by the scanning tunneling microscope (STM) images in Fig. 1.1. This discovery opened the door for a flurry of spectroscopic studies analyzing the characteristic vibrations of silicon hydrides,[3] which could be used to decipher the morphology of etched surfaces. Soon, other aqueous etchants were shown to produce atomically-flat Si(111) surfaces, leading to a large body of work focused on understanding the etching mechanisms that influence the relative smoothness of the (111) surface.

In contrast, the wet-chemical etching of Si(100) is less well understood than Si(111), even though Si(100) is the basis for virtually all microelectronic devices.

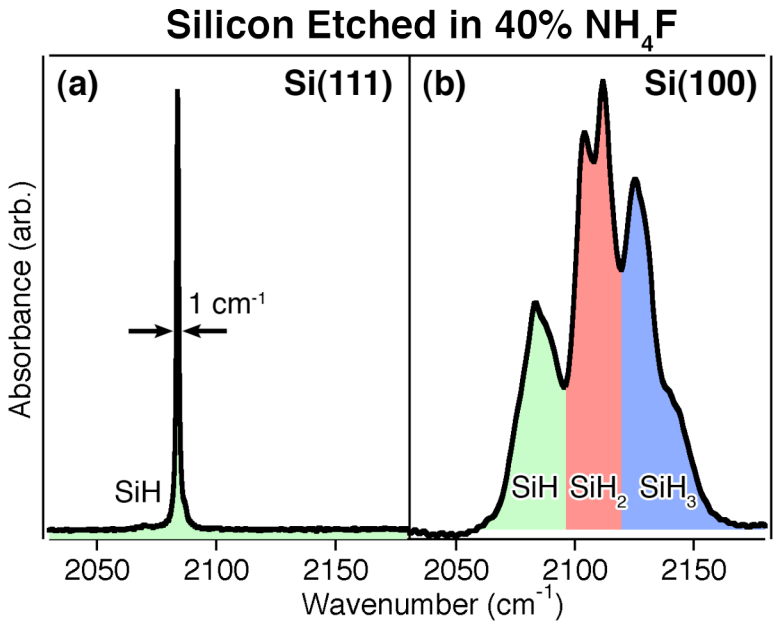

Figure 1.2. Infrared absorbance spectra (*p*-polarization) in the Si–H stretching region for hydrogen-terminated (a) Si(111) and (b) Si(100) surfaces etched in 40% $NH_4F(aq)$. Note the single, extremely narrow monohydride stretch mode observed for Si(111). In the Si(100) spectrum, the regions previously assigned to monohydrides (SiH), dihydrides (SiH_2), and trihydrides (SiH_3) are indicated with green-, red-, and blue-filled areas, respectively.

Researchers who studied etched Si(100) were confronted by images of rough surfaces[4] and absorbance spectra with vibrational modes that were much broader and more complicated than those of etched Si(111).[5] The same etchants that produced flat Si(111) with only one Si–H stretching mode resulted in Si(100) surface spectra with extremely broad, overlapping bands, as illustrated in Fig. 1.2. The broad modes of etched Si(100) surface spectra were attributed to a mixture of silicon hydrides. The spectra were divided into three regions of increasing energy assigned to monohydrides, dihydrides, and trihydrides, as shown in Fig. 1.2(b).[6] Coupled with inferences drawn from Si(111) surface spectra, the band broadness of etched Si(100) was interpreted as a sign of extreme roughness. The prevailing ideas about Si(100) etching were first posited in a few early influential studies, which quickly led to the acceptance of three rules of thumb: First, Si(100) surfaces are rough at all stages of aqueous etching. Second, Si(100) surfaces develop {111} facets with increasing etch times.[5] Third, the broadness and multiple absorption bands of H/Si(100) infrared absorbance spectra are evidence of surface roughness.

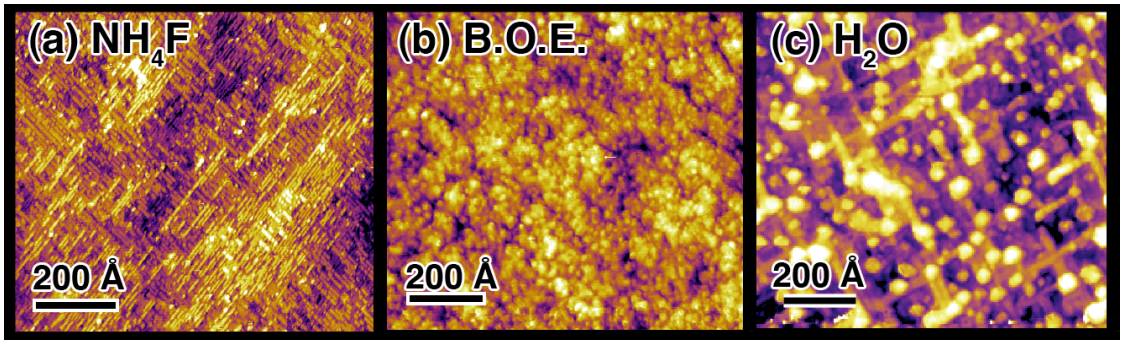

Figure 1.3. STM images for three well-characterized Si(100) morphologies produced by etching with (a) ammonium fluoride [$NH_4F(aq)$], (b) buffered oxide etchant (BOE), and (c) water.

Ironically, in the course of searching for an etchant that *roughened* Si(100), it was found that Si(100) surfaces etched in 40% $NH_4F(aq)$ were *smoother* than any wet-

chemically etched Si(100) surface previously published in the literature. This system, described in Chapter 3, broke all three "rules" mentioned above. Surface morphologies observed with STM conclusively showed that the etched surface was quite flat and displayed a missing-row morphology with significant long-range order, as illustrated in Fig. 1.3(a). Even though the infrared absorbance spectrum in the Si–H stretching region was indeed quite broad, only 3-4 atomic layers were exposed over areas of 1000 Å × 1000 Å, and no faceted hillocks or pits were observed. Instead, the broadness of the absorbance modes was attributed to variations in the local structure of the missing-row morphology (*e.g.,* point defects) and not surface roughness. A new spectral deconvolution technique, summarized in Chapter 2, was developed to separate the Cartesian components of the polarized infrared spectrum, which greatly reduced spectral congestion and simplified interpretation of the vibrational modes. This deconvolution procedure enabled new mode assignments for the complex NH_4F-etched Si(100) surface spectrum.

The discovery of near-atomically-flat Si(100) produced by NH_4F(*aq*) etching revealed that much of the conventional wisdom about Si(100) etching was incorrect; however, numerous reports in the literature of {111} microfaceting during etching demanded an explanation. Chapter 4 describes how an extremely anisotropic etchant such as NH_4F(*aq*), which produced smooth Si(100) surfaces at short etch times, could also dramatically roughen a silicon surface. Hydrogen gas bubbles, a byproduct of etching, accumulated on the surface of a sessile sample, leading to a complex variety of morphological features on several length scales. The dark field micrograph in Fig. 1.4 shows one example of a Si(100) surface roughened by bubble formation during etching. This roughening process, though not inherent to the etchant itself, produced numerous {111}-faceted, micron-scale etch pits after longer etch durations—pits that could explain the observations of roughness made by other researchers. A few simple modifications to

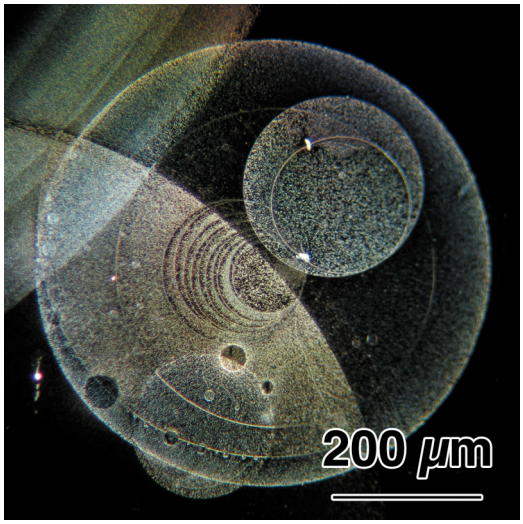

Figure 1.4. Dark-field micrograph of Si(100) etched for 1 hr in quiescent $NH_4F(aq)$. The bright regions indicate areas of surface roughness.

the etching procedure effectively removed bubbles and extended the etch time of Si(100) in $NH_4F(aq)$ out to almost an hour without the formation of {111} facets.

In addition to experiment, theoretical studies also played an important role in establishing the previous interpretation of the vibrational spectra of wet-chemically etched Si(100). Cluster calculations on trisilane were originally used to confirm the vibrational mode assignments for Si(100) surfaces etched in HF.[6] The simple trisilane molecule, however, did not include the possibility of interadsorbate strain. In fact, later slab calculations predicted that the dihydrides on an ideally hydrogen-terminated Si(100) surface distort to relieve surface strain,[7] causing huge shifts in the vibrational frequencies.[8] Still, direct comparison of theoretical vibrational mode predictions to H/Si(100) surfaces was limited by the incomplete knowledge of wet-chemically etched Si(100) surface morphologies. The advances described above on $NH_4F(aq)$-etched Si(100) finally provided a well-defined surface structure amenable to vibrational frequency calculation. Chapter 5 reports density functional theory (DFT) calculations of vibrational frequencies for the "missing-row" Si(100) morphology, as well as for the test cases of bulk-terminated

Si(100), flat Si(111), and stepped Si(111). The results for these systems show that DFT calculations can *confirm* mode assignments, but they are not yet accurate enough to be *predictive* for highly-strained, H/Si(100) morphologies. Relative trends, such as the effects of strain relaxation or varying step size, can be inferred, albeit with some caution.

Although the work outlined above focuses on *p*H 7.8 NH_4F-etched Si(100), low *p*H, fluoride-based etchants are also commonly used in industrial cleaning processes.[1] These etchants produce very different morphologies from pure NH_4F. For example, the STM image in Fig. 1.3(b) shows the rough and hillock-covered Si(100) morphology produced by *p*H 5 buffered hydrofluoric acid (buffered oxide etch, or BOE). To explore the behavior of these solutions, the *p*H dependence of Si(100) etching in buffered hydrofluoric acid (BHF) was examined. As described in Chapter 6, a transition from smooth to roughened morphologies was observed for BHF at *p*Hs < 7.8, which led to progressively rougher Si(100) surfaces characterized by hillocks with significant {111}- and {110}-microfaceted character. In contrast, Si(100) surfaces etched with BHF above *p*H 7.8 retained the near-atomically-flat "missing-row" morphology produced by pure NH_4F.

Chapter 6 draws on accumulated spectral data of etched Si(100) surfaces to assign the stretching modes of *p*H-modified, BHF-etched Si(100). In addition to the $NH_4F(aq)$-etched Si(100) surfaces described in Chapter 3, H_2O etching of Si(100) has also been previously investigated.[9] Water-etched Si(100) surfaces have well-defined, faceted hillocks connected by stripes, as shown in Fig. 1.3(c). Polarized infrared spectroscopy of the surface morphologies in Fig. 1.3 has revealed several SiH_X absorbance modes that are unique to H/Si(100) surfaces, as well as modes previously observed on etched Si(111) and Si(110). Knowledge of the characteristic absorbance modes for H/Si(100) surface adsorbates can provide quick insight into the surface morphology of novel etched Si(100) surfaces.

Finally, the importance of sample preparation techniques and chemical purity is often taken for granted, but experience has shown that extreme attention to cleanliness is necessary for the success of silicon etching experiments. For that reason, sample cleaning and preparation is extensively described in Chapter 2 and at the beginning of each chapter.

In summary, this work expands on the fundamental knowledge of Si(100) etching and corrects several widely-held misconceptions. The (100) face of the silicon crystal lattice is perhaps the most economically-important surface today. Because the techniques that are used to control and process Si(100) have become more refined, accurate knowledge of Si(100) surface chemistry and analysis is crucial for reducing defects that affect highly-designed devices. This thesis builds on the insights of previous researchers and attempts to take the first steps towards a unified understanding of wet-chemically etched H/Si(100) surfaces.

REFERENCES

[1] W. Kern, in *Handbook of Silicon Wafer Cleaning Technology*, 2nd ed., edited by K. A. Reinhardt and W. Kern (William Andrew Inc., 2008), p. 3-92.

[2] G. S. Higashi, Y. J. Chabal, G. W. Trucks, and K. Raghavachari, Applied Physics Letters **56,** 656-658 (1990).

[3] Y. J. Chabal and K. Raghavachari, Surface Science **502,** 41-50 (2002).

[4] U. Neuwald, H. E. Hessel, A. Feltz, U. Memmert, and R. J. Behm, Surface Science **296,** L8-L14 (1993).

[5] P. Dumas, Y. J. Chabal, and P. Jakob, Surface Science **269/270,** 867-878 (1992).

[6] Y. J. Chabal, G. S. Higashi, K. Raghavachari, and V. A. Burrows, Journal of Vacuum Science & Technology A: Vacuum, Surfaces, and Films **7,** 2104-2109 (1989).

[7] S. Ciraci, R. Butz, E. M. Oellig, and H. Wagner, Physical Review B **30,** 711-720 (1984).

[8] U. Freking, P. Krüger, A. Mazur, and J. Pollmann, Physical Review B **69,** 035315-1 - 035315-11 (2004).

[9] M. F. Faggin, S. K. Green, I. T. Clark, K. T. Queeney, and M. A. Hines, Journal of the American Chemical Society **128,** 11455-11462 (2006).

Chapter 2

Experimental and Computational Methods

2.1. Silicon sample preparation

Samples used for scanning tunneling microscopy (STM) experiments were prepared from 100-mm-diameter, single-side-polished, 475-500 μm-thick, 0.5-10 Ω cm, Czochralski silicon wafers. Moderately-doped silicon was needed to obtain sufficient tunneling currents for imaging. In contrast, samples for infrared absorption experiments were prepared from 100-mm-diameter, 500-μm-thick, double-side-polished, high resistivity (>1000 Ω cm), float-zone silicon wafers to minimize free carrier absorption and absorption by oxygen impurities.

To ensure a clean, flat, and reproducible starting surface, all silicon wafers were oxidized at high temperature in a tube furnace before dicing. Wafers were first cleaned with a standard RCA process[1] and then exposed to 1 atm of O_2 (*g*) for 30 min at 1100ºC. These conditions produced a 1000-Å-thick layer of SiO_2 that engulfed residual surface defects and contamination. The Si/SiO_2 interface was subsequently smoothed by annealing the wafers in a N_2 atmosphere for 30 min at 1100ºC.[2,3]

In preparation for dicing, a solid thermoplastic adhesive (Crystalbond 509, Aremco Products Inc.) was used to bond the oxidized Si wafer to a ¼″-thick glass plate that was itself bonded to a steel plate. The exposed surface of the wafer was also covered with a thin layer of adhesive to protect the surface from damage and contamination during dicing. The wafer/glass/steel stack was then magnetically clamped to a table saw and cut in the appropriate pattern with a diamond blade. Samples for STM analysis were cut into 0.6″ × 0.7″ rectangles, and infrared absorption samples were diced as shown in Fig. 2.1. The infrared absorption spectra of Si(100) and Si(111) are independent of azimuthal orientation. For low symmetry surfaces, such as Si(110) or vicinal Si(100), two

separate wafers were diced in orthogonal directions as shown in Fig. 2.1(b) to obtain complete spectroscopy data.

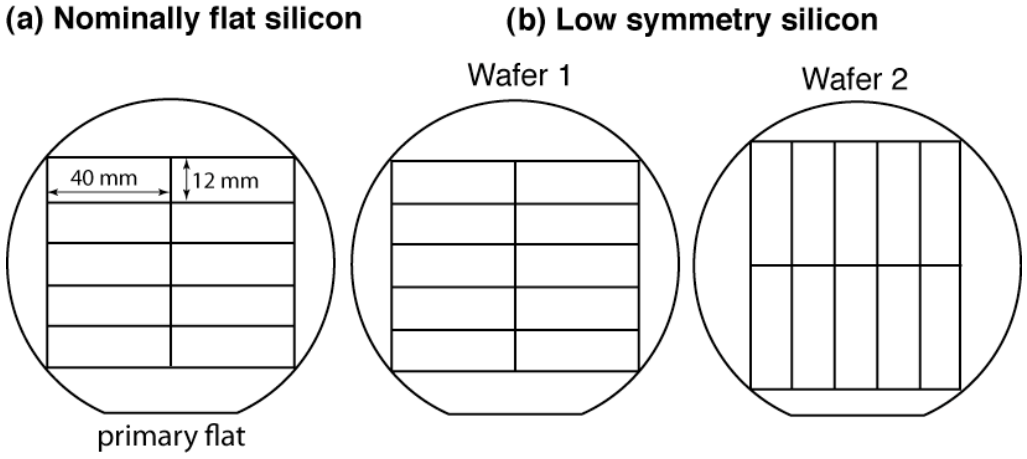

Figure 2.1. Dicing pattern for infrared absorption samples cut from 100 mm wafers for (a) high-symmetry wafers [*e.g.* nominally flat Si(100)], and (b) low-symmetry wafers [*e.g.* miscut Si(100)]. In the case of (b), two separate wafers were diced in orthogonal directions.

A dedicated wafer saw was sometimes used to dice samples instead of the diamond saw. In that case, the oxidized wafer was affixed to a removable plastic film and diced using a wafer saw (K&S 7100 dicing saw) equipped with a blade specifically designed for cutting silicon (S1235 blade). After dicing, the samples were removed by peeling away the film. This method eliminated the need for an adhesive, reducing the possibility of organic contamination and simplifying the cleaning steps. The wafer saw did not chip the cut edges as much as the diamond saw, resulting in cleaner cuts and less particulate debris.

Diced samples for multiple-internal-reflection (MIR) experiments were polished on both short ends so that the resulting sample had a trapezoidal cross-section as depicted in Figure 2.2. First, the rectangular samples were glued with the thermoplastic adhesive to a custom-machined, stainless-steel chuck that held the short edge of the

samples at 45º with respect to the polishing surface. Stacking multiple samples on top of one another in the chuck decreased the risk of sample breakage during polishing and reduced the polishing time per sample. A stack of four samples was found to balance risk of breakage with efficiency. Using a grinder-polisher (Buehler, Metaserv), the narrow ends of the samples were polished sequentially with 320-grit sandpaper, 600-grit sandpaper, 3 μm alumina polishing slurry, and 0.05 μm polishing slurry (Buehler, Micropolish). Alternatively, a good polish could be obtained with 600-grit sandpaper followed by a 1 μm polishing slurry. After one edge was polished, the chuck was heated to loosen the adhesive, and the samples were rotated by 180º, exposing the opposite (unpolished) edge to the polishing pad. The polishing procedure was then repeated.

Diced samples for both STM and infrared absorption experiments were stored with the adhesive layer intact, which protected the surface from mechanical damage. Shortly before an experiment, the adhesive was removed by soaking the sample in acetone for several hours.

Because STM experiments are extremely sensitive to contamination, the samples were subjected to an additional three-step cleaning process. The samples were first immersed in a crystallization dish containing trichloroethylene (TCE), covered with a watch glass, and heated to a gentle boil (about 40ºC) on a hot plate for 10 min. After cooling, the samples were immersed sequentially in acetone and methanol for 10 min each, then rinsed with water.

2.2. Silicon cleaning

The labware used for sample preparation was cleaned before each experiment with a standard RCA clean.[4] All labware was composed of solid glass or Teflon and was stored under water between experiments to minimize contamination.

Silicon samples were cleaned immediately before each experiment with a modified RCA clean. First, the sample was rinsed with ultrapure water (Millipore, Milli-Q) and then

immersed in a basic peroxide solution (referred to as SC1) consisting of 12 M $NH_4OH(aq)$ (EMD Chemical, ACS-grade), 30% H_2O_2 (J. T. Baker, CMOS grade) and ultrapure water in a 1:1:5 ratio by volume. The SC1 solution was then heated in an 80ºC water bath for 10 min, removing particulates and residual organic contamination from the sample.[1] Next, the sample was thoroughly rinsed in ultrapure water and then immersed in an acidic peroxide solution (SC2) composed of a 1:1:5 ratio by volume of 13 M HCl (*aq*) (J.T. Baker, ACS grade), 30% H_2O_2, and ultrapure water. The SC2 solution was then heated in an 80ºC water bath for 10 min to remove metallic contaminants. The sample was then rinsed in ultrapure water before etching as described in subsequent chapters.

2.3. Fourier transform infrared spectroscopy

Infrared absorption spectroscopy is a powerful surface analysis tool that is sensitive to the chemical identity of adsorbates and their orientations. Under some conditions, polarized infrared spectroscopy can even elucidate the morphology of etched surfaces. The vibrational modes of H-terminated silicon were studied using two different experimental geometries to measure both the Si–H stretching region (~2060-2160 cm^{-1}) and lower frequency Si–H scissor and wagging vibrational modes (~600-1000 cm^{-1}).

2.3.1. Multiple internal reflection

One of the primary challenges to obtaining high-quality spectra of surface monolayers is the small number of molecules probed, especially in comparison to bulk samples. In contrast to a single-pass transmission geometry, the multiple-infrared-reflection geometry improves the sensitivity to surface adsorbates while also enabling high surface elecric fields in all three principle directions (*x*, *y*, and *z*). The multiple-internal-reflection (MIR) geometry improves signal-to-noise ratios by roughly an order of magnitude compared to a single-pass transmission experiment.[5] In the MIR apparatus used for this work, light from the infrared source was focused at normal incidence upon a trapezoidal silicon sample as shown schematically in Fig. 2.2. Light that entered the

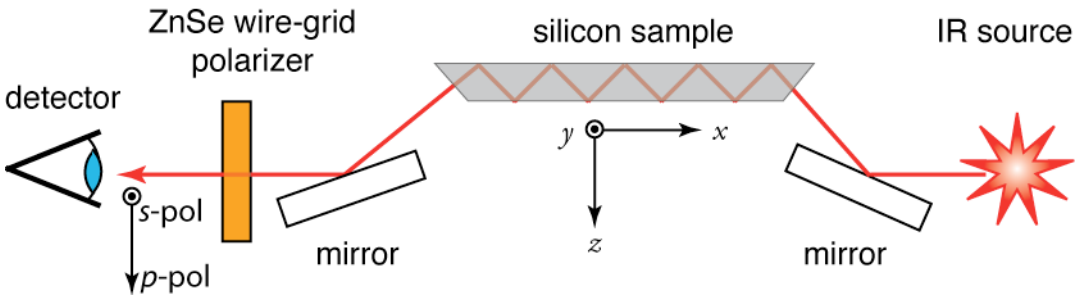

Figure 2.2. Schematic of MIR geometry. Not to scale.

beveled faces was totally internally reflected, interacting with the transition dipoles of the surface adsorbates at each reflection from the surface. Approximately 75 reflections occurred for the 40 mm long × 0.5 mm thick (1.5″ × 0.02″) samples used in these experiments. After exiting the sample through the opposite face, the infrared beam passed through a ZnSe holographic wire-grid polarizer (Molectron Inc.). Two polarizer orientations were used for each sample: one orientation transmitted the component of the electric field polarized in the plane of incidence (*p*-polarization) and the other transmitted the component polarized normal to the plane of incidence (*s*-polarization). A liquid-nitrogen-cooled, mercury-cadmium-telluride (MCT) detector (MCT-A with CdTe window, Thermo Fisher, Inc.) was used to detect the transmitted radiation.

2.3.2. Transmission spectroscopy

Although the MIR geometry offers increased sensitivity relative to a single-pass transmission geometry, multiphonon absorption bands dominate the spectrum below about 1500 cm^{-1} for long samples, such as the 40-mm-long samples used in these experiments. To study vibrational modes in the 600-1500 cm^{-1} range, the transmission geometry shown in Fig. 2.3 was used. To obtain spectra with significant perpendicular and in-plane intensity, two sample orientations were used with ϕ = 74° and 30°, respectively. At ϕ = 74°, the Brewster angle for silicon, transmitted *p*-polarized light has a

significant perpendicular component.[6] Spectra were also collected at the angle of 30° to obtain in-plane polarized radiation. (Normal incidence was not used because of interference from internal reflections between the parallel sample faces.) A ZnSe polarizer was used to select the desired polarization. For transmission experiments, a MCT-B detector with KRS-5 windows (Thermo Fisher, Inc.) was used to maximize sensitivity in the 600-650 cm^{-1} range typical of Si-H bending modes.

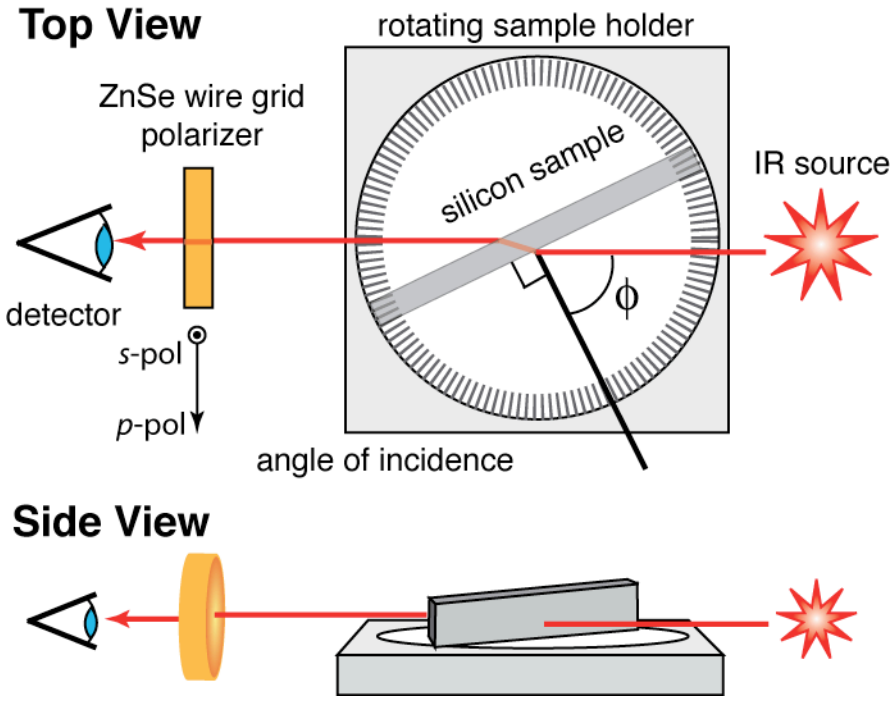

Figure 2.3. Schematic of transmission FTIR setup, where ϕ is the angle of incidence measured from the surface normal. Not to scale.

2.4. Spectral deconvolution

The interpretation of surface infrared absorption spectra can be hindered by the presence of many overlapping modes. A mathematical deconvolution technique was used to transform infrared spectra from the experimental reference frame, which was defined by the surface electric field during irradiation with both *p*- and *s*-polarized light, to a

Cartesian reference frame defined by the surface normal and the plane of incidence. In some cases, the transformation resulted in significant spectral simplification.

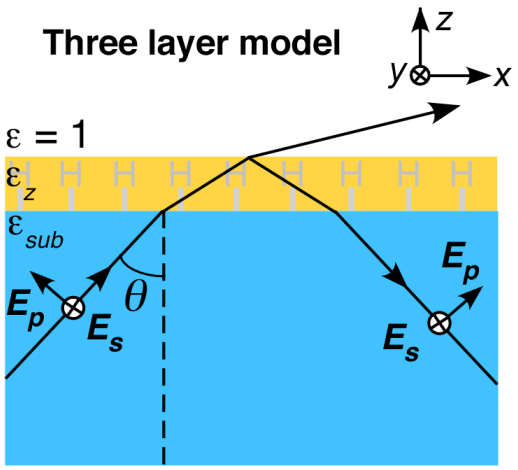

Figure 2.4. The three-layer model used to calculate the electric fields at the adsorbate. The transmitted ray is shown for clarity; however, this field is evanescent in total internal reflection.

2.4.1. Electric field at the adsorbate

The three-layer model, sketched in Figure 2.4, was used to estimate the local electric field in the adsorbate layer. In this model, the substrate and vacuum are treated as homogeneous, dielectric media, and the adsorbate layer is treated as a thin uniform dielectric medium.[5,7] First, the electric field on the substrate side of the substrate/adsorbate interface is determined using classical electrodynamics. When the electric field of incident radiation is *p*-polarized, this field has components parallel, $E_{\parallel}^{0}$, and perpendicular, $E_{\perp}^{0}$, to the surface. When the electric field of the incident radiation is *s*-polarized, the electric field on the substrate side of the surface/adsorbate interface, E_{s}^{0}, is entirely parallel to the surface. From Reference 5, these fields are

$$(2.1) \qquad \left|E_{\parallel}^{0}\right| = 2\cos\theta\sqrt{\frac{\sin^{2}\theta - 1/\varepsilon_{sub}}{\left(1-1/\varepsilon_{sub}\right)\left[\left(1+1/\varepsilon_{sub}\right)\sin^{2}\theta - 1/\varepsilon_{sub}\right]}}E_{inc}\,(p\text{-polarization}),$$

(2.2) $$\left|E_{\perp}^{0}\right| = \frac{2\varepsilon_{sub}\cos\theta\sin\theta}{\sqrt{\left(1-1/\varepsilon_{sub}\right)\left[\left(1+1/\varepsilon_{sub}\right)\sin^{2}\theta - 1/\varepsilon_{sub}\right]}} E_{inc}\,(p\text{-polarization}),\ \text{and}$$

(2.3) $$\left|E_{s}^{0}\right| = \frac{2\cos\theta}{\sqrt{1-1/\varepsilon_{sub}}} E_{inc}\,(s\text{-polarization}),$$

where ε_{sub} is the relative dielectric constant of the substrate, E_{inc} is the magnitude of the incident electric field, and θ is the angle of incidence.

The electric fields within the adsorbate layer can be defined in terms of E^{0} using the boundary conditions at the substrate/adsorbate interface. Boundary conditions require the parallel components of the electric field and the perpendicular components of the displacement field to be continuous across the interface, which can be used to determine the electric fields in the adsorbate layer. In the limit of an adsorbate layer much thinner than the wavelength of the irradiating light, the electric fields in the adsorbate layer for *p*-polarized radiation are

(2.4) $$E_{\parallel} = E_{\parallel}^{0} \quad \text{and}$$

(2.5) $$E_{\perp} = \frac{1}{\varepsilon_{z}} E_{\perp}^{0},$$

where ε_{z} is the z-component of the adsorbate dielectric tensor, which is assumed to be diagonal. For *s*-polarized radiation, the electric field in the adsorbate is

(2.6) $$E_{s} = E_{s}^{0}.$$

The limitations to the three-layer model have been reviewed by Feibelman.[8] Two potential problems have been raised. First, the sharp interfaces in the three-layer model imply discontinuities in the z-component of the electric field. In turn, the electric field discontinuity at the substrate/adsorbate interface implies the existence of bound charge

localized on a sub-atomic length scale, which is unphysical. The appropriate position for the discontinuity is also unclear. Second, the three-layer model assumes an entirely local relationship between the electric field and the displacement field, whereas in fact, the local displacement field is affected by the electric field at neighboring points during previous times. After assessing these concerns, Feibelman concluded that the model adequately approximated surface electric fields when the absorption of the adsorbate layer is small and the probing frequencies are well below the plasma frequency of the substrate. These conditions are met for infrared spectroscopy of silicon surfaces.

2.4.2 Absorbance on surfaces with no inherent symmetry

For one internal reflection, the absorbance of the adsorbate layer, A_{ads} can be expressed as

$$A_{ads} = a\left(\vec{E} \bullet \vec{\mu}\right)^2, \tag{2.7}$$

where a is a constant, and $\vec{\mu}$ is the transition dipole of the adsorbate. In the multiple internal reflection geometry, the total absorbance for many reflections can be written as

$$A = a \sum_{reflections} \left(\vec{E}(\vec{r}_i) \bullet \vec{\mu}(\vec{r}_i)\right)^2, \tag{2.8}$$

where $\vec{r}_i$ is the position of the i^{th} reflection. In the geometry defined by Fig. 2.4, the absorbance of *p*-polarized radiation, which has components both in-plane and perpendicular to the surface, can be written as

$$A_p = a \sum_{reflections} \left(E_x(\vec{r}_i)\mu_x(\vec{r}_i) + E_z(\vec{r}_i)\mu_z(\vec{r}_i)\right)^2. \tag{2.9}$$

The absorbance of *s*-polarized radiation, which is polarized entirely in -plane, is therefore

$$A_s = a \sum_{reflections} \left(E_y(\vec{r}_i)\mu_y(\vec{r}_i)\right)^2. \tag{2.10}$$

At each reflection, the in-plane and surface-normal components of the *p*-polarized radiation accumulate a few-degree phase shift, which leads to a gradual oscillation from linearly polarization to circular polarization with successive reflections. After summing over all reflections and accounting for field averaging,[9] the absorbance of *p*-polarized light becomes

$$A_p = cE_x^2\mu_x^2 + cE_z^2\mu_z^2, \tag{2.11}$$

and the absorbance of *s*-polarized light can be written as

$$A_s = c\left(E_y\mu_y\right)^2, \tag{2.12}$$

where the number of reflections is absorbed into the constant *c*.

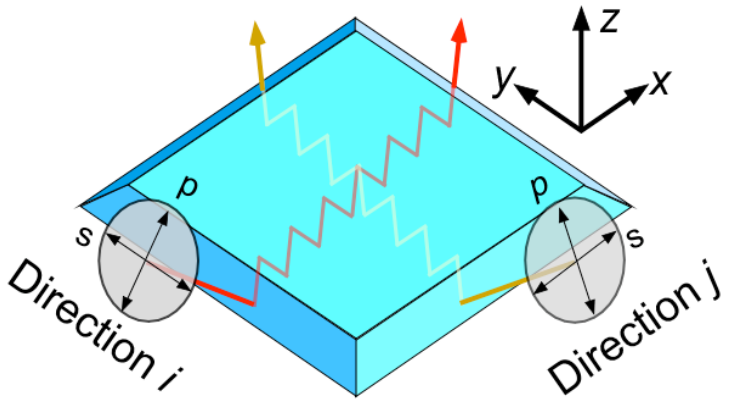

Figure 2.5. Schematic of MIR geometry used for analysis of low-symmetry silicon surfaces. A set of *p*- and *s*-polarized spectra were collected in two orthogonal directions. In practice, two separate samples were used.

To isolate the contributions from μ_x^2, μ_y^2, and μ_z^2, *p*- and *s*-polarized spectra must be collected in two orthogonal propagation directions, *i* and *j*, as shown in Fig. 2.5. When

the path lengths in each direction are equal, the absorbances in these four geometries are given by

$$\begin{pmatrix} A_{p,i} \\ A_{s,i} \\ A_{p,j} \\ A_{s,j} \end{pmatrix} = c \begin{pmatrix} E_{\parallel}^2 & 0 & E_{\perp}^2 \\ 0 & E_s^2 & 0 \\ 0 & E_{\parallel}^2 & E_{\perp}^2 \\ E_s^2 & 0 & 0 \end{pmatrix} \begin{pmatrix} \mu_x^2 \\ \mu_y^2 \\ \mu_z^2 \end{pmatrix}, \tag{2.13}$$

where $A_{p,i}$ represents the absorbance of *p*-polarized light propagating in the *i* direction, and the electric field components, $\boldsymbol{E}$, are defined in Eqns. 2.4-6. Equation 2.10 is overdetermined. The best-fit dipole $\boldsymbol{\mu^2}$ is obtained from the Moore-Penrose inverse of the electric field matrix, which yields

$$\begin{pmatrix} \mu_x^2 \\ \mu_y^2 \\ \mu_z^2/\varepsilon_z^2 \end{pmatrix} = \frac{1}{c} \begin{pmatrix} \dfrac{\left|E_{\parallel}^0\right|^2 \left(A_{p,i} - A_{p,j}\right)}{2\left(\left|E_{\parallel}^0\right|^4 + \left|E_s^0\right|^4\right)} + \dfrac{\left|E_{\parallel}^0\right|^4 \left(A_{s,i} + A_{s,j}\right) + 2\left|E_s^0\right|^4 A_{s,j}}{2\left|E_s^0\right|^2 \left(\left|E_{\parallel}^0\right|^4 + \left|E_s^0\right|^4\right)} \\ \dfrac{\left|E_{\parallel}^0\right|^2 \left(A_{p,i} - A_{p,j}\right)}{2\left(\left|E_{\parallel}^0\right|^4 + \left|E_s^0\right|^4\right)} + \dfrac{\left|E_{\parallel}^0\right|^4 \left(A_{s,i} + A_{s,j}\right) + 2\left|E_s^0\right|^4 A_{s,i}}{2\left|E_s^0\right|^2 \left(\left|E_{\parallel}^0\right|^4 + \left|E_s^0\right|^4\right)} \\ \dfrac{2\left|E_{\perp}^0\right|^2 \left|E_s^0\right|^2 \left(A_{p,i} + A_{p,j}\right) - \left(\left|E_{\parallel}^0\right|^2 / \left|E_s^0\right|^2\right)\left(A_{s,i} + A_{s,j}\right)}{2\left|E_{\perp}^0\right|^2} \end{pmatrix}. \tag{2.14}$$

Eqn. 2.14 expresses the Cartesian components of the transition dipole moment in terms of the measured absorbances, the calculated surface electric fields, and the z-component of the adsorbate dielectric constant, ε_z. If the intensities of the incident *p*- and *s*-polarized radiation are of equal magnitude, the right-hand side of Eq. 2.14 depends only on the dielectric constant of the medium, the angle of incidence of the infrared radiation, the measured absorbances, and a constant. The value of ε_z affects the scaling of the magnitude of the transition dipole's z component relative to the in-plane components.

Because the adsorbate dielectric tensor is difficult to measure, the orientation of transition dipole moment usually cannot be measured directly from the spectroscopic data.

A full derivation and validation of the deconvolution technique can be found in Ref. 9.

2.4.3 Absorbance on macroscopically symmetric surfaces

In certain cases, surface symmetry will cause the in-plane component of the transition dipole moment to be rotationally invariant. For example, a flat Si(100) terrace has twofold rotational symmetry, but the direction of the mirror plane rotates by 90º on successive terraces. Thus, a macroscopic Si(100) sample will have macroscopic fourfold rotational symmetry. As a result, $\mu_x^2 = \mu_y^2 \equiv \mu_\parallel^2$. A similar situation occurs on Si(111), which has threefold rotational symmetry. For surfaces with this type of rotational invariance, the acquisition of *p*- and *s*-polarized spectra in a single propagation direction are sufficient, and Eq. 2.13 is significantly simplified to yield

$$\begin{pmatrix} A_p \\ A_s \end{pmatrix} = c \begin{pmatrix} E_\parallel^2 & E_\perp^2 \\ E_s^2 & 0 \end{pmatrix} \begin{pmatrix} \mu_\parallel^2 \\ \mu_z^2 \end{pmatrix}. \tag{2.15}$$

Equation 2.15 can be inverted to yield

$$\begin{pmatrix} \mu_\parallel^2 \\ \mu_z^2 / \varepsilon_z^2 \end{pmatrix} = \frac{1}{c} \begin{pmatrix} \dfrac{1}{\left|E_s^0\right|^2} A_s \\ \dfrac{A_p}{\left|E_\perp^0\right|^2} - \dfrac{\left|E_\parallel^0\right|^2}{\left|E_\perp^0\right|^2 \left|E_s^0\right|^2} A_s \end{pmatrix}. \tag{2.16}$$

As for surfaces with no rotational symmetry, the uncertainty in ε_z only affects the relative magnitude of the *z*-component of the transition dipole.

2.5. Scanning tunneling microscopy

The morphology of etched silicon surfaces was studied with a custom, Besocke-type scanning tunneling miscroscope (STM) mounted in an ultra-high vacuum chamber equipped with a turbomolecular-pumped load lock.[10] The design and previous modifications to this instrument have been described elsewhere;[11,12] however, several significant modifications were made to the STM control electronics prior to this work.[13]

After etching, STM samples were placed on a clean, Teflon chuck, and an InGa eutectic was applied to the back edge of the sample to form an ohmic contact to the sample holder. The STM sample was then placed in the load-lock chamber of the STM, which was evacuated to ~10 mTorr with a liquid-nitrogen-cooled absorption pump and then evacuated to ~10^{-8} Torr with a turbomolecular pump. The sample was then transferred into the main chamber (10^{-10} Torr base pressure) for analysis.

Tungsten tips were prepared *ex situ* via electrochemical sharpening[12] and were annealed inside the STM chamber before use. Images were acquired in constant current mode at sample biases of -2.0 to -2.5 V and tunneling currents of 0.2-0.3 nA.

REFERENCES

[1] W. Kern, in *Handbook of Silicon Wafer Cleaning Technology*, 2nd ed., edited by K. A. Reinhardt and W. Kern (William Andrew Inc., 2008), p. 3-92.

[2] P. Jakob, P. Dumas, and Y. J. Chabal, Applied Physics Letters **59,** 2968-2970 (1991).

[3] A. Ogura, Journal of the Electrochemical Society **138,** 807-810 (1991).

[4] W. Kern and D. A. Puotinen, RCA Review **31,** 187-205 (1970).

[5] Y. J. Chabal, Surface Science Reports **8,** 211-357 (1988).

[6] L. J. Webb, S. Rivillon, D. J. Michalak, Y. J. Chabal, and N. S. Lewis, Journal of Physical Chemistry B **110,** 7349-7356 (2006).

[7] R. G. Greenler, Journal of Chemical Physics **44,** 310-315 (1966).

[8] P. J. Feibelman, Progress in Surface Science **12,** 287-407 (1982).

[9] I. T. Clark, B. S. Aldinger, A. Gupta, and M. A. Hines, Journal of Chemical Physics **128,** 144711-1 - 144711-9 (2008).

[10] K. Besocke, Surface Science **181,** 145-153 (1987).

[11] T. A. Newton, Ph.D. Dissertation, Cornell University, 2000.

[12] S. P. Garcia, Ph.D. Dissertation, Cornell University, 2004.

[13] I. T. Clark, Ph.D. Dissertation, Cornell University, 2008.

Chapter 3

Ammonium fluoride etching of Si(100)

The production of flat Si(100) surfaces has been a long-standing challenge to the microelectronics industry. In the initial stages of microelectronic device fabrication, silicon wafers are subjected to caustic, highly aggressive solutions that effectively remove many types of contamination but roughen the wafer surface in the process.[1] The harsh cleaning process increases the initial wafer root-mean-square (RMS) roughness from 0.2 to 1.2 nm, which has been shown to decrease the channel mobility by a factor of four for transistors subsequently fabricated on the wafer.[2] Consequently, a long search has been made for etchants that remove atomic-scale roughness while producing atomically clean Si(100) surfaces. From a mechanistic perspective, an ideal etchant would remove defect sites much more quickly than terrace sites and leave behind a smooth, passivated surface. Several etchants (*e. g.,* NH_4F) have been found that create atomically flat Si(111) surfaces by step-flow etching,[3-5] but similar success on the industrially-relevant Si(100) surface has been elusive.

The widely accepted conclusion is that the well-studied NH_4F etchant progressively roughens Si(100) surfaces by forming {111} and {110} microfacets.[6] Infrared absorbance spectra collected after 3 min of etching Si(100) in $NH_4F(aq)$ show overlapping broad transitions in the Si-H stretching region, which have been assigned to a mixture of monohydride, dihydride, and trihydride species—a heterogeneous mixture indicative of significant roughness.[7] Several techniques, including reflection high-energy electron diffraction (RHEED), temperature programmed desorption (TPD), and infrared absorbance spectroscopy, show evidence for the growth of {111} facets on Si(100) surfaces with increasing $NH_4F(aq)$ etch times over the range of 1-14 minutes.[8,9] Using

infrared absorption spectroscopy, Nakamura *et al.* observed that very long $NH_4F(aq)$ etch times (up to 2 hrs) produced Si(100) surfaces that were almost entirely {111}- and {110}-terminated.[10] Lastly, STM images of $NH_4F(aq)$-etched Si(100) surfaces showed roughness that was attributed to {111}-microfaceted hillocks.[11] These studies led many researchers to conclude that the Si(100) surface is atomically rough at all stages of $NH_4F(aq)$ etching,[7,12,13] with extended etching producing {111} and {110} microfacets.[8-10]

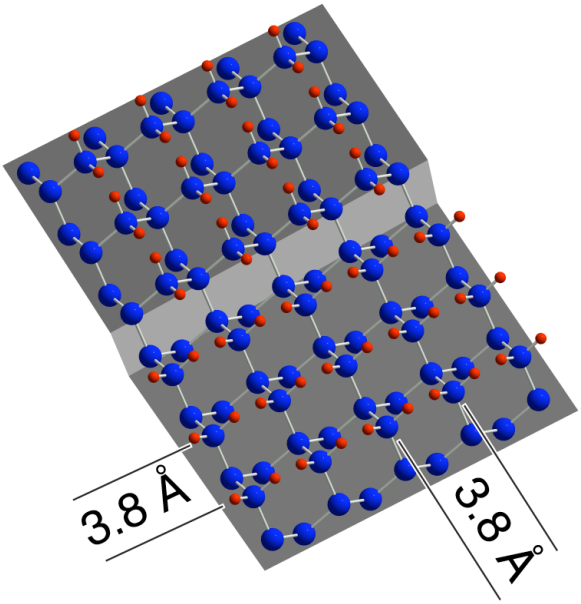

Figure 3.1. An ideal H-terminated Si(100) surface. Silicon atoms are shown in blue, and hydrogen atoms are in red. Individual terraces have C_2 symmetry, but the macroscopic Si(100) surface has C_4 symmetry.

The tendency for Si(100) to microfacet during etching has been explained in terms of strain minimization. Many aqueous etchants produce hydrogen-terminated surfaces.[14] An ideal, bulk-terminated H/Si(100) surface would be entirely dihydride-terminated as shown in Fig. 3.1. In this configuration, H atoms on adjacent dihydrides would be separated by only 1.5 Å—far less than the 2.4 Å van der Waals diameter of H—

as shown in Fig. 3.2. *Ab initio* calculations predict that strained dihydrides spontaneously cant to reduce interadsorbate repulsion.[15-17] As shown in Fig. 3.2, canting increases the

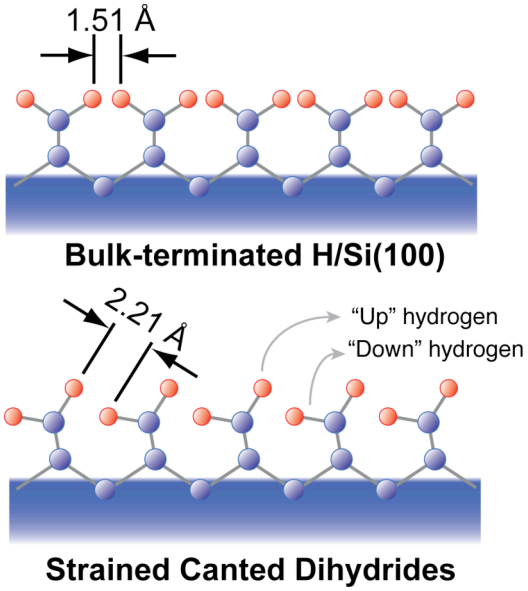

Figure 3.2. Schematic of symmetric and canted strained dihydrides. Canting increases the interadsorbate distance between neighboring hydrogen atoms. The labeled atomic spacing for the canted structure was calculated by Northrup.[16]

inter-hydrogen distance between neighboring dihydrides. Bulk-terminated Si(100) has never been experimentally observed over large areas. Etching with $NH_4F(aq)$ *does* produce ideal, bulk-terminated H/Si(111) and H/Si(110) surfaces terminated entirely by unstrained monohydride species.[3,18] Because the adsorbates on an ideal Si(100) surface are sterically strained, hillock formation during etching would reduce interadsorbate repulsion through the creation of {111} and {110} microfacets. For example, Fig. 3.3 depicts the atomic structure of a pyramidal hillock on a Si(100) surface. The {110} and {111} facets are terminated by unstrained monohydrides, and the apex of the pyramid consists of a single unstrained dihydride. Consequently, the H/Si(100) surface with minimal interadsorbate strain would be covered by faceted hillocks.

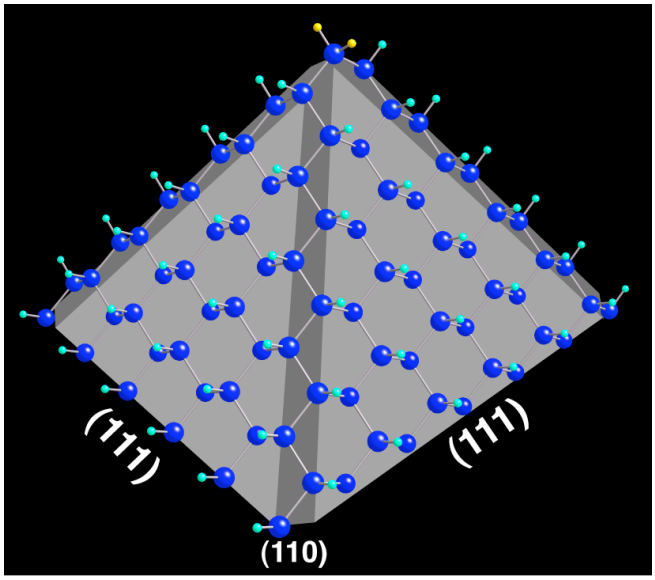

Figure 3.3. Schematic of a pyramidal hillock on Si(100), with {111} facets shown in light grey and {110} facets in dark grey. Unstrained dihydrides are depicted in yellow, and unstrained monohydrides are in aqua.

Contrary to the accepted conclusion, this chapter shows that $NH_4F(aq)$ etching of Si(100) can produce hydrogen-terminated surfaces of near-atomic flatness. The chemical structure of the etched surface was elucidated with scanning tunneling microscopy (STM) and infrared absorption spectroscopy. Although very similar infrared absorbance spectra were published nearly twenty years ago, new spectral assignments are proposed based on insights made possible by a recently-developed deconvolution technique that separates the transitions into their Cartesian components, greatly reducing spectral complexity.

The $NH_4F(aq)$-etched Si(100) surface structure was not the minimally strained morphology (*i.e.* a completely faceted surface), and previously postulated features, such as hillocks and trihydrides, were not observed. The discrepancy between these results and conventional wisdom are discussed.

3.1. Experimental

Both flat and miscut Si(100) surfaces were required for structural studies. STM samples were cut from single-side-polished, 0.5-10 Ω cm, nominally-flat Si(100) wafers

[within 0.9º of the (100) plane] or from wafers miscut by 3.5º ± 0.1º towards the [011] direction. Samples for infrared absorption experiments were prepared from high resistivity (>1000 Ω cm) silicon wafers oriented within 0.9º of the (100) plane or miscut by 5º or 9º towards the [011] direction (Virginia Semiconductor). Sample preparation and cleaning are described in Chapter 2.

After sample cleaning, the thermal oxide was removed by a 90 s immersion in buffered oxide etch [5:1 by weight of 40% NH_4F(*aq*):HF(*aq*), Mallinckrodt Baker, CMOS-grade], which produced a clean, H-terminated surface. The sample was then rinsed for ~10 s in ultrapure water (Millipore, Milli-Q). Samples for STM analysis were cleaned with an additional acidic peroxide clean (1:1:5 ratio by volume of 13 M HCl(*aq*) (J.T. Baker, ACS grade), 30% H_2O_2, and ultrapure water) for 10 min at 80ºC, followed by copious rinsing in ultrapure water. The chemical oxide produced by cleaning was removed by a ~15 s immersion in buffered oxide etch.

The cleaned sample was then etched in room-temperature, 40% NH_4F (*aq,* Mallinckrodt Baker, CMOS grade) in a pre-cleaned Teflon boat. Gas bubbles, produced by the etching reaction, became visible after 10 s of etching. To prevent bubble-induced roughening, the sample was drawn through the air/etchant interface every 15 s using Teflon forceps. (Bubble-induced roughening is discussed in Chapter 4.) Samples were etched for 2 min, unless otherwise noted. After etching, the sample was dipped in ultrapure water to remove residual etchant. STM samples were loaded into the UHV-STM following the procedure in Section 2.4.

After cleaning, multiple-internal-reflection (MIR) samples were placed in a Teflon holder, whereas transmission samples were secured with small magnets to a steel holder. The samples were loaded into a Nicolet 670 FTIR spectrometer and purged for approximately 5 min with dry air. Spectra were taken with both *p*- and *s*-polarized radiation. For miscut surfaces, two sets of *p*- and *s*-polarized spectra were collected in

orthogonal sample orientations. Background spectra were collected after *in situ* surface oxidation by 15 min exposure to the ozone produced by a mercury pen lamp (Pen-Ray Mercury Lamp, UVP Inc.). Spectral deconvolution of both nominally flat Si(100) and miscut Si(100) surface spectra was performed as described in Chapter 2.

The macroscopic etch rate of $NH_4F(aq)$ towards Si(100) was determined by gravimetric analysis. A 100-mm-diameter, double-side polished, undoped, nominally flat Si(100) wafer was placed in a 125-mm-diameter Pyrex crystallization dish containing etchant. The dish was suspended in an ultrasonic agitator, which dislodged bubbles from the wafer surface during etching, as described in greater detail in Section 4.2.6. The wafer was removed from the etchant every 10 min, dipped in ultrapure water to remove residual ethant, and weighed. The temperature of the water bath was kept constant with periodic additions of ice.

To investigate the temperature dependence of the vibrational modes, low-temperature infrared spectra were collected in a custom UHV chamber in the Chabal lab at the University of Texas at Dallas. Low-resistivity (20 Ω cm) silicon samples were used to facilitate resistive heating. The etched sample was secured at both ends by copper clamps in thermal contact with a liquid nitrogen reservoir. The temperature was measured by chromel-alumel thermocouples spot-welded to tantalum clips placed at the top and bottom of the sample. Control spectra were collected at 40ºC instead of ambient, because the room was not temperature-controlled. Low temperature spectra were collected at -110ºC, the practical lower limit of the apparatus. The sample was then oxidized *in situ* by heating it to 700ºC for 45 s in a 10^{-4} Torr O_2 atmosphere, and background spectra were collected at -110ºC and 40ºC. Spectra were taken in the transmission geometry at the Brewster angle for silicon, 74º, without a polarizer.

3.2. Results

3.2.1. STM

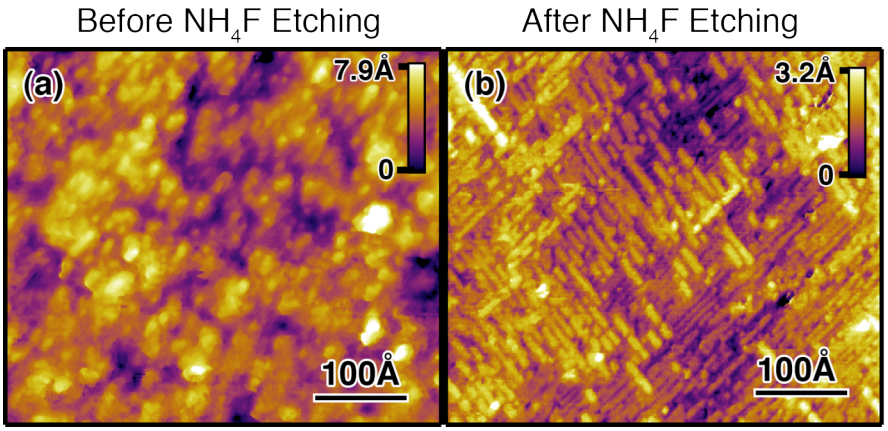

Figure 3.4. STM images of H-terminated Si(100) surfaces before and after etching in 40% $NH_4F(aq)$. (a) Surface morphology after thermal oxide removal. (b) Surface after 2 min etching in 40% $NH_4F(aq)$. The sample was drawn through the interface every 15 s during etching to remove H_2 bubbles.

Contrary to previous findings, $NH_4F(aq)$ etching of Si(100) produced surfaces of near-atomic flatness. Figure 3.4(a) shows an STM image of a cleaned sample immediately prior to etching. The morphology was characterized by irregularly shaped hillocks, with a RMS roughness of 1.5 Å as measured over a 450 Å × 500 Å image. A dramatic transformation was produced by etching in 40% $NH_4F(aq)$ for 2 min as shown in Fig. 3.4(b). During the 2 min of etching, approximately 180 monolayers were removed, as estimated from the gravimetrically-determined etch rate of 1.5 ML/s (~12.5 nm/min). The morphology of the etched surface was much smoother than that of the unetched surface, with a RMS roughness of only 0.7 Å. Instead of hillocks, the etched surface displayed terraces of long, parallel, row-like features. This smooth morphology persisted over larger length scales as well, as seen in Fig. 3.5(a). Figure 3.5(b) shows a histogram of the height distribution of the image in (a) that was fit to four Gaussians of equal width.

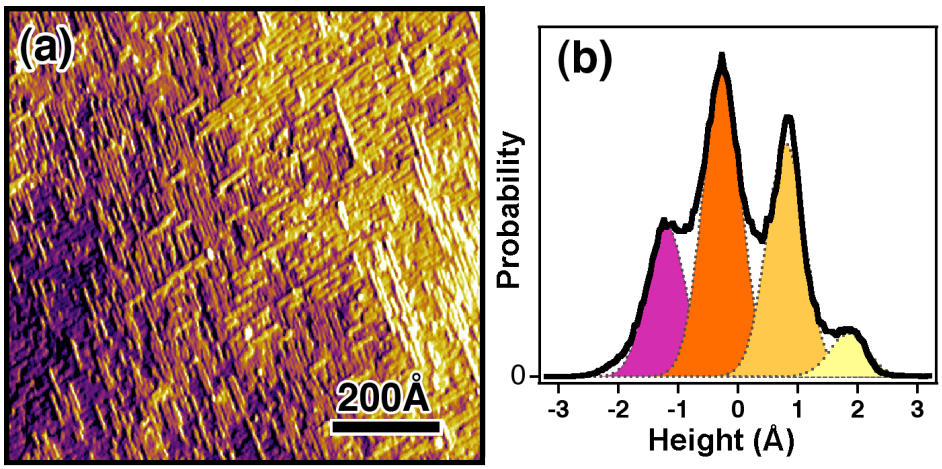

Figure 3.5. (a) STM image of a Si(100) surface etched for 30 s in NH_4F. The histogram in (b) shows the height distribution for the image, measuring the relative population of each layer.

The fit in Fig. 3.5(b) shows that 74% of the atoms in the 950 Å × 1000 Å image were located within two atomic planes. Although the NH_4F-etched Si(100) surface was very flat, the morphology did not display the atomically-smooth terraces expected of a bulk-terminated surface. Instead, a "missing-row" structure was observed. On the NH_4F-etched surface, the row alignment alternated between the $[01\bar{1}]$ and $[011]$ directions in successive layers, as shown in Fig. 3.6.

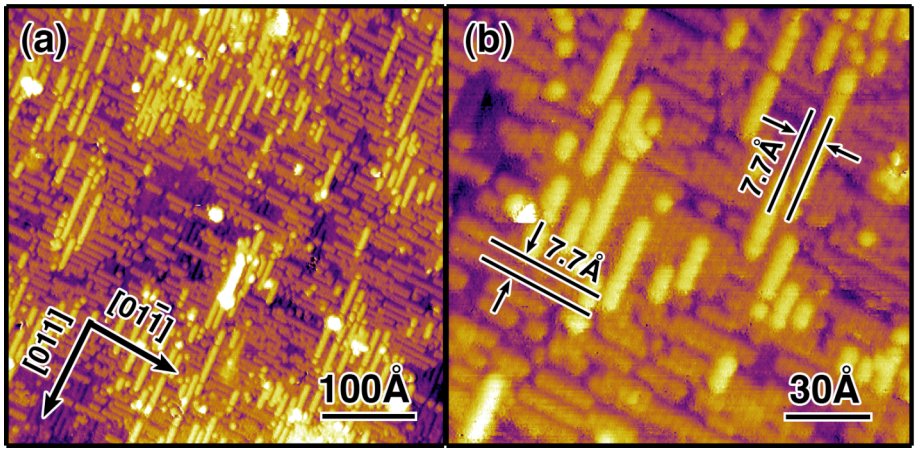

Figure 3.6. STM images of a nominally flat Si(100) sample etched in $NH_4F(aq)$, showing a (a) wide field view and (b) a higher magnification view of the same sample. The rows run along <011> directions with a typical inter-row spacing of 7.7Å.

As illustrated by Fig. 3.6(b), adjacent parallel rows within a terrace were generally spaced at least 7.7 Å from one another, approximately twice the surface lattice spacing of 3.8 Å. A periodic corrugation with a 3.8 Å spacing was sometimes observed along the long axis of the rows. This corrugation has been highlighted for clarity in Fig. 3.7. The surface morphology showed no change over etching times of 30 s to 45 min (see Chapter 4 for further discussion).

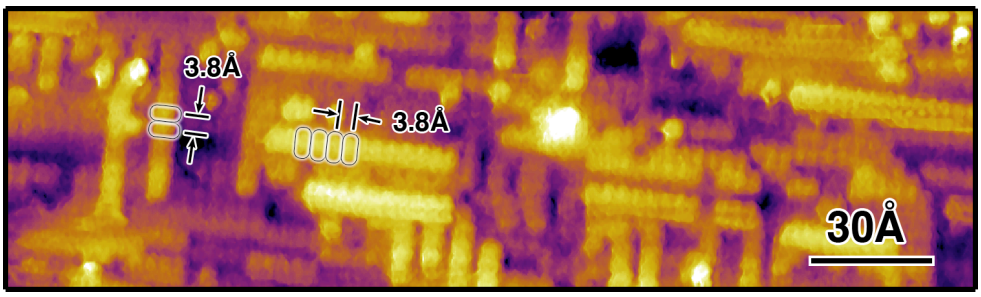

Figure 3.7. STM image of an NH_4F-etched Si(100) surface. The corrugation has been highlighted with thin outlines.

The observed row spacing and corrugation are consistent with a number of structures, including the four shown in Fig. 3.8. For example, (at least) three structures can be generated by removing every other row of Si atoms from a bulk-terminated Si(100) surface, seen in Fig. 3.8(a-c). If alternating rows of dihydrides are removed from the bulk-terminated surface in the direction perpendicular to the plane of the SiH_2 bonds, the resulting surface will have rows of unstrained dihydrides separated by rows of strained dihydrides, as sketched in Fig. 3.8(a). On the other hand, if *two* layers of dihydrides are removed from the bulk-terminated surface, the valleys between rows of unstrained dihydrides would be terminated with highly strained monohydrides, as in Fig. 3.8(c). Removal of alternating rows of dihydrides from the bulk-terminated surface in the

orthogonal direction (*i.e.* parallel to the plane of the SiH_2 bonds) would produce a structure with rows of strained dihydrides separated by single-height valleys of strained monohydrides, as shown in Fig. 3.8(b).

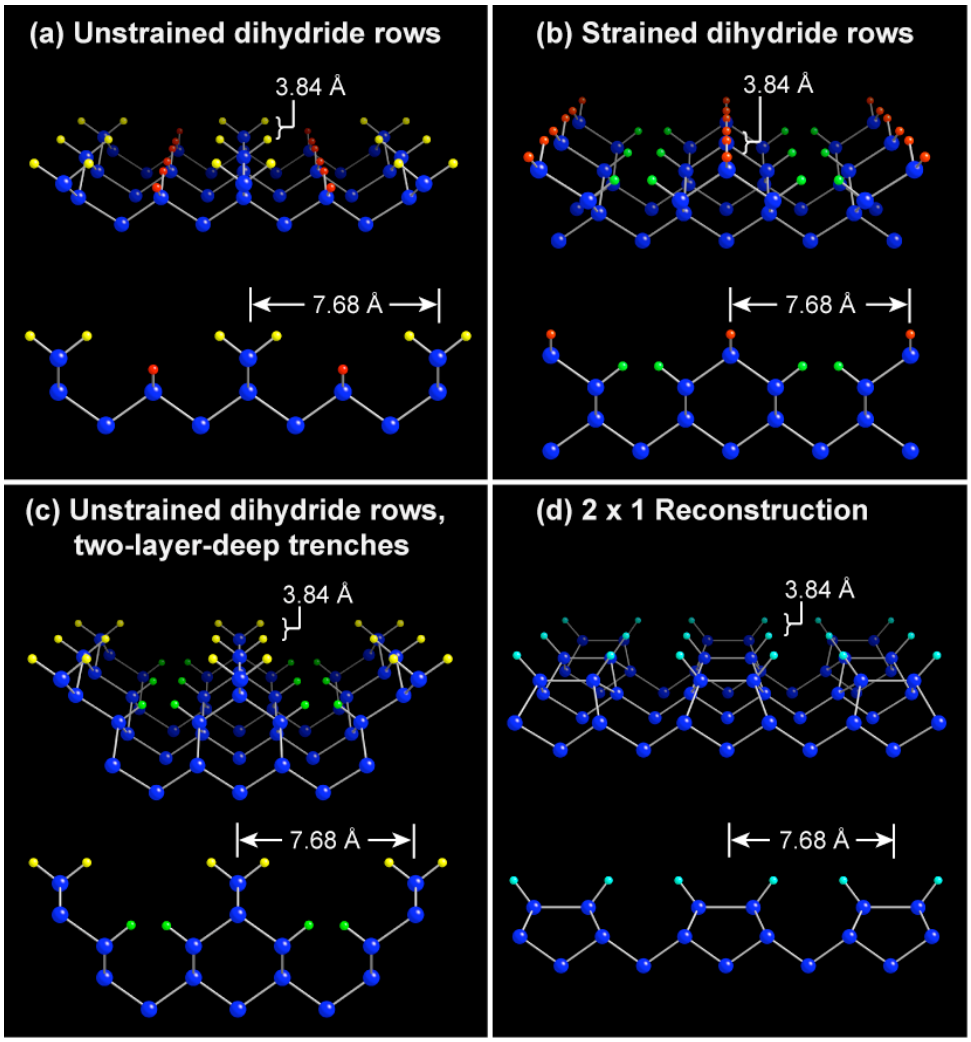

Figure 3.8. Four surface structures consistent with the periodicity and row orientations observed in STM images of NH_4F(*aq*)-etched Si(100). (a) Unstrained dihydrides with the SiH_2 units perpendicular to the row direction. (b) Strained dihydrides with the SiH_2 units parallel to the row direction. The two structures (a) and (b) are formed by removing single-height rows from an ideal H/Si(100) surface rotated by 90º with respect to one another. (c) Same as (a), except with a two-layer-deep inter-row valley. (d) 2 × 1 reconstructed H/Si(100) surface. Hydrogens of unstrained dihydrides are shown in yellow, strained dihydrides in red, unstrained monohydrides in aqua, and strained monohydrides in green.

The 2×1 H/Si(100) surface reconstruction, shown in Fig. 3.8(d), also has the same row-spacing and corrugation. This structure is formed by dimerizing adjacent silicon atoms and capping the remaining dangling bonds with hydrogen. This reconstruction can be prepared *in vacuo* by treating clean Si(100) surfaces with atomic hydrogen and has been studied extensively by infrared spectroscopy[19] and STM.[20]

Although the interatomic spacings of all four structures in Fig. 3.8 were consistent with the STM images, the orientation of the elliptical protrusions was suggestive. Simulated STM images computed with density functional theory (DFT) suggest that Si(100) dihydride units will appear as ellipses elongated in the plane of the dihydride bonds.[21] The orientation of the corrugation highlighted in Fig. 3.7 would be consistent with the structures in Fig. 3.8(a), (c), and (d).

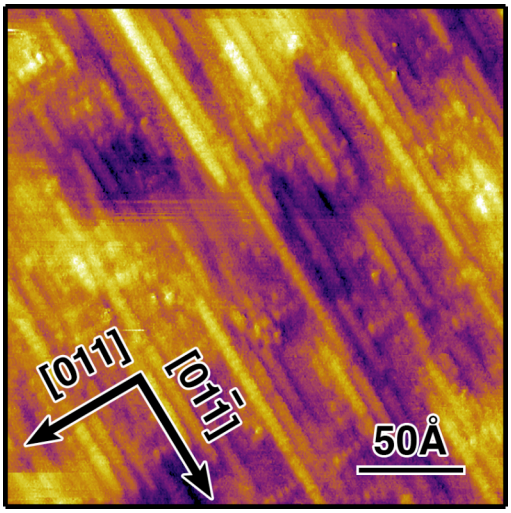

Figure 3.9. STM image of a NH_4F-etched Si(100) sample miscut by 3.5° toward the [011] direction. The rows are preferentially oriented with their long axes perpendicular to the miscut.

Spontaneous symmetry breaking of the missing-row structure was observed when miscut samples were etched. Figure 3.9 shows an STM image of a Si(100) surface miscut by 3.5° towards the [011] direction after etching for 2 min in 40% $NH_4F(aq)$. The long

row features were preferentially aligned perpendicular to the miscut direction (*i.e.* parallel to the step direction).

3.2.2. Infrared spectroscopy

The chemical composition and structure of the $NH_4F(aq)$-etched Si(100) surface were determined using infrared absorption spectroscopy. No absorption was observed in the C-H, O-H, or Si-O stretching regions, indicating that the surface was free of hydrocarbon contamination and oxidation. The *p*- and *s*-polarized spectra of the Si–H stretching region, shown in Fig. 3.10(a), were similar in shape to one another, both having broad, overlapping absorbance bands. The infrared spectrum of NH_4F-etched Si(100) was invariant over etching times of 30 s to 45 min.[Ch. 4] Both the *p*- and *s*-polarized spectra were nearly identical to those previously reported by Dumas *et al.*[7]

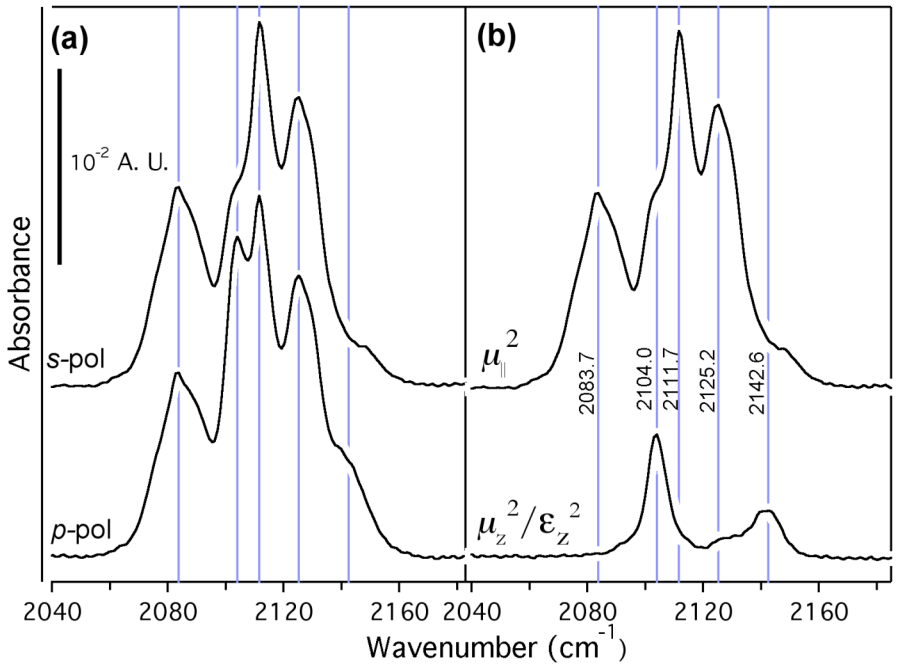

Figure 3.10. Infrared absorption spectra of the Si-H stretching region of a Si(100) sample etched for 2 min in 40% $NH_4F(aq)$ taken in the MIR geometry. In (a), the *p*- and *s*-polarized spectra are shown, whereas (b) displays the Cartesian components of the squared transition dipole moment obtained by spectral deconvolution. The positions of five well-defined spectral features are marked with blue lines.

Using the deconvolution technique summarized in Chapter 2, the squared transition dipole moments from the *p*- and *s*-polarized spectra were transformed into their Cartesian components—μ_x^2, μ_y^2, and μ_z^2—as shown in Fig. 3.10(b). As discussed in Section 2.4.3, the two in-plane components, μ_x^2 and μ_y^2, are equivalent by symmetry on Si(100) and are referred to as $\mu_{||}{}^2$. The perpendicular component, μ_z^2, is screened by the z-component of the adsorbate dielectric tensor, ε_z. (Because ε_z is usually unknown, the absolute orientation of the dipoles cannot be determined.) The deconvolution procedure separated the absorbances into five well-defined bands: three were primarily polarized in the plane of the surface (at 2083.7 cm^{-1}, 2111.7 cm^{-1}, and 2125.2 cm^{-1}), and two polarized primarily along the surface normal (at 2104.0 cm^{-1} and 2142.6 cm^{-1}).

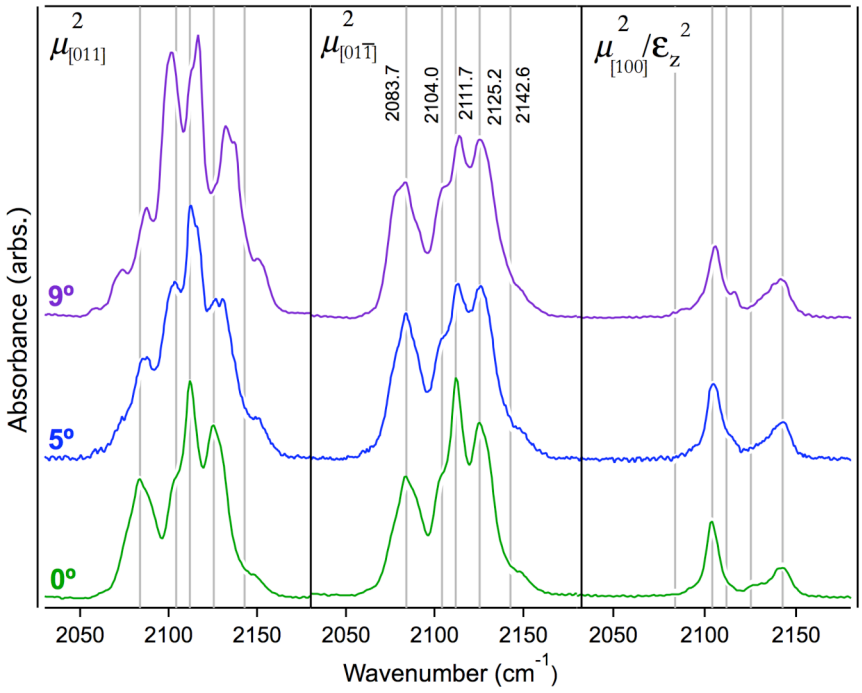

Figure 3.11. Comparison of the Cartesian components of the squared transition dipole moment obtained from infrared absorption spectra of $NH_4F(aq)$-etched silicon samples with 5° and 9° miscut towards the [011] direction and a nominally flat sample (0°) for reference. The Cartesian coordinates are defined by the surface normal and the two directions in Fig. 3.9. For the nominally flat (0° miscut) surface, the two in-plane spectra are identical by symmetry. Grey lines denote the same energies as in Figure 3.10.

Additional spectral simplification was obtained by using Si(100) samples miscut toward the [011] direction. Figure 3.11 shows the Cartesian components of the squared transition dipole moment for vicinal Si(100) surfaces miscut by 5° and 9° towards the [011] direction. The three components of the transition dipoles were $\mu^2_{[011]}$, perpendicular to the preferential row direction, $\mu^2_{[01\bar{1}]}$, parallel to the row direction, and $\mu^2_{[100]}/\varepsilon^2_z$, along the surface normal. The spectrum of a nominally flat NH_4F(*aq*)-etched Si(100) surface is shown for comparison. The broad mode at 2083.7 cm^{-1} was polarized primarily along the $[01\bar{1}]$ direction (parallel to the rows), whereas the mode at 2111.7 cm^{-1} was polarized primarily in the $[011]$ direction (perpendicular to the rows). The other in-plane transition at 2125.2 cm^{-1} was present in both polarizations.

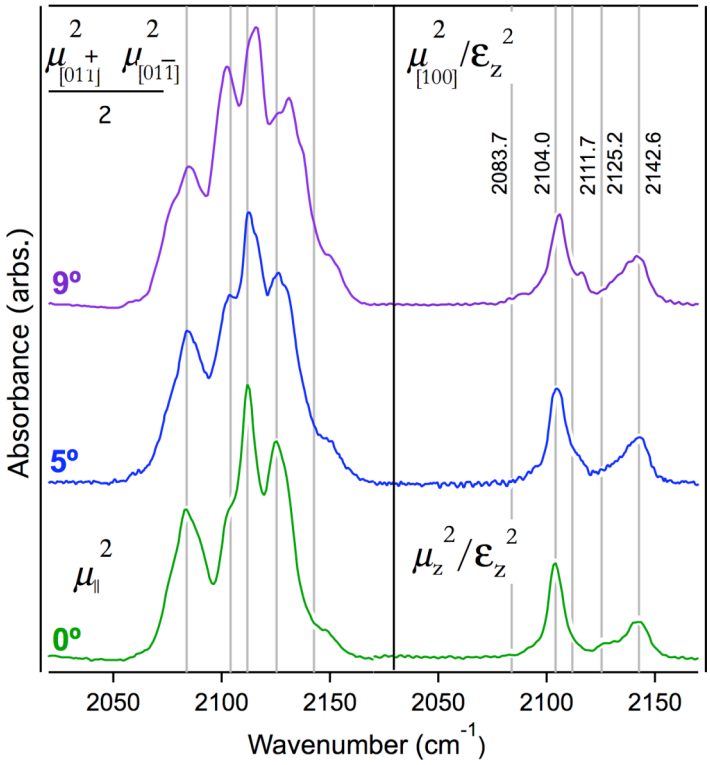

Figure 3.12. Comparison of the Cartesian components of the squared transition dipole moment obtained from infrared absorption spectra of NH_4F(*aq*)-etched silicon samples with 5° and 9° miscut towards the [011] and a nominally flat sample (0°). The in-plane components of each vicinal surface were averaged for comparison with the in-plane component of the nominally-flat surface.

The 9º and, to a lesser extent, 5º miscut surface spectra showed additional weak modes at 2116.5 cm^{-1} and 2132.0 cm^{-1} which may be due to step modes. In the absence of step modes, the relation $2\mu_{\|}^2 \approx \mu_{[011]}^2 + \mu_{[01\bar{1}]}^2$ should hold, where $\mu_{\|}^2$ is the in-plane component of the nominally-flat etched surface spectrum. Figure 3.12 compares these quantities. The averaged in-plane component of the 5º miscut surface had approximately the same shape as the in-plane component of the nominally-flat surface, suggesting that step modes have a minimal contribution. In contrast, there are significant differences for the 9º miscut surface, particularly in the mode at 2104.0 cm^{-1}. Furthermore, the modes at 2111.7 cm^{-1} and 2125.2 cm^{-1} for the 9º miscut surface had high-energy shoulders that were not present for the flat surface.

The low frequency region of *p*- and *s*-polarized transmission spectra of flat and vicinal surfaces are shown in Fig. 3.13. Two broad, overlapping, perpendicular polarized modes were observed at 906 cm^{-1} and 918 cm^{-1} for all sample miscuts. A strong mode was seen at 658 cm^{-1} in both the *p*- and *s*-polarized spectra. This mode gained intensity in the $[01\bar{1}]$ direction (*i.e.* parallel to the step edges) with increasing miscut angle.

A low-temperature infrared spectrum of NH_4F(*aq*)-etched Si(100) is shown in Fig. 3.14. The bands in the Si-H stretch region did not become narrower at low-temperature, although a uniform 3 cm^{-1} blueshift of the stretching modes was observed after lowering the temperature from 40ºC to -110ºC. This blueshift is comparable to the temperature-dependent shift observed for the terrace stretching vibration on H/Si(111). In the case of H/Si(111), the blueshift is attributed to the weak coupling of the Si-H stretch mode with a surface phonon.[22]

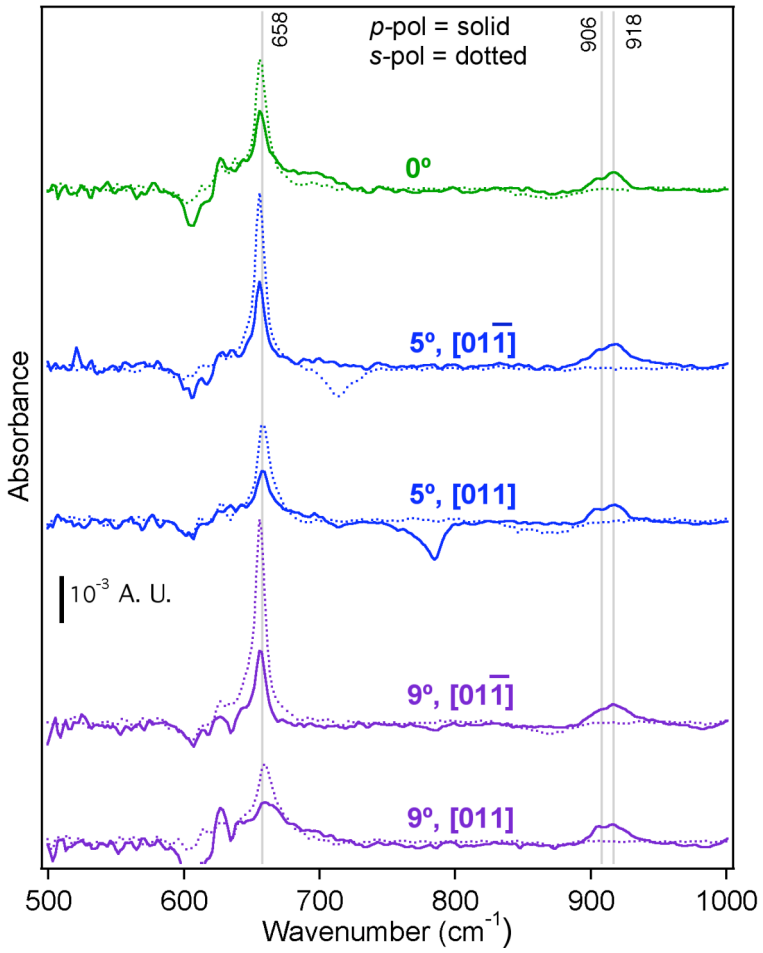

Figure 3.13. Infrared *p*- and *s*-polarized absorbance spectra taken in the transmission geometry for flat and vicinal Si(100) surfaces etched in 40% $NH_4F(aq)$ for 2 min. For the 5° and 9° miscut surfaces, spectra were collected with the *s*-component of the electric field aligned in the $[011]$ and $[01\bar{1}]$ surface lattice directions.

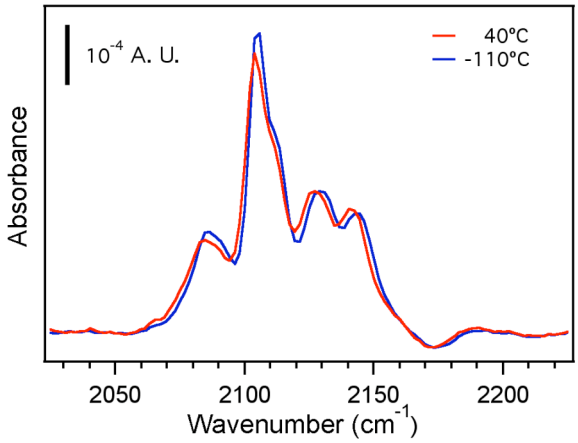

Figure 3.14. Transmission spectra taken at a 74° angle of incidence (no polarizer) of the Si-H stretch region of a NH_4F-etched Si(100) surface. Spectra were taken at 40°C (red) and -110°C (blue). A ~3 cm^{-1} blueshift was observed for the low temperature spectrum.

3.3. Discussion

3.3.1. Surface structure and the assignment of infrared absorbance bands

STM images of NH_4F(*aq*)-etched Si(100) have been interpreted by Neuwald *et al.*[11] as evidence for the formation of a 2×1 reconstructed H-terminated surface. This interpretation was inconsistent with the infrared spectra of NH_4F(*aq*)-etched Si(100). Figure 3.15 compares the infrared spectrum of a H-terminated 2×1 reconstructed Si(100) surface[19] to the spectrum of NH_4F(*aq*)-etched Si(100). The 2×1 H/Si(100) surface spectrum has only two major absorbance modes in the range of 2060 cm^{-1} to 2100 cm^{-1}, whereas NH_4F(*aq*)-etched Si(100) has five well-defined modes and significant absorbance above 2100 cm^{-1}. Based on the complete dissimilarity between the spectra, the 2×1 H/Si(100) structure in Fig. 3.8(d) was eliminated as a possibility for the surface morphology of NH_4F(*aq*)-etched Si(100).

Dumas *et al.*[7] first noted the difficulty of assigning the vibrational modes of the NH_4F(*aq*)-etched Si(100) surface due to the broad, overlapping bands and the similarity between the *p*- and *s*-polarized spectra. Based on cluster calculations, they assigned the

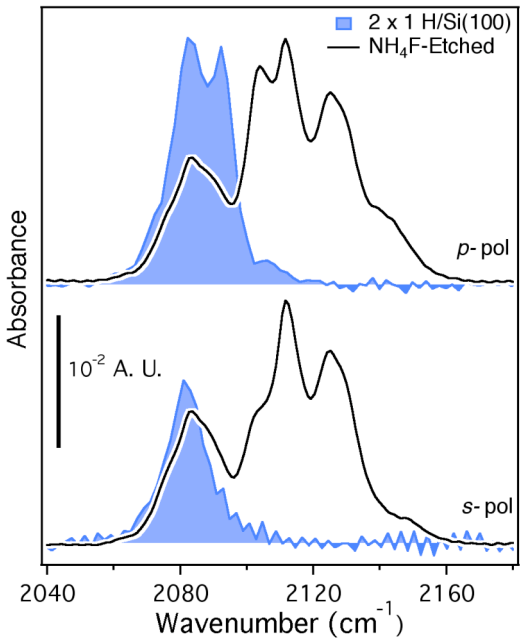

Figure 3.15. The *p*- and *s*-polarized spectra of 2 × 1 H/Si(100) (fill) compared to NH_4F(*aq*)-etched Si(100) (trace) are very dissimilar. The 2 × 1 H/Si(100) spectra are from Niwano *et al.*[9]

spectral features into regions of surface monohydrides (2070 cm^{-1}- 2090 cm^{-1}), dihydrides (2104-2112 cm^{-1}), and trihydrides (2125-2140 cm^{-1}).[23] Because of similarities to the Si-H stretching frequency on H/Si(111), the band at 2084 cm^{-1} was assigned to monohydrides on Si{111} microfacets. On Si(100), all Si-H bonds are 55° from the surface normal, which implies that monohydride stretching transitions will have significant perpendicular character. This has been confirmed experimentally for {111} microfacets on H/Si(100).[24] In contradiction to this expectation, Fig. 3.10(b) shows the 2083.7 cm^{-1} band to be in-plane polarized. Dumas *et al.* had also assigned the modes at 2125.7 cm^{-1} and 2142.3 cm^{-1} to symmetric and antisymmetric vibrations of trihydrides; however, the STM images above do not show tall protrusions consistent with surface trihydrides. In light of these contradictions, a new assignment of the NH_4F(*aq*)-etched Si(100) vibrational modes is proposed, as summarized in Table 3.1.

Table 3.1. Energies and mode assignments of infrared transitions observed for the $NH_4F(aq)$-etched Si(100) surface.

Species	Mode	Polarization	Energy (cm^{-1})
Strained Dihydride	"Up"	Perpendicular	2142.6
Strained Monohydride	-	Mostly in-plane	2125.2
Unstrained Dihydride	Antisymmetric stretch	In-plane	2111.7
Unstrained Dihydride	Symmetric stretch	Perpendicular	2104.0
Strained Dihydride	"Down"	In-plane	2083.7
Unstrained Dihydride	Scissor	Perpendicular	918
Strained Dihydride	Scissor	Mostly perp.	906
Strained Dihydride	Wag	In-plane	659.6
Unstrained Dihydride	Wag	In-plane	655.7

The modes at 2104.0 cm^{-1} and 2111.7 cm^{-1} were assigned to the symmetric and antisymmetric stretching vibrations, respectively, of unstrained dihydrides, in agreement with Dumas *et al.*[7] The observed splitting of 7.7 cm^{-1} between the symmetric and antisymmetric modes is in good agreement with the 9-11 cm^{-1} predicted by simulations.[Ch.6, 25,26] This assignment is confirmed by the polarization dependence of these modes in Fig. 3.11. For the miscut surfaces, the absorbance of the antisymmetric vibration at 2111.7 cm^{-1} was more intense in the $[011]$ direction (perpendicular to the rows) than in the $[01\bar{1}]$ direction (parallel to the rows). This observation would be expected for surface structures in which the long rows consisted of unstrained dihydrides. Only the structures illustrated by Fig. 3.8(a) and (c) have unstrained dihydrides, thus arguing against the structure in Fig. 3.8(b). Because the symmetric stretching mode of unstrained dihydrides at 2104.0 cm^{-1} is perpendicularly polarized and not affected by the dihydride row alignment, no dependence on miscut angle was observed for the intensity of this transition.

The broad transitions at 2083.7 cm^{-1} and 2142.6 cm^{-1} were assigned to the stretching vibrations of the "down" and "up" hydrogens of strained canted dihydrides, respectively, as defined in Fig. 3.2. For the 5º and 9º miscut surface spectra in Fig. 3.11,

the 2083.7 cm^{-1} mode was primarily polarized in the $[01\bar{1}]$ direction (parallel to the preferential row direction observed in miscut surfaces). This polarization of the "down" stretching mode, in conjunction with the STM images and mode assignments discussed above, was consistent with a structure having rows of canted dihydrides aligned with rows of unstrained dihydrides, as illustrated in Fig. 3.8(a). The "up" stretching mode at 2142.6 cm^{-1} was almost entirely perpendicularly polarized, which would be consistent with the geometry depicted in Fig. 3.2.

The structure and vibrational spectrum of canted dihydrides have been calculated in several theoretical studies in the context of bulk-terminated H/Si(100).[15-17,27] Because of the non-symmetric dihydride geometry, the predicted stretching modes are relatively uncoupled, consisting of isolated stretches of the "up" hydrogen and the "down" hydrogen. Although there is no consensus among the published vibrational frequency predictions, the observed ~59 cm^{-1} splitting between the stretching modes is comparable to the ≥100 cm^{-1} predicted by Freking *et al.,*[17] and is in excellent agreement with 63 cm^{-1} splitting predicted by recent DFT calculations described in Chapter 5.

A pair of highly strained monohydrides, as depicted in Fig. 3.7(c), would be expected to have two coupled stretching modes, with one polarized perpendicular to the preferential row direction. This is inconsistent with the polarizations of the transitions at 2083.7 cm^{-1} and 2142.6 cm^{-1}. Additionally, DFT calculations predict that the energies of these vibrations would be in the range 2170-2185 cm^{-1}. (See Chapter 5)

The mode at 2125.2 cm^{-1} (with mostly in-plane character) was tentatively assigned to the stretching vibrations of isolated strained monohydrides. Although the ideal missing-row structure in Fig. 3.8(a) is completely dihydride-terminated, etched surfaces have a variety of imperfections as seen in Fig. 3.6(b). The steps and defects depicted in Fig. 3.15 include strained monohydrides (green spheres) at the ends of unstrained dihydride rows on terrace edges. A monohydride stretch at 2125.2 cm^{-1} is unprecedented

(the H/Si(111) vibration for unstrained monohydrides occurs at 2083.7 cm^{-1}), although Jakob and Chabal have shown that strained monohydrides on miscut Si(111) surfaces are blueshifted by ~20 cm^{-1} relative to the terrace monohydride.[28]

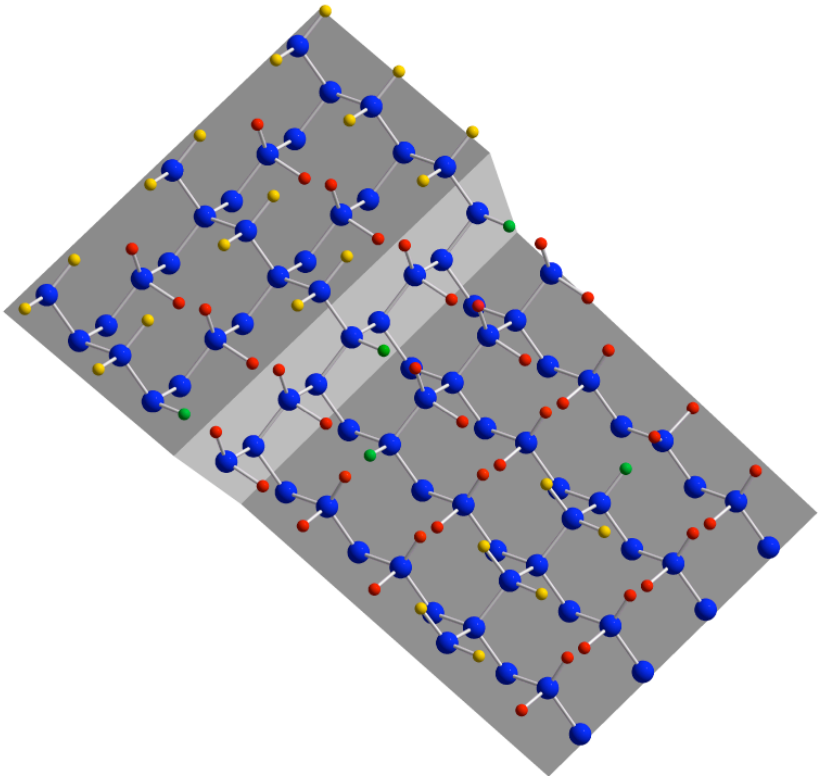

Figure 3.16. Illustration of an imperfect NH_4F-etched Si(100) surface. Unstrained dihydride hydrogen atoms are shown in yellow, strained dihydride hydrogen atoms in red, and strained monohydrides in green.

The broad modes at 908 cm^{-1} and 918 cm^{-1} were assigned to scissor vibrations of strained and unstrained dihydrides, respectively. On Si(100), the scissor mode of a symmetric dihydride would be entirely perpendicularly polarized, whereas the corresponding mode of a canted dihydride would have an in-plane component. In Fig. 3.13, the intensity of the mode at 918 cm^{-1} did not vary with azimuthal orientation. This invariance indicated that the 918 cm^{-1} mode was completely perpendicularly

polarized and was therefore assigned to symmetric (unstrained) dihydrides. In contrast, the intensity of the 908 cm^{-1} mode in Fig. 3.11 had a small azimuthal dependence, as expected for canted (strained) dihydrides. Studies of miscut Si(111) surfaces have assigned a similar mode at 913 cm^{-1} to the scissor vibration of strained step dihydrides.[29,30]

The strong transition at 658 cm^{-1} was similar in energy to the 656 cm^{-1} mode previously assigned to the step dihydride wagging mode on miscut Si(111);[29,30] however, the shape and energy of this mode varied with azimuthal orientation, suggesting the presence of two overlapping modes. When the incident radiation was parallel to the row direction (*i.e.* $[01\bar{1}]$ polarization), the transition was centered at 655.7 cm^{-1}. In contrast, when the light was polarized in the perpendicular direction (*i.e.* $[011]$ polarization), the mode was centered at 659.6 cm^{-1}. On Si(100), dihydride wagging modes for both symmetric (*i.e.* unstrained) and canted (*i.e.* strained) dihydrides should be primarily in-plane polarized. Therefore, the 655.7 cm^{-1} and 659.6 cm^{-1} modes were assigned to the wagging vibrations of unstrained and strained dihydrides, respectively. For the nominally flat surface spectra in Fig. 3.13, these two modes were not resolved and appeared as a single broad absorbance at 658 cm^{-1}.

3.3.2. Strain minimization and the mechanism of NH_4F Si(100) etching

The morphology of NH_4F-etched Si(100), with rows of unstrained dihydrides separated by canted dihydrides, does not represent the minimally-strained structure. The idealized missing-row structure in Fig. 3.8(a) still has half the interadsorbate strain of a bulk-terminated Si(100) surface, because half of the rows consist of strained, canted dihydrides. If the etching mechanism were governed solely by strain minimization, roughened Si(100) morphologies dominated by hillocks would be produced. For example, Fig. 3.3 shows that {111} and {110} facets of hillocks on Si(100) consist of unstrained monohydrides; however, no evidence of hillocks were observed.

The structure of NH_4F-etched Si(100) provides insight into the etching mechanism. The observation of long rows indicates that row-end sites are more reactive than terrace sites. In the case of the missing-row structure, the row-end site is a strained monohydride attached to a dihydride, as illustrated in Fig. 3.16. This site has the same geometry as the fastest etching site on H/Si(111) surfaces (*i.e.* the kink site), although the amount of interadsorbate strain is different for the Si(100) surface.[31] Kinetic Monte Carlo (KMC) simulations of Si(100) suggest that a row-end site must etch at least 100 times faster than atoms within the row to produce a missing-row morphology.[32] In addition, the existence of rows of strained, canted dihydrides in the valleys suggests that these sites are relatively unreactive; otherwise, double atomic-layer-deep valleys of opposing monohydrides would be expected to form, as illustrated in Fig. 3.8(c). Although strain can weaken bonds and increase reactivity, the prevalence of strained dihydrides suggests that etching may be governed more by steric hindrance rather than energetic considerations. Finally, the alternating row structure seems to indicate that strain has long-range effects on chemical reactivity. The exact requirements for the production of a surface like NH_4F-etched Si(100) are still under investigation with KMC simulations. Preliminary results show that a model must incorporate both the elevated reactivity of row-end sites and differing amounts of interadsorbate strain in order to reproduce the experimental morphology.[32]

3.3.3. Factors complicating the analysis of NH_4F-etched Si(100)

The etching of Si(100) by NH_4F has been studied for two decades, so why has it taken until 2010 to report the production of near-atomically flat Si(100) surfaces with this etchant?[33] In earlier studies, the production of near-perfect, atomically-flat H/Si(111) by $NH_4F(aq)$ etching was inferred from the presence of a single, intense Si-H stretching mode—not by direct imaging.[3] The linewidth for the H/Si(111) terrace mode is 0.9 cm^{-1} at room temperature, decreasing to 0.1 cm^{-1} at 130 K, which is by far the narrowest

linewidth observed to date for any adsorbate vibration.[22] The extremely narrow linewidth implies low heterogeneous broadening and thus a very flat surface with few defects. Accordingly, researchers expected that atomically flat (or nearly flat) H/Si(100) should have similarly narrow bands. As shown by Fig. 3.10, this is not the case. The stretching region of NH_4F-etched Si(100) extends from 2070 cm^{-1} to 2150 cm^{-1}, and the narrowest mode has a width of at least 10 cm^{-1}. In retrospect, this reasoning is overly simplistic, particularly for systems with severe interadsorbate strain. For example, a defect (*i.e.* missing atom) in a row of canted dihydrides would presumably allow partial relaxation of the dihydrides into the space formerly occupied by the defect, thus causing local shifts in structure and vibrational frequency. If the wide absorbance bands in NH_4F-etched Si(100) were due instead to homogeneous broadening or variations in interadsorbate coupling, the bands would potentially become narrower at low-temperatures; however, this was not observed in the low temperature infrared spectra illustrated in Fig. 3.14. This result supports the hypothesis that the wide absorbance bands in $NH_4F(aq)$-etched Si(100) are caused by heterogeneous broadening due to strain relaxation, which would not be temperature dependent.

Experimental complications may also have delayed the discovery of flat wet-chemically etched Si(100). Silicon etching reactions are very sensitive to minute amounts of contamination, which can sometimes lead directly to roughness (*e. g.,* nucleation of etch pits, oxidation).[34] Contaminants may also be deposited on the etched surface as it is drawn through the air/water interface or during loading the sample into the STM. A contaminated surface will appear rough in most scanned probed microscopies. These factors may have contributed to the conclusion of previous researchers that NH_4F-etched Si(100) surfaces were rough.

Finally, hydrogen gas is a byproduct of the NH_4F/Si(100) etching reaction. When not removed during etching, bubbles can lead to roughening of the etched surface and

formation of {111}-microfaceted etch pits. This mechanism may explain some of the rough morphologies reported by others and is discussed extensively in the next chapter.

3.4. Conclusions

The structure of Si(100) surfaces etched in 40% $NH_4F(aq)$ was investigated using STM and infrared absorption spectroscopy. The etched surface structure did not have the minimally strained morphology (*i.e.* faceted hillocks). Instead, $NH_4F(aq)$-etched Si(100) was composed primarily of rows of unstrained dihydrides separated by rows of strained, canted dihydrides. No evidence for hillock formation or microfaceting was observed. Previous spectral assignments that classified the vibrational spectra into three regions of monohydride, dihydride, and trihydride stretching modes were shown to be incorrect. Cartesian component analysis of the vibrational spectra of miscut surfaces was used to assign the five main vibrational modes, two each from canted and unstrained dihydrides and one from strained monohydrides. Although the etched surface is of near-atomic flatness, significant heterogeneous broadening was observed in the infrared spectrum. The broadness was attributed to defects in the "missing-row" structure that caused local variations in interadsorbate strain.

REFERENCES

[1] W. Kern, in *Handbook of Silicon Wafer Cleaning Technology*, 2nd ed., edited by K. A. Reinhardt and W. Kern (William Andrew Inc., 2008), p. 3-92.

[2] T. Ohmi, K. Kotani, A. Teramoto, and M. Miyashita, IEEE Electron Device Letters **12,** 652-654 (1991).

[3] G. S. Higashi, Y. J. Chabal, G. W. Trucks, and K. Raghavachari, Applied Physics Letters **56,** 656-658 (1990).

[4] P. Allongue, Physical Review Letters **77,** 1986-1989 (1996).

[5] S. P. Garcia, H. Bao, and M. A. Hines, Physical Review Letters **93,** 166102-1 - 166102-4 (2004).

[6] Y. J. Chabal, G. S. Higashi, and R. J. Small, in *Handbook of Silicon Wafer Cleaning Technology, 2nd Edition*, 2 ed., edited by K. A. Reinhardt and W. Kern (William Andrew Inc., 2008), p. 515-606.

[7] P. Dumas, Y. J. Chabal, and P. Jakob, Surface Science **269/270,** 867-878 (1992).

[8] V. L. Thanh, D. Bouchier, and G. Hincelin, Journal of Applied Physics **87,** 3700-3706 (2000).

[9] M. Niwano, Y. Takeda, Y. Ishibashi, K. Kurita, and N. Miyamoto, Journal of Applied Physics **71,** 5646-5649 (1992).

[10] M. Nakamura, M.-B. Song, and M. Ito, Electrochimica Acta **41,** 681-686 (1996).

[11] U. Neuwald, H. E. Hessel, A. Feltz, U. Memmert, and R. J. Behm, Surface Science **296,** L8-L14 (1993).

[12] D. Gräf, S. Bauer-Mayer, and A. Schnegg, Journal of Vacuum Science & Technology A: Vacuum, Surfaces, and Films **11,** 940-944 (1993).

[13] C. H. Bjorkman, M. Fukuda, T. Yamazaki, S. Miyazaki, and M. Hirose, Japanese Journal of Applied Physics **34,** 722-726 (1995).

[14] G. W. Trucks, K. Raghavachari, G. S. Higashi, and Y. J. Chabal, Physical Review Letters **65,** 504-507 (1990).

[15] S. Ciraci and I. P. Batra, Surface Science **178,** 80-89 (1986).

[16] J. E. Northrup, Physical Review B **44,** 1419-1422 (1991).

[17] U. Freking, P. Krüger, A. Mazur, and J. Pollmann, Physical Review B **69,** 035315-1 - 035315-11 (2004).

[18] K. Arima, J. Katoh, S. Horie, K. Endo, T. Ono, S. Sugawa, H. Akahori, A. Teramoto, and T. Ohmi, Journal of Applied Physics **98,** 103525-1 - 103525-8 (2005).

[19] Y. J. Chabal and K. Raghavachari, Physical Review Letters **53,** 282-285 (1984).

[20] J. J. Boland, Physical Review Letters **67,** 1539-1542 (1991).

[21] K. Endo, K. Arima, K. Hirose, T. Kataoka, and Y. Mori, Journal of Applied Physics **91,** 4065-4072 (2002).

[22] P. Dumas, Y. J. Chabal, and G. S. Higashi, Physical Review Letters **65,** 1124-1127 (1990).

[23] Y. J. Chabal, G. S. Higashi, K. Raghavachari, and V. A. Burrows, Journal of Vacuum Science & Technology A: Vacuum, Surfaces, and Films **7,** 2104-2109 (1989).

[24] M. F. Faggin and M. A. Hines, Review of Scientific Instruments **75,** 4547-4553 (2004).

[25] Y. J. Chabal and K. Raghavachari, Physical Review Letters **54,** 1055-1058 (1985).

[26] M. K. Weldon, K. T. Queeney, A. B. Gurevich, B. B. Stefanov, Y. J. Chabal, and K. Raghavachari, Journal of Chemical Physics **113,** 2104-2109 (2000).

[27] K. Tagami, E. Tsuchida, and M. Tsukada, Surface Science **446,** L108-L112 (2000).

[28] P. Jakob and Y. J. Chabal, Journal of Chemical Physics **95,** 2897-2909 (1991).

[29] S. Watanabe, Journal of Chemical Physics **108,** 5965-5974 (1998).

[30] Y. Caudano, P. A. Thiry, and Y. J. Chabal, Surface Science **502,** 91-95 (2002).

[31] M. A. Hines, Annual Review of Physical Chemistry **54,** 29-56 (2003).

[32] A. Gupta, B. S. Aldinger, M. F. Faggin, and M. A. Hines, Journal of Chemical Physics **(in press)** (2010).

[33] I. T. Clark, B. S. Aldinger, A. Gupta, and M. A. Hines, Journal of Physical Chemistry C **114,** 423-428 (2010).

[34] T. Bearda, P. W. Mertens, and S. P. Beaudoin, in *Handbook of Silicon Wafer Cleaning Technology*, edited by K. A. Reinhardt and W. Kern (William Andrew Publishing, 2008), p. 93-164.

Chapter 4

Roughening of Silicon Surfaces Due to Gas Evolution During Etching

In the early steps of microelectronics device manufacture, silicon wafers undergo harsh chemical cleaning processes that effectively remove contamination but that also roughen the wafer surface.[1] A smooth silicon substrate, however, is essential for optimal device performance, as even a 1 nm increase in root-mean-square roughness of the starting wafer has been shown to decrease the channel mobility of the final transistor by a factor of 4.[2] For this reason, an anisotropic etchant capable of removing wafer roughness has been long sought. From this perspective, an ideal etchant would rapidly remove defect sites (*i.e.* roughness) much faster than terrace sites, leaving behind an atomically flat silicon surface. In the case of the (111) silicon crystal face, several etchants have been shown to produce atomically flat Si(111) surfaces via step-flow etching.[3-5] Similar success on the Si(100) surface, the basis of nearly all microelectronic devices, has been a long-standing challenge.

Anisotropic etchants are also used to intentionally *roughen* silicon surfaces. For instance, the reflectivity of monocrystalline solar cells can be decreased by roughening the wafer, thereby increasing the amount of energy generated per cell.[6] For this application, etchants are sought that produce {111}-faceted pyramids on the Si(100) substrate either directly[7,8] or in conjunction with patterning.[9]

The rational development of new anisotropic etchants that produce surfaces with tailored morphologies—either rough or smooth—will require a full understanding of the chemical reactivity of the surface. In general, anisotropic silicon etchants can be divided into two groups—strong aqueous bases, such as KOH or tetramethylammonium hydroxide, and fluoride-containing etchants, such as HF or NH_4F. Both classes of

etchants typically produce hydrophobic silicon surfaces that are primarily or entirely H-terminated, and in general, these etchants attack Si(111) surfaces more slowly than other faces of silicon. Silicon etching is a multistep process in which the first step is a slow oxidation reaction followed by fast removal of the oxidized silicon atom from the surface.[10] For many commonly used silicon etchants, especially alkaline solutions, H_2 gas evolution accompanies oxidation. In the case of $NH_4F(aq)$ etching of silicon, the net reactions are often written as

$$\equiv Si{-}H + OH^-(aq) + H_2O(l) \rightarrow \equiv Si{-}OH + H_2(g) + OH^-(aq), \text{ and} \qquad \text{(oxidation)}$$

$$(\equiv Si)_3Si{-}OH + 3\ HF(aq) + H_2O(l) \rightarrow 3(\equiv Si{-}H) + SiF_3OH(aq). \qquad \text{(etching)}$$

Because of the technological importance of Si(100), elucidating the etching mechanisms responsible for roughening this surface is critical. As discussed in the previous chapter, $NH_4F(aq)$ etching of Si(100) selectively removes every other row of silicon dihydrides to produce a near-atomically flat morphology of alternating, single-atom-height rows.[11] This observation stands in stark contrast to previous investigations that observed evidence for surface roughening[12] and the formation of Si{111} microfacets.[13,14] This chapter resolves this apparent discrepancy and shows that the same etchant can produce near-atomically flat or highly microfaceted Si(100) surfaces. Although the extreme anisotropy of NH_4F is a *prerequisite* for the production of very flat surfaces, this anisotropy does not guarantee smoothness.

Hydrogen bubbles evolved during etching were observed to produce several types of roughened Si(100) morphologies. Two mechanisms of bubble-induced roughening are proposed. In the first, bubbles locally mask the etching surface, producing circular etch pillars. Under some conditions, temporary pinning of the bubble on a surface defect or contaminant induces oscillatory bubble growth, which leads to the production of nested

circular etch pillars. The second mechanism is more subtle. When two bubbles coalesce, the surface underneath the new, larger bubble is often covered by a fine spray of etchant that produces circular micropits. After the masking bubble dislodges or migrates across the surface, these etch pits are re-exposed to the bulk etchant. Larger pits retain their circular morphology while smaller pits are quickly widened by the anisotropic etchant to expose the slow-etching facets.

Because bubble-induced roughening can ruin the desired flatness of an etching surface, several techniques were also explored for mitigating bubble formation and coalescence, including withdrawal of the sample through the air/etchant interface, ultrasonic agitation, and the addition of an electrolyte. Long-duration etching experiments in which bubbles were assiduously removed showed that the atomic-scale etching mechanism did not inherently lead to microfaceting. Instead, bubble-induced roughening is proposed as an explanation for prior observations that ammonium fluoride roughens Si(100) by creating {111} facets.

4.1. Experimental

Nominally undoped, high-resistivity (> 1000 Ω cm), float-zone silicon wafers and moderately doped (1-20 Ω cm) Czochralski wafers were used for these experiments. No morphological dependence on doping was observed. The samples were thermally oxidized, diced, and cleaned as described in Chapter 2. The second cleaning step, an SC2 clean, was sometimes omitted for roughening experiments analyzed with techniques (*e. g.,* optical microscopy, AFM) that were insensitive to trace amounts of contamination.

After cleaning, the samples were placed in a pre-cleaned Teflon dish containing buffered oxide etch [5:1 by weight of 40% $NH_4F(aq)$:50% $HF(aq)$, Mallinckrodt Baker, CMOS grade] for 75 s to remove the thermal oxide. The samples were then dipped in ultrapure water to remove residual etchant and etched in room temperature 40% $NH_4F(aq)$ in a Teflon dish for variable times.

Ultrasonic agitation was sometimes used to hasten the detachment of bubbles from the etching surface. In these experiments, the sample was propped on edge in a narrow (30 ml) Kimax beaker of etchant that was suspended in the water bath of an ultrasonic agitator. This orientation promoted the removal of bubbles from the faces of the etching surface.

In some experiments, the sample was etched in a ~1.5 M NH_4OOCCH_3 40% $NH_4F(aq)$ solution, which was made by adding ammonium acetate (Mallinckrodt Chemicals) to 40% $NH_4F(aq)$. The etch rate of Si(100) surfaces in this solution was determined by gravimetric analysis as described in Section 3.2.

Several techniques were used to characterize the morphology and composition of the etched surface. The etched samples were imaged with a Leica DM/LP optical microscope operating in dark-field mode. This mode enhanced the contrast of rough areas. Topographical images were obtained with an ADE Phase-Shift MicroXAM optical interferometric profilometer. Atomic force microscopy (AFM) images were acquired in non-contact tapping mode on a Digital Instruments Multimode AFM. Scanning tunneling microscopy (STM) and infrared absorption spectroscopy were performed as described in Chapter 2.

The growth of H_2 bubbles on the etching surface was quantified with data obtained from videomicroscopy. A very small silicon sample was placed inside a glass cuvette with flat windows and a Hirox-Digital KH-7700 bright field microscope was used to obtain side profile videos and images. In these experiments, the camera was first focused on the sample and then the $NH_4F(aq)$ was introduced into the cuvette with a pipette. The resulting video of bubble formation was analyzed with IGOR Pro (Wavemetrics).

4.2. Results

Silicon samples etched in quiescent $NH_4F(aq)$ accumulated bubbles visible to the naked eye after 15 s of etching. The polished surface of samples etched for longer than 5 min developed haziness that became more pronounced with increasing etch times—a sign of significant roughening.

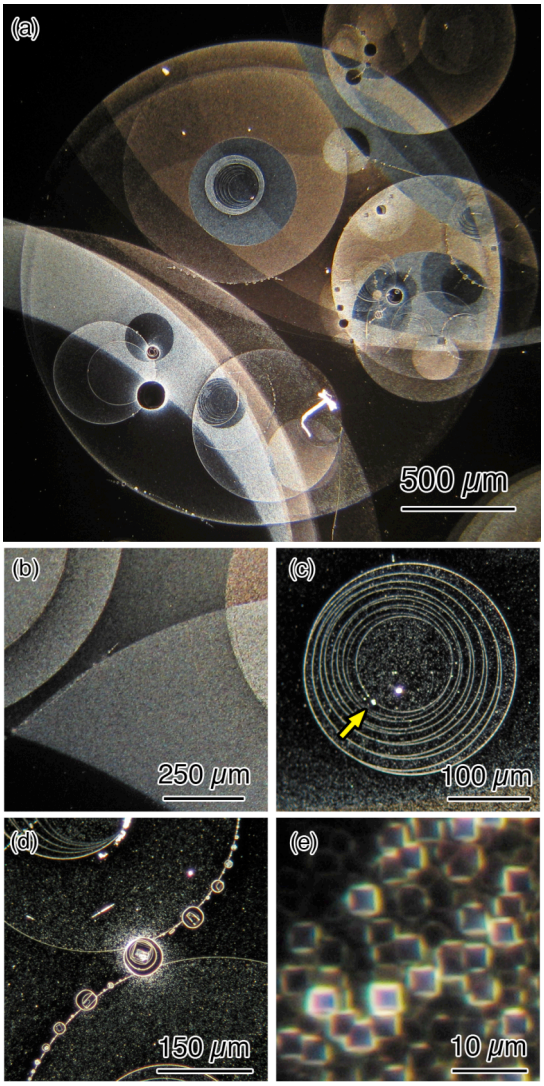

Figure 4.1. Dark-field optical micrographs of a Si(100) surface etched for 1 hr in quiescent, room-temperature $NH_4F(aq)$ showing a variety of circular and faceted features. The yellow arrow in (c) points to a particle that may have served as a pinning site.

Figure 4.1 shows typical dark-field micrographs of a Si(100) sample etched for 1 hr in quiescent $NH_4F(aq)$. In dark-field microscopy, surface roughness scatters light into the collection lens and appears bright, whereas smooth areas appear black. In Fig. 4.1(a), a major fraction of the surface appears bright, indicating that the surface was extensively roughened. In general, large features ($\geq$ 50 μm) were circularly symmetric, whereas smaller features tended to have four-fold symmetry. Figure 4.1(b) shows overlapping circles on the 250 μm to 1 mm scale of varying contrast and color, indicating regions with differing amounts of roughness. Smaller circular features (50 μm – 250 μm) were occasionally arranged in concentric patterns or curvilinear arrays as shown in Figs. 4.1(c) and (d), respectively. The high-contrast, colored circular areas in dark-field micrographs such as Fig. 4.1(a) were composed of micrometer-scale, square-like features with four-fold symmetry, as illustrated in Fig. 4.1(e). The following sections examine each type of feature in order of decreasing size.

4.2.1. Circular Etch Pillars

Large circular features (> 200 μm) often appeared in overlapping groups [*e. g.*, Fig. 4.1(b)] or as part of a roughly concentric pattern [*e. g.* Fig. 4.1(c)]. These structures were typically raised from the surface. For example, Fig. 4.2(a) shows a portion of a

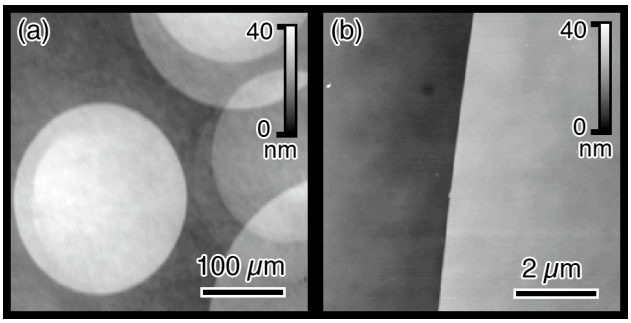

Figure 4.2. Si(100) surface etched for 3 min in quiescent, room-temperature $NH_4F(aq)$. (a) Optical profilometry shows raised, overlapping pillars and (b) AFM image shows a sharp pillar boundary.

surface after 3 min of etching that contains five overlapping circular features, each higher than the surrounding area. These circular structures had sharply defined boundaries and relatively flat tops, as shown in Fig. 4.2(b). In the case of concentric circular features, such as those in Fig. 4.1(c), the morphology resembled a stacked "wedding-cake" structure similar to those reported by Palermo *et al.*[15]

In-situ dark-field optical microscopy was used to observe bubble growth, which revealed a discontinuous growth of the bubble diameters. Extracted frames from a videomicrograph of a typical bubble during etching are shown in Fig. 4.3, where adjacent frames are separated in time by 1 second. Two rapid expansions occurred during the 12 s spanned by the frames, with the bubble diameter remaining nearly constant between discontinuous growth events. The actual expansion occurred faster than the capture rate of the video camera (≈ 0.1 s). In general, discontinuous growth was observed during the initial stages of bubble growth, typically within several minutes of nucleation.

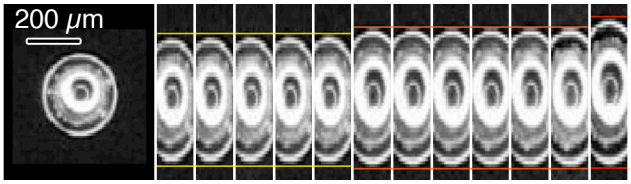

Figure 4.3. Sequential frames from a 12 s dark-field videomicrograph of a bubble growing on a Si(100) surface during $NH_4F(aq)$ etching. Each frame is separated by 1 s from the previous frame. Except for the first image, the vertical dimension has been stretched by a factor of 2 to exaggerate diameter changes. The bubble underwent two discontinuous growth events, each occurring in less than 0.1 s, the time resolution of the camera.

Side-profile bright-field videomicrographs of bubbles, as illustrated in the inset of Fig. 4.4, were used for quantitative analysis. A bubble that did not undergo any coalescence events was selected, and the bubble profile was fitted to a truncated ellipse. The height and contact width were measured as a function of time, and geometry was used to calculate the volume of the bubble, assuming cylindrical symmetry with respect to

the surface normal. Figure 4.4 shows the growth trajectory of a typical bubble over a period of 160 s. Two distinct modes of bubble growth were observed. Early in etching ($t \leq 77$ s), the contact width grew continuously, indicating a lack of growth pinning. Three times during the course of this experiment, the contact width remained almost constant during short periods, apparently becoming pinned until a rapid expansion occurred, as marked by the dashed lines in Fig. 4.4. The contact width and height traces showed characteristic discontinuities at the apparent depinning events, which corresponded to the rapid bubble expansion observed visually. In contrast to the contact width and height, the bubble volume increased smoothly through the rapid expansion events, as shown in Fig. 4.4(c), indicating that the reaction kinetics governing gas absorption were unaffected by the discontinuous growth events.

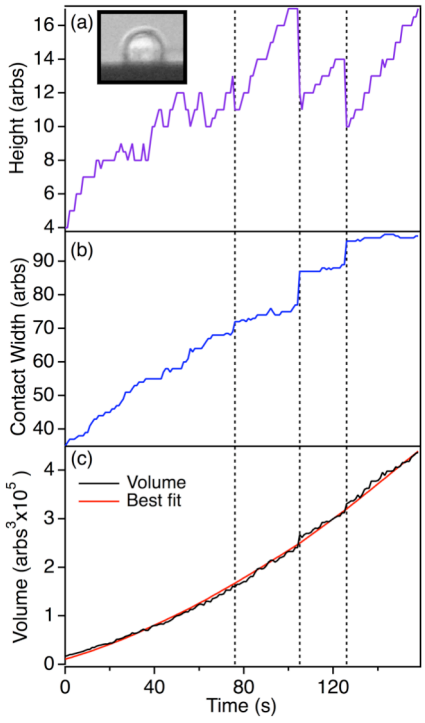

Figure 4.4. Evolution of the (a) height, (b) contact width, and (c) volume of a single H_2 bubble (inset) on a Si(100) surface during $NH_4F(aq)$ etching. The dotted lines indicate discontinuous growth events. The red line is the best fit to the model (see text).

Because the bubble volume in Fig. 4.4(c) grew continuously despite pinning events, bubble growth could be mathematically described by a simple model. If a bubble grows primarily via H_2 absorbed through the gas/liquid interface near the etching surface, and the local supersaturation of dissolved hydrogen is constant, then volume growth should be proportional to the circumference of the contact region, yielding

$$\frac{\partial V}{\partial t} = a\pi D, \tag{4.1}$$

where V and D are the volume and contact diameter of the bubble, and a is a constant. To test this mechanism, the volume growth data in Fig. 4.4(c) were fit to

$$V(t) = a\pi \int_0^t D(t_0)\, dt_0 + V(0), \tag{4.2}$$

where $V(0)$ and a were adjustable parameters. Bubble growth by H_2 absorption through the near-surface gas/etchant interface was supported by the good fit obtained in Fig. 4.4(c), which yielded 2.448 ± 0.095 arbs$^3 \times 10^5$ for $V(0)$ and 210.3 ± 0.9 arbs^3 for a. Models that assumed gas diffusion through the entire surface area of the bubble ($\partial V/\partial t \propto D^3$) fit the data poorly.

Because the circular etch pillars had flat tops and sides, surface roughness due to pillars occurred only at the pillar edges. These narrow edges comprised a negligible fraction of the total surface roughness observed in Fig. 4.1(a). Furthermore, the bubble growth mechanism does not explain the formation of the bright areas observed on top of circular pillars, as seen in Fig. 4.1(a) and (b). To determine the major source of surface roughening, smaller features were examined.

4.2.2. Circular Etch Pits

Bubble coalescence produced complicated morphological structures, such as the curved arrays of circular features at the boundaries of pillars shown in Fig. 4.1(d). The

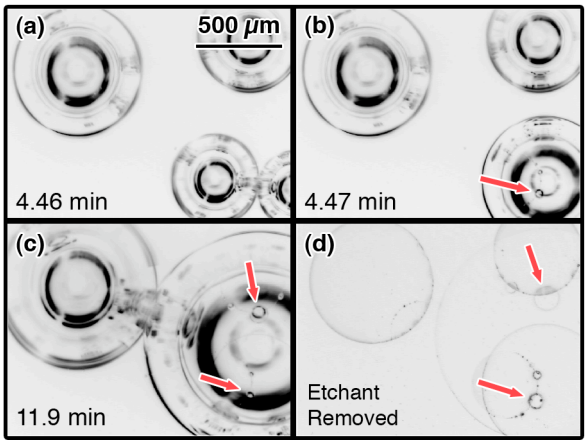

Figure 4.5. Frames from a dark-field videomicrograph (inverted for contrast) of H_2 bubbles growing on a Si(100) surface during $NH_4F(aq)$ etching. Etch times (labeled) were measured from the addition of etchant. The red arrows in (b) and (c) indicate etchant droplets trapped underneath H_2 bubbles during coalescence events. The etch pits resulting from the trapped etchant are indicated by red arrows in (d).

dark-field videomicrographs in Fig. 4.5 show examples of bubble coalescence. The first frame shows two bubbles that had nucleated close to one another and expanded to near touching after 4.46 min of etching. By the next frame, the two bubbles had coalesced and trapped small etchant droplets under the combined gas bubble, as indicated by the arrow in Fig. 4.5(b). The two rightmost bubbles merged a few minutes later (not shown), trapping the etchant droplet indicated by the upper arrow in Fig. 4.5(c). When the bulk etchant was removed, the surface displayed large circular features where H_2 bubbles had resided, corresponding to the pillars described in the previous section. Smaller circular features were arrayed along the periphery of the etch pillars, as indicated by the arrows in Fig. 4.5(d).

The morphology of the small circular structures was investigated by optical profilometry, as illustrated in Fig. 4.6. In contrast to the large etch pillars (>100 μm), which were typically *raised* with respect to the surrounding surface, smaller circular structures (< 100 μm) were typically *depressed*. The circular pits in Fig. 4.6 were cylindrical

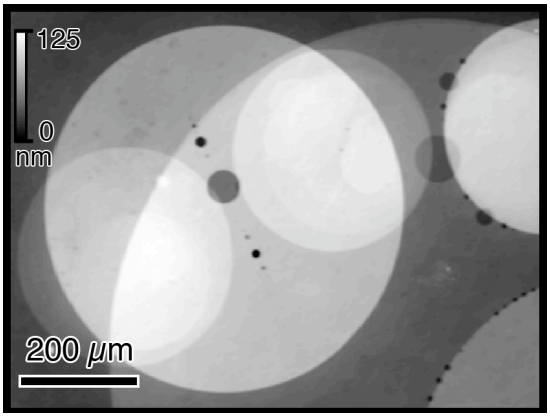

Figure 4.6. Optical profilometry of a Si(100) surface etched for 8 min in $NH_4F(aq)$, showing three roughly symmetric arrays of circular etch pits. The circular pits were formed by droplets that tended to collect at surface imperfections, such as the edge of an etch pillar.

with flat bottoms. Circular pits were attributed to the production of etchant droplets trapped under a H_2 bubble during a coalescence event. These etchant droplets tended to collect at surface ridges or defects, such as the edges of etch pillars, and sometimes formed symmetrical arrays of pits. For example, Fig. 4.6 shows two examples of roughly symmetrical arrays that radiate outwards from a larger, central pit.

Although circular etch pits were more numerous than etch pillars, the pits were not the major component of surface roughness seen in Fig. 4.1 for much the same reason mentioned in the previous section. The sides and bottoms of the cylindrical pits were smooth; therefore, the circular pits could not account for the large bright regions ($>10^6$ μm^2) observed in the dark-field micrographs of roughened surfaces.

4.2.3. Microfaceted etch pits

As illustrated by the dark-field micrograph in Fig. 4.1(e), the tops of circular pillars were covered with numerous micron-scale features. Figure 4.7 shows AFM images of two regions that appeared bright in dark-field microscopy, revealing that the square-shaped features were actually faceted etch pits. The pits in Fig. 4.7 range from flat-

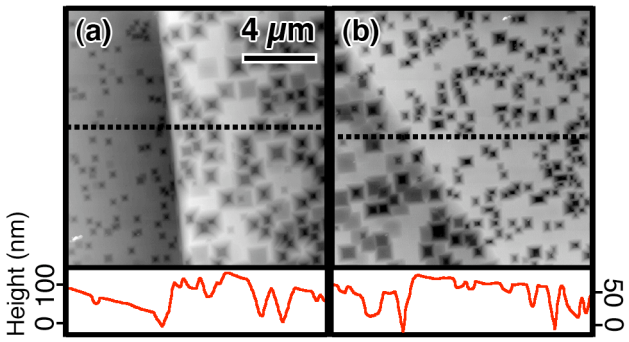

Figure 4.7. AFM images and cross-sections of a Si(100) surface etched for 25 min in $NH_4F(aq)$, showing faceted micropits near pillar boundaries (raised areas). Some micropits are flat-bottomed, whereas others are pyramidal. In all cases, the edges are aligned with <110> directions. The positions of the line profiles are indicated by dashed lines.

bottomed etch pits to nearly perfect inverted pyramids; the square pits were invariably aligned with the high-symmetry <011> directions. The pit size and density were approximately uniform within each bright area, though these parameters varied significantly across morphological boundaries (*e. g.,* pillar edges) and large regions of the surface. For example, the pit size distribution was noticeably different on either side of the pillar boundaries in Fig. 4.7.

The faceted micropits were the major component of bubble-induced surface roughness. For example, the micropits in Fig. 4.7(b) covered approximately 30% of the upper plateau and 50% of the entire image. The spacing between individual pits was often as small as several hundred nm. Micropits were primarily concentrated on top of circular etch pillars; however, many roughened domains were not completely circular and were only an arc or a semi-circle, as illustrated by some of the bright regions in Fig. 4.1(a) and (b).

Individual etch pits were too small to observe *in situ* with optical microscopy. In spite of this limitation, dark-field microscopy during etching provided indirect evidence for micropit formation. For instance, Fig. 4.8 shows six bubbles labeled *A-F* at $t = 0.97$ min, measured from the addition of etchant. Over the next few minutes, several

coalescence events occurred, forming bubbles *EF*, *AB*, and *CD*, in that order. At t = 7.02 min, bubbles *AB* and *CD* coalesced to form the large bubble *ABCD*. After ~15 min of etching, a hazy patch appeared at the former position of bubble *AB*, indicated by the yellow arrow in Fig. 4.8. The etchant was removed after 19 min of etching and the surface morphology imaged. Only some of the pillar tops appeared rough under dark-field microscopy, namely *AB*, *ABCD*, and *EFG*. The top of the pillars left by

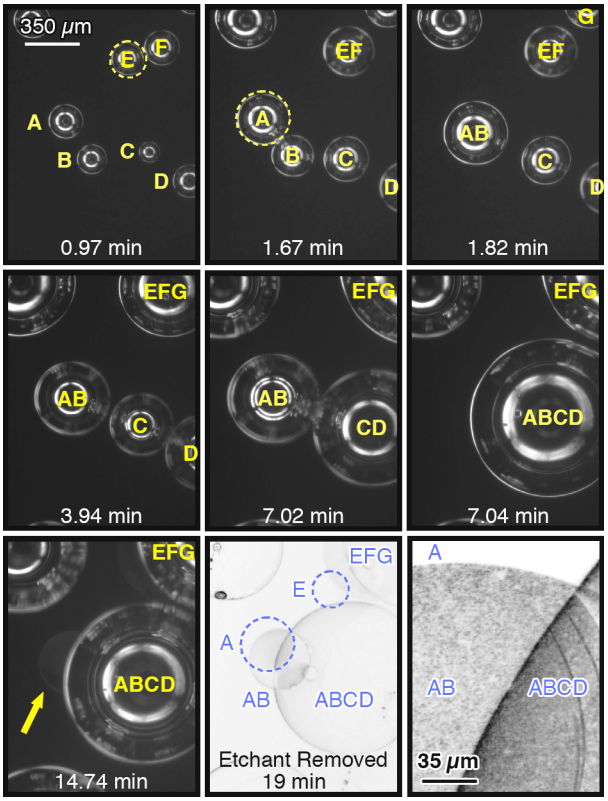

Figure 4.8. Dark-field videomicrography of H_2 bubbles growing on a Si(100) surface during $NH_4F(aq)$ etching. The last two frames are inverted to enhance contrast. Etch times (labeled) were measured from the addition of etchant. The dashed circles mark the greatest extent of the isolated bubbles *A* and *B* before they coalesced. The arrow highlights the area that was once underneath *AB*. After 19 min of etching, the etchant was removed. The areas originally under bubble *A* and *E* remained smooth, whereas those underneath *AB* and *ABCD* were roughened.

bubbles *E* and *A* remained smooth, except for where their areas overlapped with the contact regions of bubbles formed by subsequent coalescence events.

Observations of many samples during etching revealed two requirements for micropitting. The presence of a single bubble was not a sufficient condition for the formation of micropits, rather, two or more bubbles had to coalesce. In addition, the surface under the new bubble had to be re-exposed to the bulk etchant, which occurred only if the bubble dislodged or migrated from its original position. A mechanism for the production of microfaceted etch pits is described in Section 4.3.2.

4.2.4. Bubble-induced roughening of Si(111) and Si(110)

Samples of Si(111) and Si(110) were also etched in quiescent $NH_4F(aq)$ to test the generality of the Si(100) results. Bubble-induced roughening of Si(100) produced two main types of morphological features—circular structures and faceted pits with the same

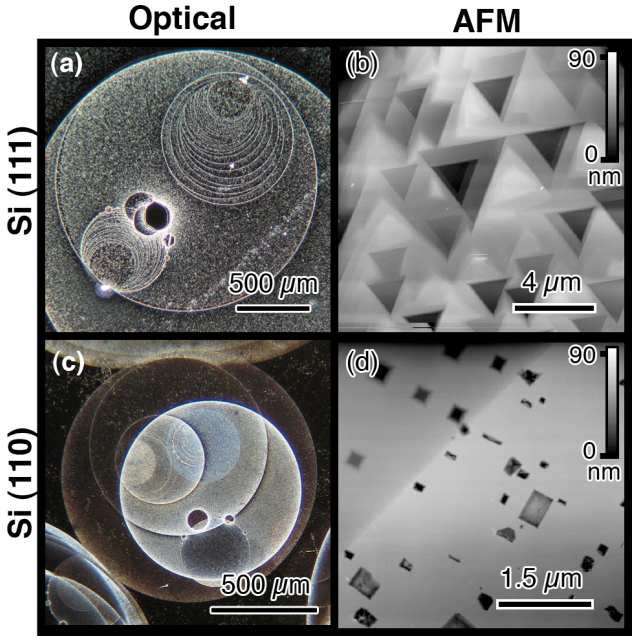

Figure 4.9. Dark-field optical micrographs of a (a) Si(111) and (c) Si(110) surface etched for 70 min in $NH_4F(aq)$ display similar circular etch features, whereas AFM images of micropits on (b) Si(111) and (d) Si(110) surfaces display triangular and rectangular habits, respectively.

four-fold rotational symmetry as the macroscopic Si(100) surface. In contrast, Si(111) and Si(110) surfaces have three-fold and two-fold rotational symmetry with respect to the surface normal.

Figure 4.9 shows examples of Si(111) and Si(110) surfaces etched for 70 min in quiescent $NH_4F(aq)$. The dark-field micrographs for Si(111) in Fig. 4.9(a) and Si(110) in Fig. 4.9(c) displayed circular regions of varying microscale roughness and concentric circular structures, similar to those shown in Figs. 4.1(a), (b), and (c). The morphology of large circular pillars and pits ($\geq 50\ \mu m$) was not affected by the atomic-scale surface structure, but surface symmetry did have a dramatic effect on the shapes of the micron-scale etch pits. In the case of Si(111), shown in Fig. 4.9(b), the etch pits were triangular, with the same three-fold symmetry as the (111) surface. For Si(110), shown in Fig. 4.9(d), the micron-scale pits were less regular but tended towards a rectangular shape.

4.2.5. Bubble suppression methods

Several methods were explored to suppress surface roughening caused by bubble growth and coalescence during etching. After exposure of Si(100) to 40% $NH_4F(aq)$, bubbles typically required ~30 s of etching to reach a sufficient density to coalesce. The simplest method to prevent coalescence was to manually withdraw and reinsert the sample every 15 s. This technique efficiently dislodged bubbles from the surface. Etching experiments as long as 40 min were performed in this manner, and the Si(100) samples

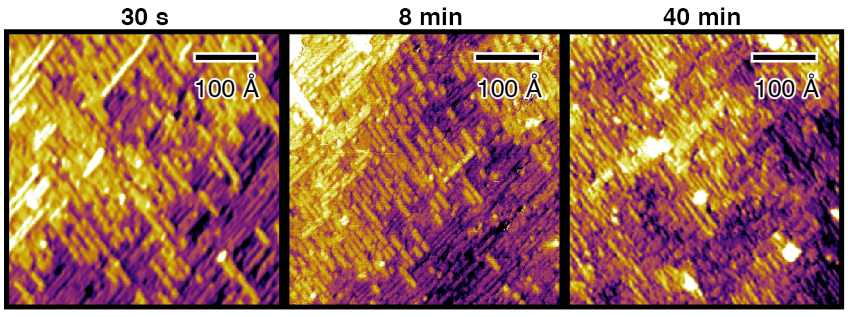

Figure 4.10. STM images of Si(100) samples etched in $NH_4F(aq)$ for 30 s, 8 min, and 40 min using the manual withdrawal technique.

retained surface flatness at all length scales as verified by eye, optical microscopy, AFM, and STM. For example, Fig. 4.10 shows STM images of Si(100) surfaces etched in $NH_4F(aq)$ for 30 s, 8 min, and 40 min using the withdrawal technique. The atomic-scale surface structure was very similar over the range of etch times analyzed, although the sample etched for 40 min had slightly more contamination. Infrared absorbance spectroscopy was also performed on samples etched using the withdrawal technique. Figure 4.11 shows the Cartesian components of the Si–H stretching region spectra for Si(100) etched in $NH_4F(aq)$ for 30 s, 2 min, and 40 min using the withdrawal technique and for a sample etched in quiescent $NH_4F(aq)$ for 1 hr. As discussed in Chapter 3, the spectra of near-atomically-flat, NH_4F-etched Si(100) surfaces display five principal

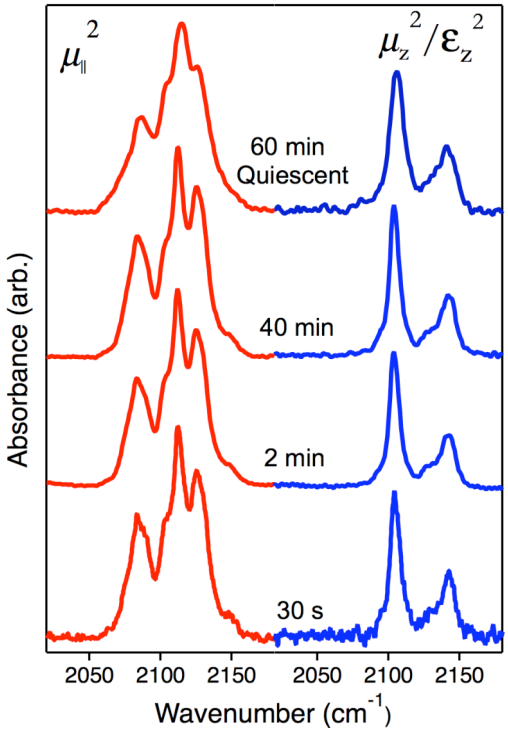

Figure 4.11. Cartesian components of the squared transition dipole moment obtained from infrared absorbance spectra of Si(100) etched in $NH_4F(aq)$ for 30 s, 2 min, and 40 min that were withdrawn through the etchant/air interface every 15 s. The spectrum of a sample etched for 60 min in $NH_4F(aq)$ without withdrawal is shown for comparison.

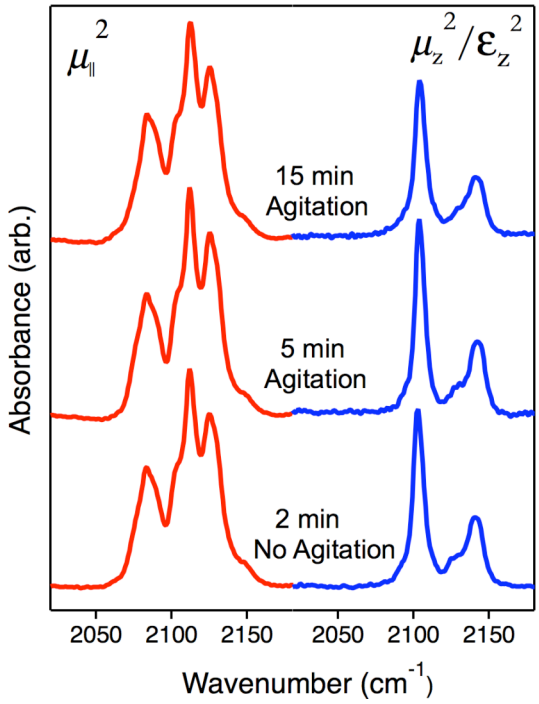

Figure 4.12. Cartesian components of the squared transition dipole moment obtained from infrared absorbance spectra of Si(100) etched in $NH_4F(aq)$ for 2 min, 5 min, and 15 min. The samples etched for 5 min and 15 min were subjected to ultrasonic agitation.

absorbance modes. No significant changes in mode lineshape or energy were observed with etch time for the samples that had been etched with the withdrawal technique. In comparison, the absorbance spectrum of the sample etched for 1 hr in quiescent etchant showed significant mode broadening, which is indicative of increased surface disorder.

A second technique dislodged bubbles through ultrasonic agitation, removing the need for frequent operator intervention. Ultrasonic agitation dislodged the bubbles produced during etching, causing them to stream off the surface. This technique has been previously reported to eliminate pyramid production during elevated-temperature KOH/Si(100) etching,[16,17] though others observed ultrasound-induced defect formation.[18] Figure 4.12 shows infrared absorbance spectra for Si(100) samples etched for 2 min, 5 min, and 15 min in $NH_4F(aq)$, where ultrasonic agitation was employed during the two

longer etches. The spectra for all three samples were nearly identical, indicating that no roughening had occurred even after long etch times. Figure 4.13 compares STM images of a Si(100) surface etched for 2 min in $NH_4F(aq)$ using the withdrawal technique and a Si(100) sample etched for 5 min with ultrasonic agitation. The morphology of the

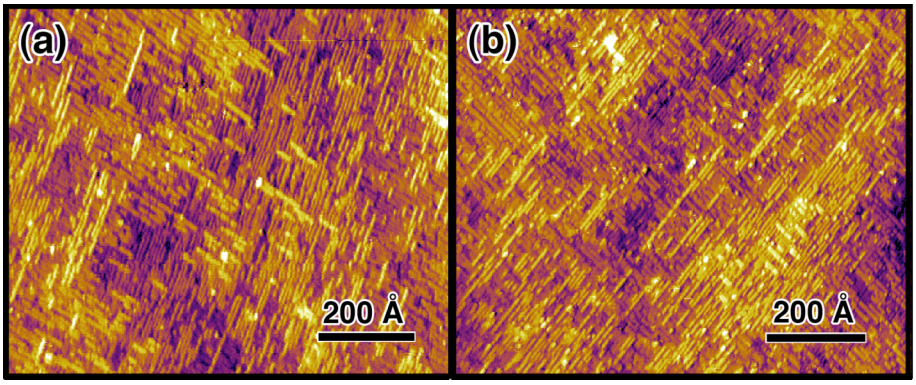

Figure 4.13. STM images of Si(100) etched in $NH_4F(aq)$ for (a) 2 min with periodic withdrawal from the solution and (b) 5 min of ultrasonic agitation with no withdrawal.

surfaces in Figs. 4.13(a) and (b) were very similar despite the different modes of preparation. Finally, dark-field micrographs of Si(100) surfaces etched with ultrasonic agitation were entirely black (not shown), indicating smoothness on larger length scales. At etch times greater than 30 min, the surface of ultrasonically agitated samples developed a mesoscopically rough texture. The texturing created hazy patches on the polished surface and provided nucleation sites for bubbles, which led to further surface roughening.

The possibility of using chemical additives to inhibit bubble-induced roughening was also investigated, with the constraint that any additive must not significantly perturb the etching chemistry. Surfactants have been shown to reduce bubble coalescence;[19] however, prior experience has shown that surfactants significantly alter the anisotropy of etchants.[20] Surfactants are also difficult to fully remove from a surface.

Ionic electrolytes have also been shown to inhibit bubble coalescence. Above a threshold concentration, many inorganic salts inhibit bubble coalescence in aqueous solutions.[21,22] This threshold concentration for coalescence inhibition can vary from as low as 0.01 M for NaCl to over 2 M for $KOOCCH_3$. The mechanism of inhibition remains unclear.[23-25]

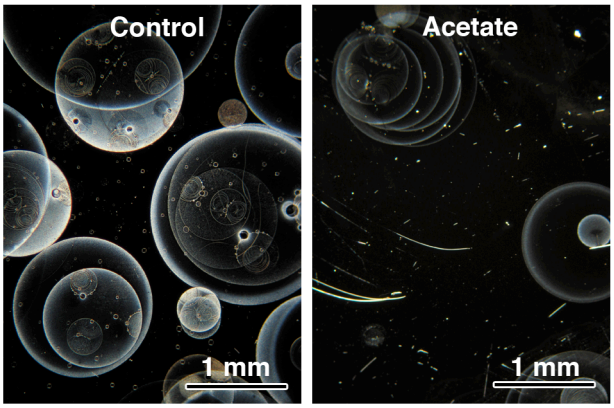

Figure 4.14. Dark-field optical micrographs of a Si(100) surface etched for 1 hr in (left) 40% NH_4F or (right) a 2 M NH_4OOCCH_3, 40% $NH_4F(aq)$ solution showing that added electrolyte suppressed etch-induced roughness.

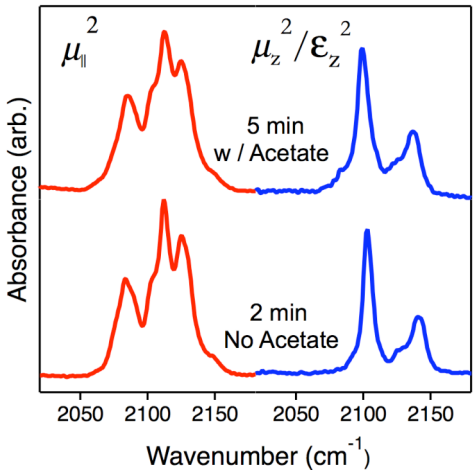

Figure 4.15. Cartesian components of the squared transition dipole moment extracted from infrared absorbance spectra of Si(100) etched in $NH_4F(aq)$ for 2 min with periodic withdrawal through the interface and 5 min in a 2 M NH_4OOCCH_3, 40% $NH_4F(aq)$ solution with no withdrawal.

To test for coalescence inhibition during silicon etching, a variety of electrolytes were added to 40% $NH_4F(aq)$ at concentrations of 1–2 M, including NaCl, LiCl, ammonium phosphate monobasic ($NH_4H_2PO_4$), ammonium citrate dibasic ($(NH_4)_2HC_6H_5O_7$), and ammonium acetate (NH_4OOCCH_3). Empirically, only ammonium acetate was effective at reducing bubble formation and preserving a flat surface morphology. Figure 4.14 compares dark-field micrographs of two Si(100) surfaces etched for 1 hr in 40% $NH_4F(aq)$ with and without acetate. Although roughening was evident on both surfaces, the acetate-enhanced etchant produced a significantly smoother surface with fewer circular pillars and micropitted areas.

The chemical composition of the etched surface was not affected by the addition of acetate. Figure 4.15 shows infrared spectra for samples etched for 2 min in $NH_4F(aq)$ and 5 min in quiescent acetate-enhanced etchant. Although the spectrum for the surface etched in the acetate-enhanced solution was slightly broadened relative to the $NH_4F(aq)$-etched surface spectrum, the positions and intensities of the five prominent absorbance bands were similar in both spectra. No modes indicative of surface roughening were observed after acetate-enhanced etching.

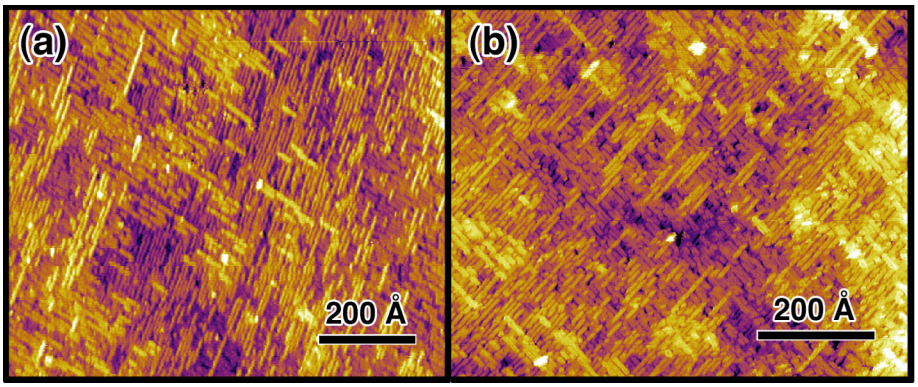

Figure 4.16. STM images of Si(100) etched in $NH_4F(aq)$ for (a) 2 min with periodic withdrawal from the solution and (b) 2 min in a ~2 M NH_4OOCCH_3, 40% $NH_4F(aq)$ solution with no withdrawal.

Furthermore, the addition of acetate to the etchant did not alter the atomic-scale morphology. Figure 4.16 shows STM images of Si(100) etched in $NH_4F(aq)$ with and without acetate; both display similar morphologies. As determined by gravimetric analysis, the acetate-enhanced solution had a Si(100) etch rate approximately 40% slower than that of pure 40% $NH_4F(aq)$ (0.93 monolayer/s vs. 1.55 monolayer/s, respectively). Decreased surface roughness from acetate addition could not be attributed solely to the difference in the etch rate, because Si(100) surfaces etched in the acetate-enhanced solution for 1 hr were still smoother than surfaces etched for 30 min in quiescent, pure 40% $NH_4F(aq)$ (not shown).

Although these experiments demonstrated the potential of chemical additives for suppressing bubble-induced roughness, mechanical methods for removing bubbles were consistently more effective at preventing roughness at all length scales.

4.3. Discussion

Si(100) surfaces etched with $NH_4F(aq)$ for short etch times ($\leq$ 2 min) or with mechanical H_2 bubble removal were near-atomically smooth. When bubbles were allowed to accumulate during etching, a variety of circular and four-fold symmetric features roughened the surface on length scales ranging from tens of nanometers to millimeters. Two mechanisms are proposed to explain the origin of these features.

4.3.1. Mechanism for production of concentric circular etch features

A mechanism for the production of surface roughness by etching-generated bubbles was first proposed by Palik *et al.* to explain roughening observed during KOH etching of Si(100).[26] In their "pseudomasking" model, a H_2 bubble nucleates on the surface after local H_2 supersaturation of the etchant. The bubble temporarily protects the underlying surface from the etchant as the surrounding silicon is etched away, forming a bubble-capped pillar. As the bubble grows in volume, the buoyant force becomes large

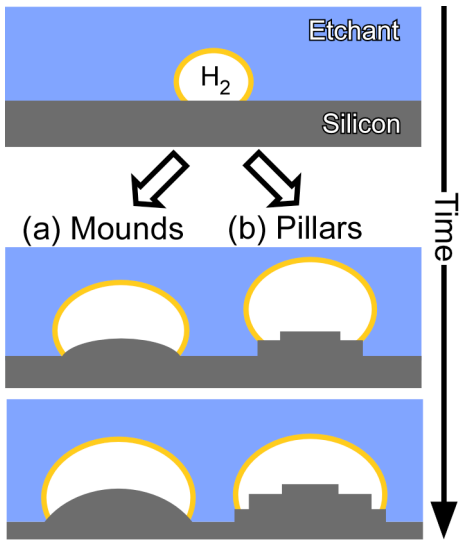

Figure 4.17. Mechanism for the production of circular etch pillars and mounds. (a) If the contact diameter of the bubble grows continuously, a shallow mound forms under the bubble. (b) If the contact diameter grows discontinuously, nested pillars form a wedding-cake structure.

enough to overcome the adhesive force, and the H_2 bubble eventually dislodges and floats away. The Palik *et al.* pseudomasking model assumes that the bubble contact region remains pinned during etching and does not expand. Thus, their model explains isolated etch pillars.

A modified pseudomasking model is proposed to explain the nested circular pillars observed on Si(100) etched in quiescent $NH_4F(aq)$, as illustrated in Fig. 4.1(c). During nucleation and the early stages of growth, bubble contact widths grew continuously, as observed in Fig. 4.4(b) for $t < 79$ s. Because the contact region was not pinned, the continuous expansion of the bubble diameter presumably led to the production of rounded hills, shown schematically in Fig. 4.17(a). In later stages of growth, the bubble contact area remained roughly constant and grew only during rapid expansion events, such as those shown in Figs. 4.3 and 4.4. After each expansion, the contact area remained pinned until the next event, leading to a stacked "wedding-cake" structure, as

depicted in Fig. 4.17(b). This stacked structure corresponds to the nested circular features seen in Figs. 4.1(a) and (c) by top-view, dark-field microscopy.

Although the incorporation of two H_2 bubble growth modes into the pseudomasking model describes the origin of circular pillars observed on the etched surface, it does not explain the origin of the discontinuous growth events. On a smooth surface, gas bubbles are expected to grow continuously without contact line pinning, as is the case for the evaporation of water droplets on mica and silicon surfaces;[26] however, surface roughness and heterogeneity are known to cause contact line pinning.[27]

A model for discontinuous bubble growth is shown schematically in Fig. 4.18. In the first step, illustrated by Fig. 4.18(a), a small bubble nucleates and grows continuously until it is pinned by a surface defect (*e. g.,* a scratch mark, a particle). For instance, the dark-field micrograph in Fig. 4.1(c) shows a particle located at the periphery of the innermost circle (yellow arrow), which is consistent with the particle functioning as an initial pinning site. At the moment of pinning, the contact angle between the bubble and the surface will be the receding contact angle θ_r, which is determined by the silicon-etchant and etchant-vapor surface energies as well as by the wetting hysteresis.[28] While the bubble is pinned, a circular pillar is produced as depicted in Fig. 4.18(b). During this time, H_2 will continue to diffuse into the bubble. The bubble volume grows, decreasing the contact angle and the work of adhesion while increasing the elastic energy of the bubble. Two outcomes are possible. If the buoyant force exceeds the force of adhesion, the bubble will detach. In Fig. 4.18(c), the second possibility is shown, in which the elastic energy overcomes the pinning force. In this case, the bubble rapidly expands, depins from the edge of the etch pillar, and spreads onto the surrounding surface. The new contact angle cannot be exactly predicted because of the wetting hysteresis,[29] but will be between the advancing and receding contact angles, θ_a and θ_r—a 30° range for hydrogen-terminated silicon.[30] As depicted in Fig. 4.18(d), the contact angle of the bubble will

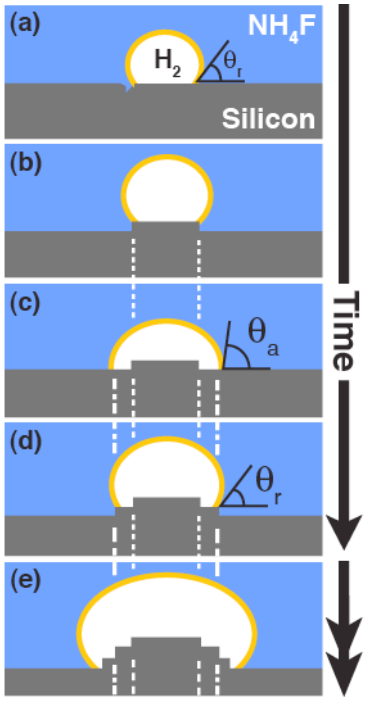

Figure 4.18. Mechanism for the production of nearly-concentric, circular etch pillars. (a) The contact line of a growing bubble becomes pinned at a surface defect, (b) leading to the formation of an etch pillar. As the bubble grows, (c) the contact angle eventually depins, (d) creating another etch pillar. Oscillatory growth continues, (e) producing a wedding-cake structure.

shrink to θ_r as the bubble volume continues to grow. If the contact line is stationary long enough to produce another etch pillar, the bubble will be pinned by the pillar, and the cycle will start over. In this way, the bubble will continue to produce its own pinning sites, initiating an oscillatory growth pattern. Figure 4.18(e) shows the expected result of several growth cycles.

This proposed mechanism explains the observation of discontinuous bubble growth and the formation of nested circular features. After nucleation, bubbles grow continuously until they become pinned on a surface defect. Because of contact angle hysteresis and bubble masking, an oscillatory growth phase ensues that produces the

approximately concentric pillars. Finally, when the buoyant force exceeds the force of adhesion, the bubble will detach from the surface.

In addition to raised circular etch pillars, other morphological features have been attributed to masking by H_2 bubbles. Several authors have proposed that H_2 bubbles are responsible for the formation of pyramidal hillocks during KOH etching of Si(100),[31,32] although no raised pyramids were observed for the NH_4F-etched surfaces reported here.

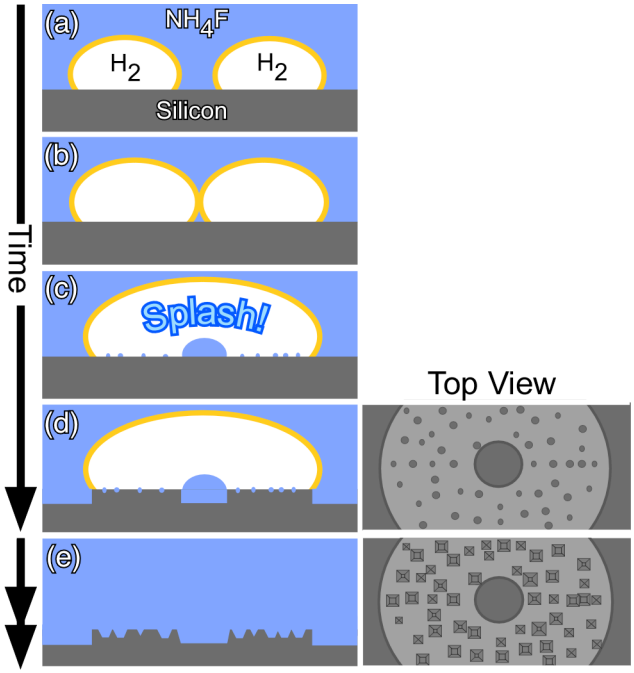

Figure 4.19. Mechanism for the formation of circular and faceted etch pits. (a) Two bubbles grow on the silicon surface until (b) their interfacial regions come into contact and (c) they coalesce, trapping both micron-scale droplets at the merger boundary and spreading tiny droplets across the surface. (d) The droplets continue etching, producing circular pits when viewed from above. (e) After the bubble dislodges and re-exposes the surface to the bulk etchant, the smaller pits rapidly become faceted, while the micron-scale circular etch pits remain relatively unaltered.

4.3.2. Mechanism for production of microfaceted pits

A different model involving bubble coalescence, schematically shown in Fig. 4.19, is proposed to explain the formation of micron-scale faceted etch pits. After nucleation, two initially separated bubbles, shown in Fig. 4.19(a), grow until they contact one another, as depicted in Fig. 4.19(b). The two bubbles then coalesce, splashing small etchant droplets over the area of the surface underneath the new bubble, as illustrated in Fig. 4.19(c). Trapped etchant droplets were observed in support of this mechanism. For example, several trapped droplets are highlighted by the red arrows in Fig. 4.5. The droplets formed during coalescence tended to collect at areas of high surface relief (*e. g.,* scratches, pillars) and etched the surface underneath the droplet to produce circular etch pits, such as those seen in Figs. 4.1(d) and 4.6.

Because bubble coalescence was observed to trap larger etchant droplets that lead to circular etch pits, it was hypothesized that the merger process also produces smaller droplets that then etch sub-micron-scale circular pits, depicted schematically in Fig. 4.19(d). If the tiny circular etch pits are re-exposed to the etchant (*e. g.,* by bubble departure), the pits would be anisotropically etched by the bulk etchant, as depicted in Fig. 4.19(e). When an arbitrary concave surface is exposed to an anisotropic etchant, the feature will quickly etch until the slow-etching faces are exposed.[33] On the Si(100) surface, concave features will eventually evolve to tetrahedral pits defined by {111} facets. Micropits with flat bottoms, also seen in Fig. 4.7, represent an intermediate geometry between spherical and faceted pits. This micropit formation mechanism explains the four-fold symmetric faceted pits seen on Si(100), the three-fold symmetric pits observed on Si(111), and the roughly two-fold symmetric pits on Si(110).

In contrast to these faceted structures, larger droplets of trapped etchant produced circular pits, as depicted in the top view of Figs. 4.19(d) and (e). For the experiments reported here (with etch times $\leq$ 70 min), pits larger than ~20 μm remained

circular because insufficient time elapsed for the etchant to transform the cylindrical pit into a faceted structure.

The origin of the micron-scale etchant droplets could not be conclusively determined; however, one of two possible mechanisms seems likely. The microdroplets may be atomized etchant that has been splashed across the surface by the energetic coalescence process. The gradated distribution of micron-scale etch pits seen in micrographs lends support to the splashing mechanism, as the density of droplets varied with proximity to the coalescing interface. For example, some of the bright micropit-roughened regions in Fig. 4.1(a) did not have uniform color or contrast and were often brightest at their periphery. Alternatively, a thin etchant film trapped between the bubbles may bead up into small droplets as it de-wets the surface. Spinodal dewetting of ultrathin aqueous films can lead to the spontaneous formation of sub-micron patterns under some conditions.[34] This phenomenon has been used to deposit uniform arrays of particles.[35]

To distinguish between the two mechanisms, a small amount of polyethylene oxide was dissolved in the etchant. This polymer has been shown to suppress the breakup of water droplets during collisions with hydrophobic surfaces.[36,37] Unfortunately, the polyethylene oxide was not soluble in 40% $NH_4F(aq)$ at concentrations high enough to affect the observed patterns of bubble-induced roughness. Attempts to use higher concentrations led to the formation of dendritic precipitates on the silicon surface.

4.3.3. Explanation for etching-induced Si{111} microfacets

As discussed in the introduction to Chapter 3, the conventional wisdom in the field of silicon etching was that most wet-chemical etchants, including $NH_4F(aq)$, progressively roughen Si(100) surfaces, in part by promoting the formation of Si{111} facets. In this chapter, infrared absorbance spectroscopy and STM imaging showed that Si(100) surfaces etched in $NH_4F(aq)$ had a near-atomically smooth morphology for etch times up to 40 min when bubbles were removed, indicating that roughening was not

inherent to the etchant. How can this discrepancy be explained? On one hand, the absorbance spectra in Ref. 11, Fig. 4.11, and Fig. 4.12 were essentially identical to those obtained by Dumas *et al.* after 3 min of etching Si(100) in $NH_4F(aq)$,[12] suggesting that Dumas *et al.* produced similarly smooth morphologies (even though they attributed the spectra to a rough surface). In contrast, the four spectra noted above are very different from those reported by Niwano *et al.*[14] and by Nakamura *et al.*,[38] who both found convincing spectroscopic evidence for {111} microfacet formation after longer $NH_4F(aq)$ etching times of 14 min and 180 min, respectively.

The conflicting data can be reconciled in terms of bubble-induced roughening. In the cases where short etch times were studied, such as in Dumas *et al.,* and where bubbles were scrupulously removed, such as in Clark *et al.*, the etched surface was near-atomically smooth. In contrast, the long etch times in quiescent $NH_4F(aq)$ studied by Niwano *et al.* and Nakamura *et al.* would have allowed ample time for micron-scale pitting to occur. The non-imaging techniques used to characterize these surfaces [*e. g.,* thermally programmed desorption (TPD), reflection high-energy electron diffraction (RHEED), infrared absorbance spectroscopy] would not have been able to detect the large circular etch pillars that are easily imaged in dark-field microscopy. On the other hand, hydrogen adsorbed on the {111}-faceted micropits would be readily observable in infrared absorption spectroscopy, leading Niwano *et al.* and Nakamura *et al.* to the incorrect conclusion that NH_4F etching of Si(100) is intrinsically responsible for the formation of {111} facets.

Finally, it should be noted that although the spectra in Niwano *et al.* and Nakamura *et al.* were dominated by the {111} absorbance mode, the spectra in both works showed two additional modes that have been previously assigned to {110} facets. It is not yet clear if the mechanism described in Section 4.3.2 can explain the production of microfaceted etch pits with significant {110} character; thus, the evidence for {110}-

faceting in Niwano *et al.* and Nakamura *et al.* may be more consistent with pyramid formation than with pitting. Although no pyramids were observed in the experiments reported here, the mechanisms for etching-induced pyramid formation on Si(100) are currently under investigation.

4.4. Conclusions

When Si(100) surfaces were etched in quiescent NH_4F solutions, H_2 gas produced by the etching reaction formed bubbles on the etching surface. These bubbles perturbed the etching reaction in a number of ways, producing complicated morphologies with circular pillars, circular pits, and microfaceted etch pits. Masking of the etching surface by H_2 bubbles explained the formation of circular pillars. Occasionally, the growing bubbles were pinned by a surface inhomogeneity, which induced a periodic motion that produced a "wedding-cake" structure of nested pillars. Etch pits of both circular and faceted morphologies were attributed to droplets of etchant trapped underneath bubbles during coalescence events. The production of micron-scale, faceted etch pits was attributed to the anisotropic etching of initially circular etch pits. As a result, the shape of the micron-scale etch pits was dependent on the surface symmetry. Etched Si(100) surfaces displayed square-pyramidal etch pits, whereas Si(111) and Si(100) surfaces displayed triangular and rectangular etch pits, respectively.

Three techniques for bubble suppression were investigated: manual withdrawal of the sample through the air/liquid interface, ultrasonic agitation, and the addition of an electrolyte. All three methods suppressed roughening, but the simple withdrawal technique was found to be the most effective.

These observations reconcile the apparently contradictory conclusions of previous investigations which showed that $NH_4F(aq)$ etching of Si(100) produces near-atomically flat surfaces or very rough, microfaceted surfaces. The anisotropic etching reactions inherent to NH_4F etching produce near-atomically flat surfaces; however, the

H_2 bubbles—a product of the etching reaction—disrupt this process, producing roughness at many length scales. Although microfacet formation is *not* inherent to the atomic-scale reactions of the NH_4F etchant, bubble-induced roughening can produce microfaceted etch pits over a significant fraction of the surface.

REFERENCES

[1] W. Kern, in *Handbook of Silicon Wafer Cleaning Technology*, 2nd ed., edited by K. A. Reinhardt and W. Kern (William Andrew Inc., 2008), p. 3-92.

[2] T. Ohmi, K. Kotani, A. Teramoto, and M. Miyashita, IEEE Electron Device Letters **12,** 652-654 (1991).

[3] G. S. Higashi, Y. J. Chabal, G. W. Trucks, and K. Raghavachari, Applied Physics Letters **56,** 656-658 (1990).

[4] P. Allongue, Physical Review Letters **77,** 1986-1989 (1996).

[5] S. P. Garcia, H. Bao, and M. A. Hines, Physical Review Letters **93,** 166102-1 - 166102-4 (2004).

[6] K. R. McIntosh and L. P. Johnson, Journal of Applied Physics **105,** 124520-1 - 124520-10 (2009).

[7] C. J. Wu, P. J. Wei, and J. F. Lin, Journal of Micromechanics and Microengineering **19,** 115015-1 - 115015-7 (2009).

[8] C. J. Wu, P. J. Wei, and J. F. Lin, Journal of Micromechanics and Microengineering **19,** 125019-1 - 125019-6 (2009).

[9] W. T. Wang, N. Lu, J. Y. Hao, H. B. Xu, D. P. Qi, and L. F. Chi, Journal of Physical Chemistry C **114,** 1989-1995 (2010).

[10] M. A. Hines, International Reviews in Physical Chemistry **20,** 645-672 (2001).

[11] I. T. Clark, B. S. Aldinger, A. Gupta, and M. A. Hines, Journal of Physical Chemistry C **114,** 423-428 (2010).

[12] P. Dumas, Y. J. Chabal, and P. Jakob, Surface Science **269/270,** 867-878 (1992).

[13] V. L. Thanh, D. Bouchier, and G. Hincelin, Journal of Applied Physics **87,** 3700-3706 (2000).

[14] M. Niwano, Y. Takeda, Y. Ishibashi, K. Kurita, and N. Miyamoto, Journal of Applied Physics **71,** 5646-5649 (1992).

[15] V. Palermo, E. Susi, and D. Jones, Journal of the Electrochemical Society **151,** G554-G558 (2004).

[16] T. Baum and D. J. Schiffrin, Journal of Micromechanics and Microengineering **7,** 338-342 (1997).

[17] T. Baum, J. Satherley, and D. J. Schiffrin, Langmuir **14,** 2925-2928 (1998).

[18] D. G. Schimmel, Journal of the Electrochemical Society **126,** 479-483 (1979).

[19] J. Lee, S. E. Kentish, and M. Ashokkurnar, Journal of Physical Chemistry B **109,** 5095-5099 (2005).

[20] R. A. Wind and M. A. Hines, (unpublished results).

[21] V. S. J. Craig, B. W. Ninham, and R. M. Pashley, Journal of Physical Chemistry **97,** 10192-10197 (1993).

[22] V. S. J. Craig, B. W. Ninham, and R. M. Pashley, Nature **364,** 317-319 (1993).

[23] L. A. Deschenes, J. Barrett, L. J. Muller, J. T. Fourkas, and U. Mohanty, Journal of Physical Chemistry B **102,** 5115-5119 (1998).

[24] Y. H. Tsang, Y. H. Koh, and D. L. Koch, Journal of Colloid and Interface Science **275,** 290-297 (2004).

[25] H. K. Christenson, R. E. Bowen, J. A. Carlton, J. R. M. Denne, and Y. Lu, Journal of Physical Chemistry C **112,** 794-796 (2008).

[26] R. D. Deegan, Physical Review E **61,** 475-485 (2000).

[27] R. E. Johnson and R. H. Dettre, Journal of Physical Chemistry **68,** 1744-& (1964).

[28] Y. L. Chen, C. A. Helm, and J. N. Israelachvili, Journal of Physical Chemistry **95,** 10736-10747 (1991).

[29] L. C. Gao and T. J. McCarthy, Langmuir **22,** 6234-6237 (2006).

[30] J. G. Park and S. Raghavan, Journal of Adhesion Science and Technology **7,** 179-193 (1993).

[31] S. A. Campbell, K. Cooper, L. Dixon, R. Earwaker, S. N. Port, and D. J. Schiffrin, Journal of Micromechanics and Microengineering **5,** 209-219 (1995).

[32] H. Schroder, E. Obermeier, and A. Steckenborn, Journal of Micromechanics and Microengineering **9,** 139-145 (1999).

[33] M. Elwenspoek and H. V. Jansen, *Silicon Micromachining* (Cambridge University Press, New York, 1998).

[34] U. Thiele, M. Mertig, and W. Pompe, Physical Review Letters **80,** 2869-2872 (1998).

[35] L. V. Govor, G. Reiter, G. H. Bauer, and J. Parisi, Physical Review E **74,** 041609-1 - 041609-9 (2006).

[36] V. Bergeron, D. Bonn, J. Y. Martin, and L. Vovelle, Nature **405,** 772-775 (2000).

[37] V. Bergeron and D. Quere, Physics World **14,** 27-31 (2001).

[38] M. Nakamura, M.-B. Song, and M. Ito, Electrochimica Acta **41,** 681-686 (1996).

Chapter 5

Modeling the Vibrational Spectrum of H-Terminated Silicon with Density Functional Theory

The materials used in semiconductor microelectronics are extremely pure; therefore, device properties are typically limited by surface or interfacial defects, not bulk defects.[1] The techniques used to process silicon—the substrate of choice—have been meticulously designed to produce the cleanest and smoothest surface possible, but the shrinking dimensions of microelectronic devices place increasingly stringent requirements on these surfaces. Hydrofluoric-acid-based (HF-based) etchants are commonly used in industrial processing to etch silicon wafers roughened and oxidized by harsh cleaning solutions.[2] These HF-based etchants remove oxidized silicon and passivate the surface with a monolayer of covalently-bound hydrogen.[3] Understanding the chemical composition and morphology of HF-etched silicon surfaces is therefore critical to developing a rational methodology.

Infrared absorption spectroscopy has emerged as one of the most productive techniques for analyzing hydrogen-terminated silicon surfaces (H/Si). Vibrational absorption spectroscopy has several advantages over other methods, including sub-monolayer sensitivity and the ability to obtain information on the orientation of surface adsorbates through the use of polarized light. This technique has led to many advances in the understanding of silicon cleaning, etching, and oxidation, including the discovery of extremely anisotropic etchants capable of producing atomically-flat H/Si(111)[3] and H/Si(110).[4]

One of the principal challenges in the analysis of vibrational spectra is the assignment of the observed absorption bands to the vibrational modes of specific surface species. These assignments are made on the basis of several analysis strategies. The mode

energy alone is sufficient for the assignment of simple spectra, such as the spectrum of atomically-flat H/Si(111) with one Si–H stretching mode and one Si–H bending mode.[3] Additionally, isotopic energy shifts can be used to confirm the involvement of light species (typically H). Isotopic substitution can also simplify vibrational spectra. For instance, dihydride species typically have two coupled modes—the antisymmetric and symmetric vibrations. At low isotopic substitution (e.g., 25% H: 75% D), the coupled vibrations coalesce to a single mode—an isolated Si–H stretch.[5] The mode polarization is another useful tool for spectral assignment, because polarization can be used to obtain structural information. For instance, the polarization of step modes was used to determine the step structure of vicinal Si(111) surfaces.[6] The major challenge to these experimental assignment strategies comes from spectra with many overlapping modes. In these cases, miscut surfaces can be used to increase the concentration of particular defects. For example, buffered-HF-etched Si(111) surfaces have steps that are primarily terminated by either monohydrides or dihydrides, depending on the miscut direction.[6,7] By increasing the miscut angle, the absorbance of the desired step species can be increased relative to that of the terrace mode. In spite of these varied techniques, experimental analysis alone is not always sufficient for assigning vibrational modes.

Computational models have been used to confirm the assignments of vibrational modes and to predict the modes of postulated structures. For instance, the relative mode energies and energy splittings calculated for trisilane were used in the initial interpretation of HF-etched Si(111) and Si(100) spectra,[5] and later theoretical work confirmed the assignment of H/Si(111) step modes.[8] Calculations were also used to assign the modes of oxidized silicon species observed after the decomposition of H_2O on clean Si(100)-(2 × 1) surfaces[9] and to predict the mode intensities for some of these oxidized species.[10] More recently, computational studies have confirmed that the observed shifts in the H/Si(111) stretch vibration with chlorine cofunctionalization are due to an inductive effect.[11]

In contrast to H/Si(111), the H/Si(100) surface has presented a much greater challenge for vibrational energy calculations. Early theoretical work on Si(100) focused on possible reconstructions of H/Si(100). The simplest H/Si(100) surface is the 1×1 unreconstructed bulk-terminated surface, in which each surface silicon is bound in a tetrahedral geometry to two hydrogens. The hydrogens of neighboring dihydrides would be only 1.5 Å apart, well below the van der Waals diameter of hydrogen. To relieve this severe interadsorbate strain, Ciraci *et al.* first calculated that the dihydrides would cant on (100) surfaces with high coverage of hydrogen[12] to increase the distance between neighboring dihydrides,[13] as shown in Fig. 3.2. Northrup predicted the vibrational modes for the canted dihydride surface (CDS),[14] and several researchers have performed similar calculations;[15-19] however, no consensus on the predicted mode energies has been reached. For example, Fig. 5.1 shows the predicted dihydride stretching modes on the CDS as a

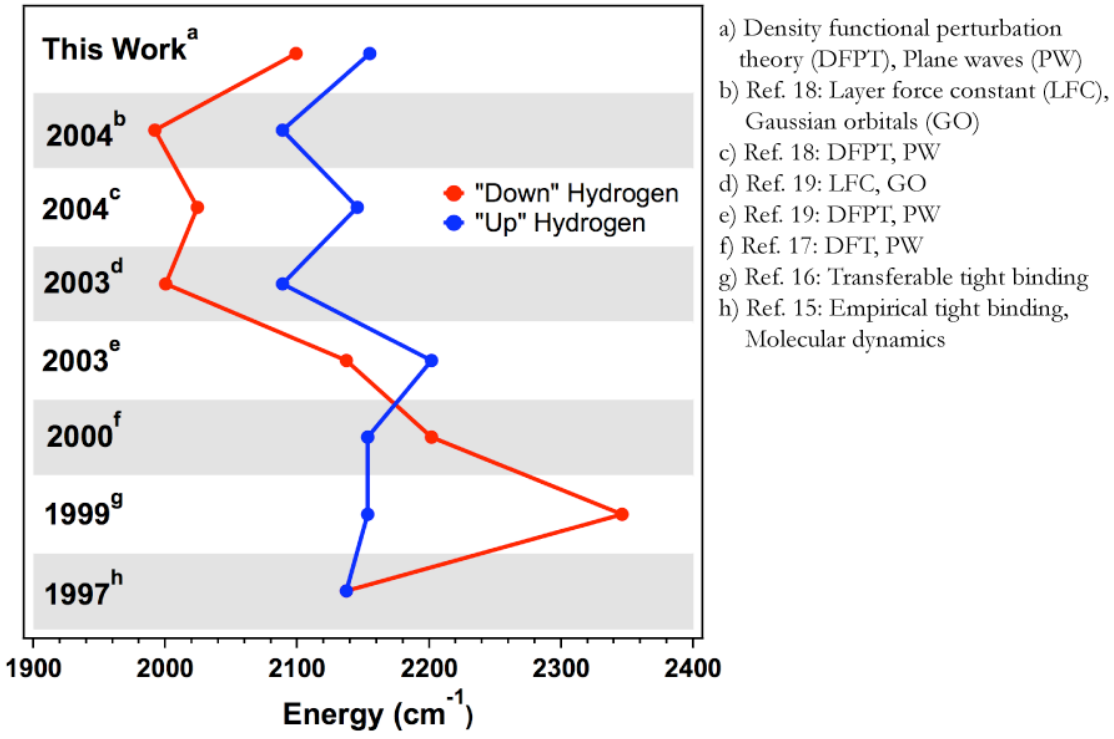

Figure 5.1. Calculated stretching mode energies of canted dihydrides on bulk-terminated H/Si(100) as a function of publication year.

function of publication year. Even for this idealized, periodic system, the predicted "down" mode energy varies by ~350 cm^{-1} between theoretical methods and researchers. Because 1×1 H/Si(100) has never been observed, the accuracy of the calculations cannot be judged.

Until recently, cluster calculations have been the preferred method for vibrational energy calculations. Small clusters are computationally tractable and often yield vibrational energies that correlate well with experiment.[20] To create a cluster model, a small region of surface and near-surface atoms is cleaved from the semi-infinite lattice. Silicon atoms at cleavage sites are typically frozen to their bulk positions and terminated with hydrogen or a "pseudoatom" designed to mimic the bulk electronic environment. This approach may fail if the cluster is too small. For example, cluster calculations on small structures have been shown to allow unrealistic distortions for some systems with a large amount of steric strain.[21] In contrast, the periodic slab structures used in this work avoid complications caused by lateral boundaries and can model surfaces with long-range effects due to interadsorbate strain.

In this study, the vibrational modes and energies of hydrogen-terminated silicon were calculated using density functional perturbation theory (DFPT). To test the accuracy of the model, several theoretically and experimentally well-studied H/Si surfaces were simulated, including the atomically-flat H/Si(111) surface and the two principal step structures of vicinal H/Si(111). The relaxed structure and vibrational energies of the highly-strained, bulk-terminated H/Si(100) surface were then calculated and compared to previous simulations. In addition, the predicted vibrational modes and energies for missing-row H/Si(100) structures were compared to the observed spectrum of NH_4F-etched Si(100). Using canted dihydride rows as a model, the effect of defects on H/Si(100) vibrational energies was explored. Finally, this work concludes with an

assessment of the overall accuracy of theoretical prediction of H/Si surface vibrational energies and, by extension, the vibrational energies of other highly strained systems.

5.1. Theoretical Methods

The vibrational properties of H-terminated silicon were investigated with first-principles calculations using the Vienna *ab initio* simulation package (VASP v. 5.2).[22-24] The program uses density functional theory (DFT) with a plane-wave basis and the projector-augmented wave (PAW) method developed by Blöchl[25] in the implementation of Kresse and Joubert[26] to calculate the energies of periodic atomic systems. The Perdew-Burke-Ernzerhof (PBE) exchange-correlation functional was used for all calculations.[27] The core electrons were described using the hard version of the PAW potentials as supplied with the VASP code, and vibrational energies were calculated using density functional perturbation theory. Convergence of the mode energies with respect to plane-wave basis set size (energy cutoff), *k*-point mesh, vacuum spacing, and slab thickness were tested as described in Section 5.1.1.

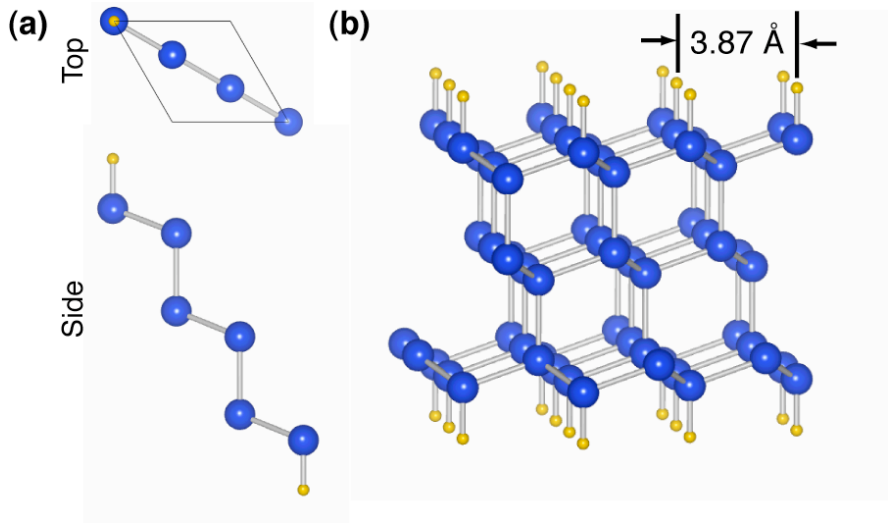

Figure 5.2. (a) The 1 × 1 unit cell used to model flat H/Si(111) surfaces. The top view shows the cell boundaries. (b) A portion of the H/Si(111) surface formed by the unit cell in (a) after relaxation with a 5 × 5 × 2 *k*-point mesh and an 800 eV energy cutoff. Silicon atoms are represented by blue spheres and hydrogen atoms by gold spheres.

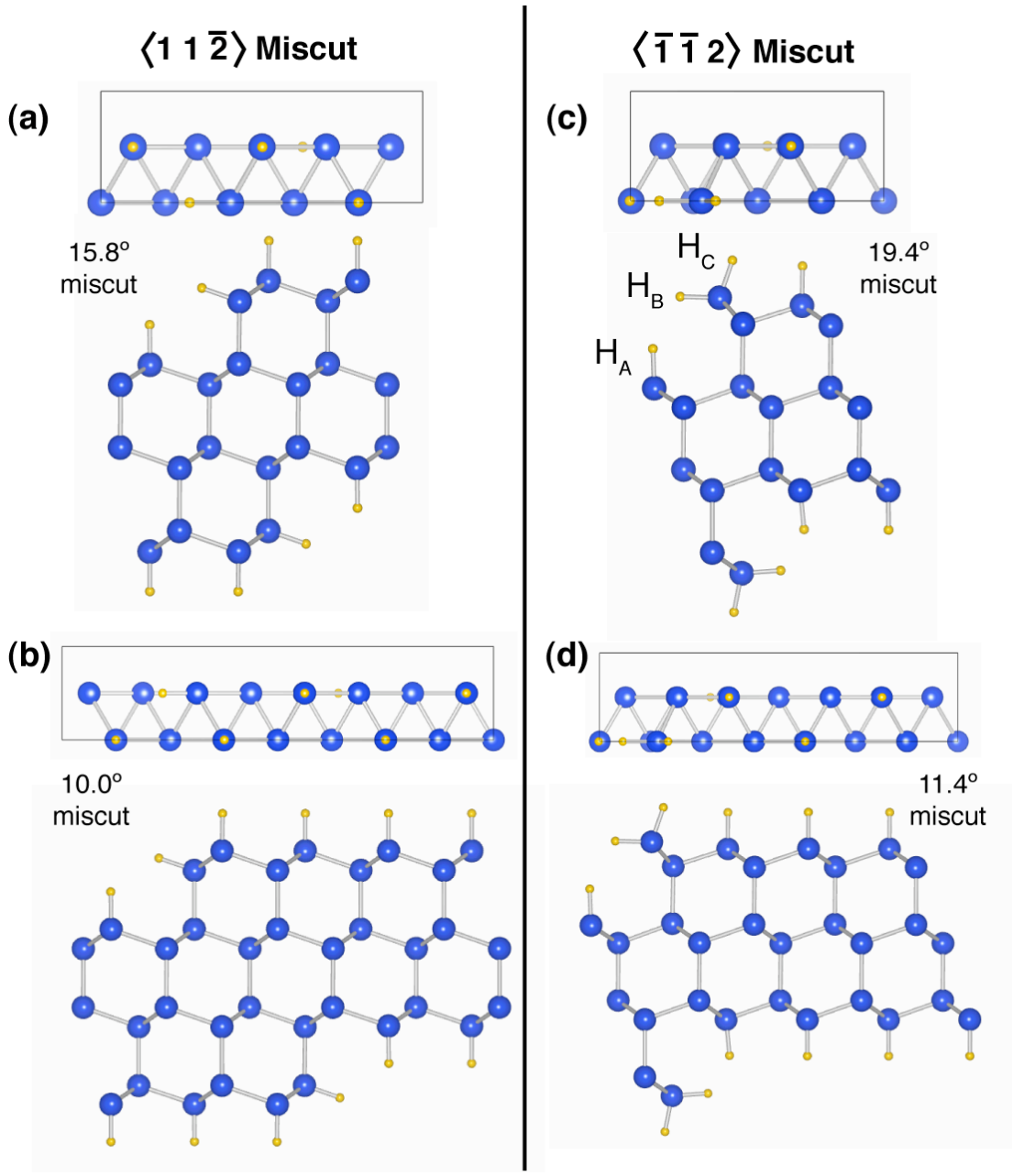

Figure 5.3. Unit cells (shown after relaxation) used to calculate the vibrational frequencies of stepped H/Si(111) surfaces. The cell boundaries are shown in the top views below each structure. (a) Si(111) surface miscut in the $\langle 11\bar{2} \rangle$ direction with two and (b) four terrace monohydrides. (c) Si(111) surface miscut in the $\langle \bar{1}\,\bar{1}\,2 \rangle$ direction with two and (d) four terrace monohydrides. The step dihydride in (c, d) is strained by steric interactions with the lower terrace monohydride. The relaxations were carried out with $2 \times 4 \times 1$ and $1 \times 4 \times 1$ *k*-point meshes for the two and four terrace structures, respectively, with an energy cutoff of 800 eV.

Both flat and miscut H-terminated Si(111) surfaces were studied. The flat H/Si(111) surface was modeled with a hexagonally-symmetric slab. Figure 5.2(a) shows a typical H/Si(111) unit cell used to model the bulk-terminated H/Si(111) surface shown in Fig. 5.2(b). To model the principal step structures observed on miscut Si(111), four slab structures representing miscuts in the $\langle \bar{1}\,\bar{1}\,2 \rangle$ and $\langle 11\bar{2} \rangle$ directions with both two- and four-atom-wide terraces were constructed. As shown in Fig. 5.3, surfaces miscut toward the $\langle \bar{1}\,\bar{1}\,2 \rangle$ direction have strained, dihydride-terminated steps, and surfaces miscut toward the $\langle 11\bar{2} \rangle$ direction have unstrained, monohydride-terminated steps. Modeling two terrace widths for each step structure enabled comparison of strain and coupling effects.

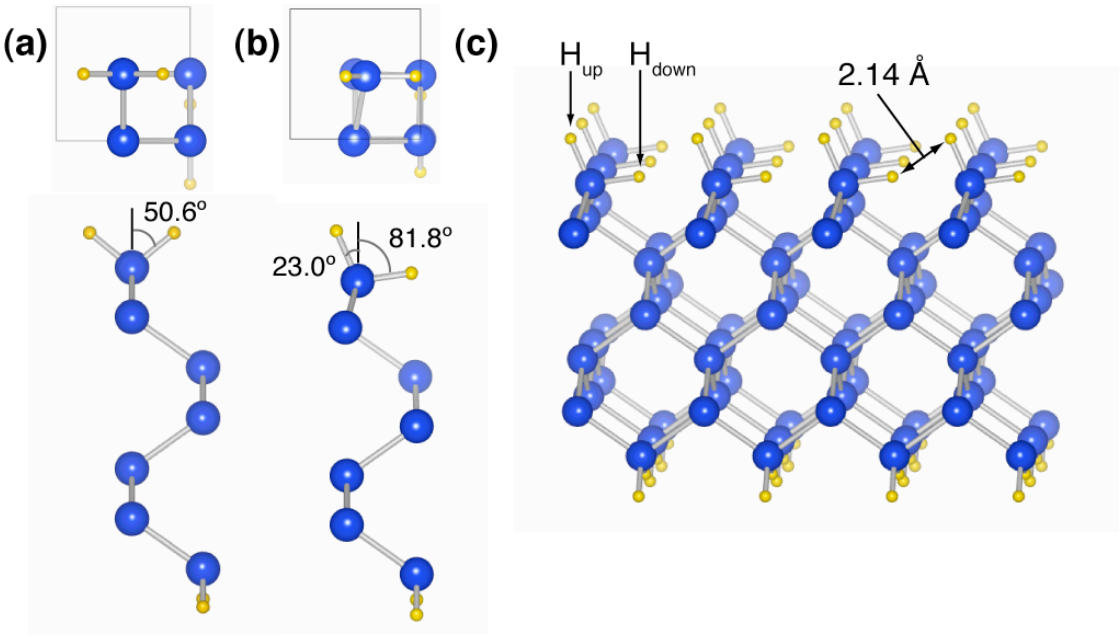

Figure 5.4. Structures used to predict the vibrational frequencies for flat H/Si(100). Representative H/Si(100) 1 × 1 unit cells relaxed with the top dihydride (a) constrained to a symmetric orientation and (b) allowed to cant. (c) A portion of the canted dihydride surface under periodic boundary conditions. The distance between adjacent hydrogens on neighboring dihydrides increased from 1.57 Å in (a) to 2.14 Å in (b). The relaxations were carried out with a $8 \times 8 \times 2$ *k*-point mesh and an energy cutoff of 850 eV.

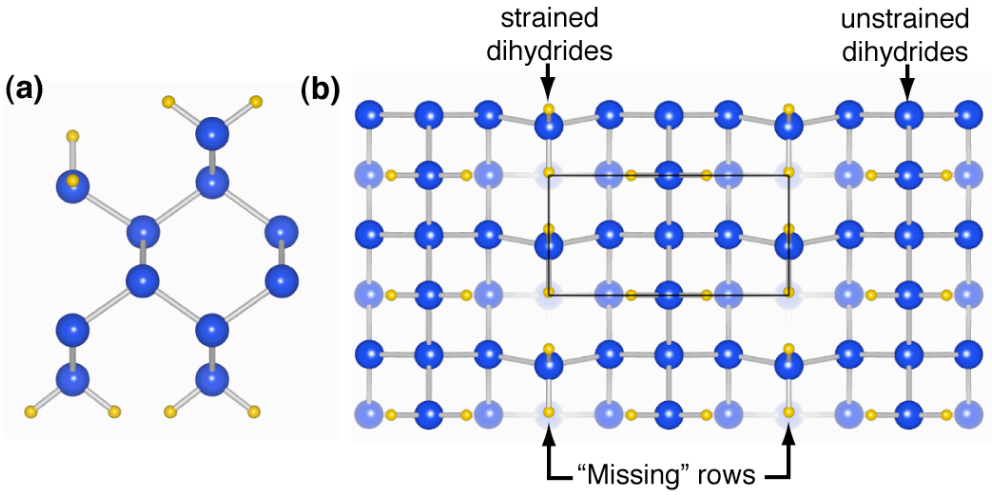

Figure 5.5. (a) A relaxed 2×1 unit cell and (b) periodic surface used to predict the vibrational frequencies of the "missing-row" surface observed in $NH_4F(aq)$-etched Si(100). In the simulated surface, infinitely long rows of unstrained dihydrides alternate with rows of strained, canted dihydrides. The outline of a unit cell has been added to (b). The bottom layer of silicon atoms was capped with symmetric dihydrides. The relaxation was carried out with a $4 \times 8 \times 2$ *k*-point mesh and an energy cutoff of 850 eV.

The relaxed, 1×1 bulk-terminated H/Si(100) surface was modeled using the unit cell shown in Fig. 5.4(a). The H atoms were sterically strained by interactions with neighboring dihydrides in the plane of the H–Si–H bonds. When symmetry constraints on the structure were removed, a canted dihydride structure was produced after relaxation, as shown in Fig. 5.4(b). Figure 5.4(c) shows a portion of the canted dihydride surface with periodic boundary conditions. The upward- and downward-pointing hydrogens are denoted H_{up} and H_{down}, respectively.

Recent experimental work has shown that Si(100) surfaces etched with 40% (*aq*) ammonium fluoride, although extremely flat, are not bulk terminated.[28] The 2×1 cell in Fig. 5.5(a) was used to model an idealized "missing-row" morphology similar to that observed on NH_4F-etched Si(100). This surface consists of rows of unstrained dihydrides separated by trenches terminated with strained dihydrides, as depicted in Fig. 5.5(b). To

study the effect of defects on this surface, a large 4×2 supercell of the canted dihydride morphology was constructed with eight surface dihydrides, as shown in Fig. 5.6(a). The three defect structures in Fig. 5.6(b-d) were then constructed by removing consecutive dihydrides from one of the canted dihydride rows.

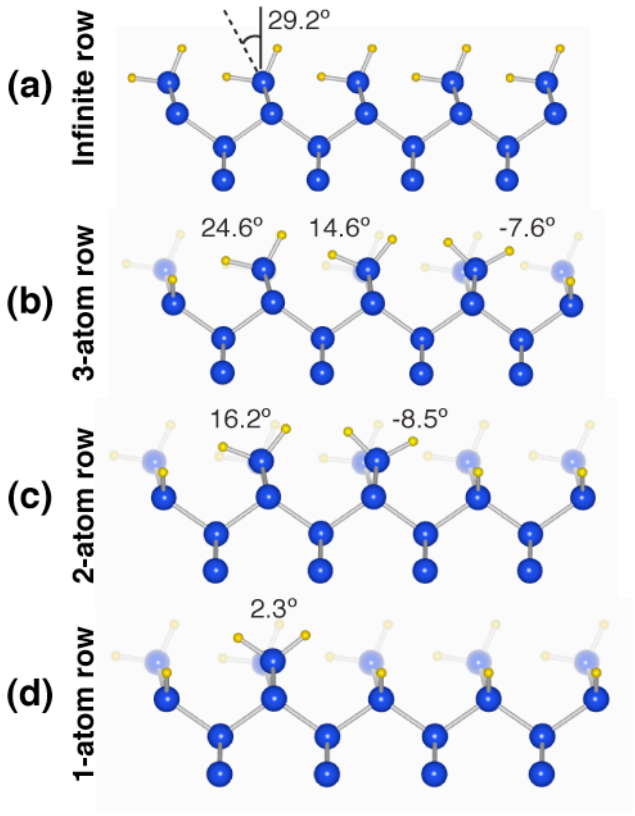

Figure 5.6 Relaxed 4×2 H/Si(100) unit cells used to calculate vibrational frequencies for rows of strained canted dihydrides with varying lengths. Dihydrides were removed sequentially from the row of four canted dihydrides (infinitely long with periodic boundary conditions) and allowed to relax. The angle between the dihydride H-Si-H bisector and surface normal is labeled. The bottom two layers of silicon atoms and terminal hydrogens are not shown, and a 5×2 portion of the surface is displayed for clarity. The relaxations were carried out with a $2 \times 3 \times 2$ *k*-point mesh and an energy cutoff of 850 eV.

All structures were optimized by relaxing the positions of all hydrogen atoms and the top four layers of silicon atoms. Silicon atoms in the bottom two layers of each

structure were frozen in their bulk positions. The Si lattice constant used for the frozen atoms, a_{Si} = 5.468 Å, was obtained from a bulk Si cell relaxed with the PBE functional. This lattice constant compares well to that obtained from all-electron calculations using the same PBE functional (a_{Si} = 5.472 Å).[29] The slabs were separated by at least 6 Å of vacuum. To reduce the electronic effects of dangling bonds, the bottom Si layer was passivated with hydrogen (*i.e.*, in the bulk-terminated geometry). For the relaxation, the one-electron orbitals were expanded using a plane-wave basis set with an energy cutoff of 750 - 850 eV and a dense Monkhorst-Pack *k*-point grid[30] to ensure convergence of the lattice parameter to less than 0.01 Å. The energy cutoff and *k*-point meshes used for each structure are noted in the captions of Figs. 5.2-5.6. Brillouin-zone integration was performed using the tetrahedron method with Blöchl corrections.

In most cases, the vibrational energies of the optimized structures were calculated using the tetrahedron method for the Brillouin-zone integration. This method fails on very large systems due to the small number of *k*-points in the irreducible Brillouin zone. For large systems [*e. g.,* the 4×2 H/Si(100) structures in Fig. 5.5], Gaussian smearing with a $\sigma \leq 0.1$ eV was used. A comparison of the two methods on small systems showed no significant differences in the calculated energies. The Hessian matrix of interatomic force constants was determined by DFPT, and then the mass-weighted Hessian matrix was diagonalized, yielding the Γ–point vibrational energies and normal modes. Normal-mode energies are reported as calculated; no scaling factor was used.

Because these calculations were performed at 0 K, low-temperature spectroscopic data are given for comparison whenever available. Temperature-dependent shifts in SiH_X vibrational modes are on the order of a few wavenumbers. For example, the Si-H stretch mode on flat H/Si(111) blueshifts by 2.3 cm^{-1} after cooling from room temperature to 14 K.[31]

Table 5.1. Comparison of silane vibrational modes obtained with the LDA, PBE, and PBEsol exchange-correlation functionals and two different versions of the PAW potentials, a soft one and a hard one denoted by "h". The structure was a $(15\ \text{Å})^3$ cell containing a single molecule of silane, relaxed with an energy cutoff of 700 eV and a $1 \times 1 \times 1$ k-point mesh. Vibrational mode energies were calculated with an energy cutoff of 500 eV, except for PBE hard and PBE sol, where 700 eV was used. The sum of the absolute errors for the calculated modes are listed in the bottom row.

Mode	**LDA** (cm^{-1})	**LDA h** (cm^{-1})	**PBE** (cm^{-1})	**PBE h** (cm^{-1})	**PBE sol** (cm^{-1})	**Expt.**[32] (cm^{-1})
ν_1 (sym stretch)	2176.9	2183.7	2177.6	2176.3	2168.4	2185.7
ν_2 (sym scissor)	933.4	931.9	946.7	950.8	932.1	972.1
ν_3 (asym stretch)	2190.8	2198.3	2191.8	2190.6	2181.5	2189.1
ν_4 (asym scissor)	854.6	850.0	877.6	877.4	876.2	913.3
Absolute Error	107.9	114.7	71.9	68.1	102.0	-

5.1.1. Convergence and accuracy tests

Some of the simulations required large unit cells and thus significant computational resources. To balance the competing demands of high accuracy and reasonable cost, the parameters for the simulations were optimized using the following tests.

The effects of the exchange-correlation functional on vibrational energies were tested on a cubic array of silane molecules separated by 15 Å of vacuum. Silane has four Si–H bonds analogous to those on H/Si surfaces, and its vibrational modes have been measured experimentally.[32] Several exchange-correlation functionals were tested, including the local-density approximation (LDA),[33] and two generalized-gradient approximations, PBE[27] and PBEsol.[34] For the LDA and PBE functionals, a hard and soft version of the PAW potentials were tested. Table 5.1 shows that the PBE functional most accurately reproduced the experimental measurements for silane, with approximately 35% less total absolute error than the LDA functional. The hard version of the PAW potential yielded a modest improvement (~5%) over the soft version. Later calculations on H/Si

confirmed the general observation that the PBE functional yielded better agreement with experiment than the LDA-calculated energies, which often matched poorly with experiment and occasionally reversed the order of vibrational modes (*e. g.,* the energy of symmetric and antisymmetric stretch modes).

The number of silicon layers in the slabs was also varied. Ideally, enough layers must be used to simulate the bulk electronic environment and to allow surface lattice distortions to smoothly transition to the bulk geometry. For that reason, all simulations incorporated four silicon layers that were free to relax, with either two or three underlying "frozen" (bulk-like) layers. For unstrained systems such as the H/Si(111) surface, the calculated stretching and bending energies converged to within ~1 cm^{-1} with only two free Si layers and four frozen layers, as described in Section 5.2.1. Allowing the relaxation of more layers did not significantly change the energies. In contrast, strain between surface adsorbates on Si(100) caused noticeable lattice distortion up to three silicon atoms deep.

Proper structural relaxation was critical to the precision of energy calculations. Convergence tests with respect to energy cutoff and *k*-point mesh were performed on each structure. For example, convergence tests on the 2×1 Si(100) structure with 11 Si atoms and 8 H atoms in a 7.73 Å × 3.86 Å × 20.47 Å cell showed all Si-H energies to be converged to within 5 cm^{-1} for energy cutoffs ≥ 650 eV and *k*-point meshes ≥ $3 \times 6 \times 1$, and to within 2.5 cm^{-1} for a *k*-point mesh of $5 \times 10 \times 1$ at the same energy cutoff. For the largest supercell, computational limits mandated a slightly less dense *k*-point mesh. In spite of this constraint, the stretching mode energies were converged to within 10 cm^{-1}. For a typical system, energy cutoffs ≥ 750 eV coupled with a sufficiently fine *k*-point mesh yielded stretching mode energies converged to within 3 cm^{-1}.

5.2. Results

The relaxed structures and vibrational energies were calculated for several H-terminated silicon surfaces, including flat and stepped H/Si(111), flat and structured H/Si(100), and a structured H/Si(100) surface with defects.

5.2.1. Flat H/Si(111) surface

Atomically-flat terraces of hydrogen-terminated Si(111) are produced by several alkaline aqueous etchants.[3,35,36] These surfaces have an ideal 1×1, unreconstructed, bulk-terminated structure in which each surface silicon is bound to a single hydrogen atom. These silicon monohydrides extend vertically from the surface and are separated by ~3.8 Å from one another. Because the van der Waals diameter of H is 2.40 Å, there is little steric strain between neighboring adsorbates. Two narrow Si–H vibrational modes are observed for this system: a stretching mode with a transition dipole normal to the surface, and a bending mode in the plane of the surface.[3,37,38]

Table 5.2. Comparison of H/Si(111) vibrational modes obtained with slabs of differing thickness. The number of layers frozen to their relaxed bulk positions was varied to determine the contribution of underlying layers to the vibrational modes. The vibrational mode energies were calculated using the PBE functional, a *k*-point mesh of $5 \times 5 \times 2$ and an energy cutoff of 700 eV.

Total Layers	**Frozen Layers**	**Stretch** (cm^{-1})	**Bend** (cm^{-1})
8	4	2107.45	614.47
6	2	2107.65	615.20
6	4	2107.80	613.59
4	2	2111.39	615.37

Because of the simple geometry and lack of strain-induced distortions on flat H/Si(111), this surface was used to determine the minimum cell structure parameters required for vibrational calculations with H/Si slabs. First, the effect of the total number of silicon layers as well as the number of frozen layers in the 1×1 H/Si(111) cell was

studied. The results are summarized in Table 5.2. The energies for the relaxed structures were converged to < 3 cm^{-1} when four total silicon layers were used, but convergence to < 1 cm^{-1} was achieved only after increasing the total number of layers to six. As expected, the vibrational energies were affected more by the number of relaxed layers than the number of frozen layers. For example, Table 5.2 shows that the stretching mode redshifted by 0.35 cm^{-1} when two additional relaxed layers were added to a 6-layer simulation, but redshifted by only 0.20 cm^{-1} when two frozen layers were added.

Table 5.3. Comparison of H/Si(111) vibrational modes obtained with the PBE functional for different supercells, each containing six layers of silicon capped with hydrogen. The bottom two layers of silicon were frozen to their relaxed bulk positions. The mode energies were calculated with $5 \times 5 \times 2$, $3 \times 6 \times 2$, and $3 \times 3 \times 2$ *k*-point meshes for the 1×1, 2×1, and 2×2 structures, respectively, and an energy cutoff of 800 eV. The experimental stretching and bending mode energies were measured at 14 K and 295 K, respectively.

Mode	**1×1** (cm^{-1})	**2×1** (cm^{-1})	**2×2** (cm^{-1})	**Expt.** (cm^{-1})
Terrace monohydride stretch	2109.38	2109.39	2109.43	2086.0[31]
Terrace monohydride bend	612.14	614.65	614.79	626.7[39]

To assess the numerical stability of the model, vibrational energies were calculated for the 1×1, 2×1 and 2×2 H/Si(111) supercells having 1, 2, and 4 monohydrides per cell, respectively. The calculated energies listed in Table 5.3 varied by 0.05 cm^{-1} for the stretching mode and ~2 cm^{-1} for the bending mode, exhibiting good stability towards cell size. The relaxed structure had a Si-H bond length of 1.50 Å and an interhydrogen distance of 3.87 Å (set by the "frozen" Si-Si distance), as indicated in Fig. 5.2. Table 5.3 shows that calculations on the 1×1 cell overestimated the Si–H stretching mode energy by 26 cm^{-1} and underestimated the Si-H bend energy by 15 cm^{-1} compared to experiment.[39] This accuracy is comparable to that of Ferguson *et al.*, who used the BLYP

functional with the 6-31G(*d, p*) basis set to compute unadjusted energies for H/Si(111) of 2123 cm^{-1} and 628 cm^{-1}.[11] (Ferguson *et al.* attributed the close agreement of their calculated bending mode energy with experiment to fortuitous cancellation of errors.)[40]

5.2.2. Stepped H/Si(111) surface

The key test for surface vibrational calculations is the accuracy of calculations on structures with significant interadsorbate strain. For these systems, structural relaxations are critical, requiring larger basis sets and finer *k*-point meshes than unstrained surfaces. Because the structure and vibrational modes of stepped Si(111) have been conclusively determined, these surfaces are a good benchmark for vibrational calculations. Two principal step structures can be created by miscutting Si(111) toward either the $\langle 11\bar{2} \rangle$ or $\langle \bar{1}\,\bar{1}\,2 \rangle$ directions. Surfaces miscut toward $\langle 11\bar{2} \rangle$ have steps decorated with a chain of monohydrides analogous to a one-layer-wide {110} facet, whereas Si(111) miscut toward $\langle \bar{1}\,\bar{1}\,2 \rangle$ has steps terminated with dihydrides, analogous to a one-layer-wide {100} facet.[6]

Table 5.4. Calculated vibrational modes of H/Si(111) miscut in the $\langle 11\bar{2} \rangle$ direction. The mode energies for the two- and four-atom wide terraces were calculated with $2 \times 4 \times 1$ and $1 \times 4 \times 1$ *k*-points, respectively, and an energy cutoff of 750 eV. The calculated terrace monohydride bend, A_2, had two approximately degenerate modes equivalent to orthogonal bending motions in the plane of the surface. Band designations were taken from Chabal *et al.*[6] The experimental stretching mode energies were measured at 90 K, whereas all other modes were measured at 295 K.

Band	**Mode**	**2 SiH terrace** (cm^{-1})	**4 SiH terrace** (cm^{-1})	**Experiment** (cm^{-1})
B_2	Step sym- stretch	2114.7	2113.3	2089.1[6]
A_1	Terrace monohydride stretch	2105.2	2107.2	2085.6[6]
B_1	Step antisym- stretch	2100.0	2101.9	2072.7[6]
B_3	Step out-of-plane wag	640.9	641.4	649, 637[7]
A_2	Terrace monohydride bend	611.8, 617.9	609.1, 615.6	627[39]
B_4	Step in-plane wag	601.4	595.2	614[39]

The relaxed structures for Si(111) surfaces miscut toward the $\langle 11\bar{2}\rangle$ direction are shown in Fig. 5.3(a,b). Because the monohydride step species were unstrained, no significant distortions from the bulk-terminated positions occurred. The vibrational energies calculated for the $\langle 11\bar{2}\rangle$-miscut H/Si(111) surface are shown in Table 5.4. (The band designations defined by Jakob and Chabal[6] are used throughout.) The calculated mode order agreed with experiment; however, the stretching mode energies were overestimated by approximately 25 cm^{-1}, whereas the wagging and bending modes were underestimated by 10-20 cm^{-1}.

Table 5.5. Calculated vibrational modes of H/Si(111) miscut in the $\langle \bar{1}\,\bar{1}\,2\rangle$ direction. The mode energies for the two- and four-atom wide terraces were calculated with $2\times4\times1$ and $1\times4\times1$ *k*-point meshes, respectively, and an energy cutoff of 750 eV and 700 eV, respectively. The experimental stretching mode energies were measured at 90 K, whereas all other modes were measured at 295 K.

Band	**Mode**	**2 SiH terrace** (cm^{-1})	**4 SiH terrace** (cm^{-1})	**Experiment** (cm^{-1})
C_3	Strained dihydride stretch	2152.5	2150.9	2135.7[6]
C_1	Terrace-like dihydride stretch	2126.3	2127.6	2095.6[6]
C_2	Strained monohydride stretch	2122.4	2122.4	2102.5[6]
A_1	Terrace monohydride stretch	2105.1	2108.9	2085.6[6]
C_4	Dihydride scissor	892.4	892.0	913[7]
C_5	Dihydride wag	636.7	635.1	656[39]
A_2	Terrace monohydride bend	614.4, 621.8	614.7, 616.3	627[39]

In contrast to the $\langle 11\bar{2}\rangle$-miscut H/Si(111) surface, Si(111) miscut toward $\langle \bar{1}\,\bar{1}\,2\rangle$ has strained dihydride step species, as illustrated by the relaxed structures in Fig. 5.3(c, d). This surface has been studied experimentally with infrared[7,38,41,42] and Raman[43,44] spectroscopies, and the mode assignments and orientations are well known. After relaxation, the step dihydride in Fig. 5.3(c) tilted upwards from its bulk-terminated

position by 18.9º, which was substantially larger than the 4º predicted by Li *et al.*[45] but comparable to the 20º calculated by Raghavachari *et al.*[8] Table 5.5 lists the calculated vibrational modes for the $\langle \bar{1}\,\bar{1}\,2 \rangle$-miscut Si(111) surface. In general, the stretching energies were overestimated by 15-30 cm^{-1}, and the lower energy modes were underestimated by a similar amount. The 28.5 cm^{-1} calculated splitting between the C_3-C_2 modes (for the 4 SiH terrace structure) was in good agreement with the 33.2 cm^{-1} observed in experiment, but the simulated energies for the closely-spaced C_1 and C_2 modes were reversed. Analysis by Hines *et al.* showed the polarized, angle-dependent Raman spectra of the C_1, C_2, and C_3 modes were consistent with localized vibrations of H_C, H_A, and H_B, respectively.[44] In contrast, the calculation of Raghavachari *et al.* found that the C_2 and C_3 modes roughly correspond to out-of-phase and in-phase vibrations of H_A and H_B.[8] The modes predicted by the DFT simulation all showed significant coupling, with only 60%, 66%, and 72% of the C_1, C_2, and C_3 mode energy being localized on H_C, H_A, and H_B, respectively.

In addition, Jakob *et al.* measured the energy of the terrace stretch vibration as a function of terrace width on $\langle \bar{1}\,\bar{1}\,2 \rangle$-miscut Si(111).[46] Compared to the calculated stretching mode of the infinite Si(111) terrace in Table 5.3, the predicted A_1 mode energies in Table 5.5 were redshifted by 2.2 cm^{-1} and 4.2 cm^{-1} for terraces with one unstrained terrace monohydride and three unstrained terrace monohydrides, respectively. These calculated shifts were in good agreement with the 2.20 cm^{-1} and 4.59 cm^{-1} shifts observed by Jakob *et al.* for terraces of the same size.

In general, the calculations were more accurate for unstrained species than for strained species. For instance, the calculated mode order for the *B* stretches (unstrained step monohydride) agreed with experiment, whereas the calculated *C* modes (strained step dihydride) did not. In addition, the calculated coupling in the *C* modes was also significantly different than indicated by experiment. The difficulty of calculating accurate

vibrational energies for strained species on H/Si(111) surfaces hints at the sensitivity of vibrational modes to the local strain environment.

5.2.3. Flat H/Si(100) surface

Because the ideally flat H/Si(100) surface has never been experimentally observed, no objective basis for evaluating the accuracy of the many theoretical predictions exists. Nevertheless, the flat H/Si(100) surface represents the simplest H/Si(100) morphology and is a well-studied test system.

The flat H/Si(100) surface was modeled with a 1×1 cell. The initially symmetric-dihydride-terminated surface (SDS) in Fig. 5.4(a) relaxed to a canted dihydride surface (CDS) in Fig. 5.4(b). The canted dihydride Si-Si bond was tilted by 15.0º with respect to the surface normal, and the bisector of the H-Si-H dihydride bonds was tilted by 29.4º. The Si–H bond lengths for the "up" and "down" CDS hydrogens were 1.494 Å and 1.500 Å, respectively, and the H–Si–H bond angle was 104.9º (an ideal tetrahedral angle would be 109.5º). Canting increased the interhydrogen distance from 1.57 Å to 2.14 Å, as illustrated in Fig. 5.4(c). These structural parameters are in good agreement with the results of previous researchers.[47] The energy per 1×1 cell of the CDS was calculated to be 0.14 eV lower than that of the SDS, which was somewhat less than the values previously calculated (0.19-0.20 eV).[18]

The 1×1 CDS had six SiH_2 vibrational modes: two stretching modes, a scissor (D_{sr}^{c}), wagging (D_{w}^{c}), twisting, and rocking mode. Unlike the SDS, which had symmetric and antisymmetric dihydride stretching modes, the nonequivalent CDS hydrogens stretched independently of one another along their respective bond directions. These modes are denoted D_{up}^{c}, named for the stretch of the "up" hydrogen of the canted dihydride, and D_{dn}^{c}, named for the "down" hydrogen. Although most simulations generally agreed on the structural parameters of the CDS (to within a few percent), vibrational energy calculations have been wildly discordant, as shown in Fig. 5.1. For

example, the predicted stretching mode splittings (D^c_{up} - D^c_{dn}) range from -193.6 cm^{-1} [16] to 121.0 cm^{-1},[18] with the negative value indicating reversed mode order.

Table 5.6. Calculated vibrational modes of the flat 1×1 H/Si(100) bulk-terminated surface consisting of strained canted dihydrides, obtained with a $8 \times 8 \times 2$ *k*-point mesh and an energy cutoff of 750 eV. Prior results from similar DFT calculations are shown for comparison.

Band	**Mode**	**This Work** (cm^{-1})	**Ref. 18** (cm^{-1})	**Ref. 19** (cm^{-1})
D^c_{up}	"Up" stretch	2155.0	2089.0	2201.9
D^c_{dn}	"Down" stretch	2099.2	1992.2	2137.4
D^c_{sr}	Scissor	887.2	822.7	-
D^c_{w}	Wag	633.5	613.0	-
	Up - Down Split	55.8	96.8	64.5

Table 5.6 lists the predicted energies for the four highest energy vibrational modes and compares these energies to two similar DFT studies. Although the predicted stretching mode energies vary widely, all three studies predict the same mode order and a D^c_{up} - D^c_{dn} splitting greater than 50 cm^{-1}. The computed stretching mode splitting of 55.8 cm^{-1} was moderately lower than in comparable work.

5.2.4. H/Si(100) "missing-row" structure

Testing the accuracy of vibrational energy calculations for H/Si(100) requires a well-characterized surface morphology with an assigned infrared spectrum. The NH_4F(*aq*)-etched Si(100) surface, described in Chapter 3, has a near-atomically-flat surface with a well-defined "missing-row" structure (MRS) consisting of rows of unstrained symmetric dihydrides alternating with valleys of strained canted dihydrides. Likewise, the infrared absorbance spectrum of the surface consists of only five, albeit

broad, modes with distinct polarizations.[28] This surface morphology is therefore an ideal test case for vibrational energy calculations on highly strained surfaces.

Figure 5.5(a) shows the 2×1 unit cell constructed with one unstrained dihydride and one canted dihydride to simulate the MRS of NH_4F-etched Si(100). With periodic boundary conditions, the relaxed 2×1 cell produced infinite rows of unstrained dihydrides separated by rows of strained, canted dihydrides equivalent to a defect-free terrace of the MRS, as illustrated in Fig. 5.5(b).

Table 5.7. Calculated vibrational modes of the 2×1 Si(100) "missing row" morphology obtained with a $3 \times 6 \times 1$ *k*-point mesh and 750 eV cutoff energy. Experimental mode energies are from room temperature measurements. The calculated mode energies for flat H/Si(100), as listed above in Table 5.6, are reproduced for comparison in the last column.

Band	**Mode**	**Predicted** (cm^{-1})	**Experiment** (cm^{-1})	**Flat H/Si(100)** (cm^{-1})
D^{c}_{up}	Canted dihydride "up" stretch	2142.9	2142.6[28]	2155.0
D^{u}_{as}	Unstrained dihydride antisym. stretch	2138.4	2111.7[28]	-
D^{u}_{ss}	Unstrained dihydride sym. stretch	2126.9	2104.0[28]	-
D^{c}_{dn}	Canted dihydride "down" stretch	2076.7	2083.7[28]	2099.2
D^{u}_{sr}	Unstrained dihydride scissor	892.2	918.0[Ch.3]	-
D^{c}_{sr}	Canted dihydride scissor	873.4	906.0 [Ch.3]	887.2
D^{c}_{w}	Canted dihydride wag	646.6	659.6 [Ch.3]	633.5
D^{u}_{w}	Unstrained dihydride wag	635.3	655.7 [Ch.3]	-

Table 5.7 shows the calculated and experimentally observed vibrational energies for the MRS. Qualitatively, the predicted vibrational modes had the same overall order as in the experimental spectrum. Quantitatively, the nearly perfect match between the predicted and actual canted dihydride-stretching mode energies, D^{c}_{up} and D^{c}_{dn}, was

surprising. The calculated mode splitting ($D^{c}_{up} - D^{c}_{dn}$) of 66.2 cm^{-1} was also in good agreement with the 58.9 cm^{-1} observed splitting, supporting the assignment of the H/Si(100) absorbance spectrum in Chapter 3.

The structural similarities between the MRS and the CDS provided additional insight. In going from a linear array of canted dihydrides in the MRS to two-dimensional arrays in the CDS, the calculated energies blueshifted by 12 cm^{-1} and 22 cm^{-1} for the D^{c}_{up} and D^{c}_{dn} modes, respectively. These energy increases are consistent with the increased (approximately doubled) interadsorbate strain on the CDS.

The accuracy of the calculated energies for the other modes in Table 5.7 was comparable to that of unstrained species on Si(111). For example, the calculated stretch energies for unstrained dihydrides, D^{u}_{as} and D^{u}_{ss}, were overestimated by ~25 cm^{-1}, and the calculated wagging mode energies were 10-20 cm^{-1} lower than in experiment. The calculated mode splittings were also moderately overestimated. For instance, the splitting between the unstrained dihydride stretching modes ($D^{u}_{as} - D^{u}_{ss}$) was calculated to be 11.5 cm^{-1}, compared to ~8 cm^{-1} in experiment. Likewise, the energy splittings between unstrained and canted dihydride modes were also too large, yielding 18.8 cm^{-1} and 11.3 cm^{-1} for the scissor and wagging modes, respectively, versus 12.0 cm^{-1} and 4.9 cm^{-1} in experiment. In light of the moderate error for the majority of the calculated mode energies, the highly accurate energies obtained for the canted dihydride stretching modes was likely fortuitous.

5.2.5. H/Si(100) surface with defects

As shown in the previous two sections, strong interadsorbate interactions between neighboring dihydrides led to spontaneous canting and large shifts in vibrational mode energies; however, perfect, defect-free surfaces may be a poor model of experiment. As shown by the scanning tunneling microscopy (STM) images in Chapter 3, dihydride rows on NH_4F(*aq*)-etched Si(100) have finite length, typically extending for tens

of atoms or less. With defects caused by the abstraction of silicon atoms, dihydrides near the defect would be able to relieve some of the severe interadsorbate strain by distorting from the perfectly canted geometry shown in Fig. 5.5(b). Partial relaxation of strain would shift the vibrational mode energies, because the vibrational modes of strained and unstrained dihydrides are very different. What are the vibrational modes of *finite* rows of strained dihydrides? Does strain relaxation lead to significant energy shifts?

To examine these effects, a 4×2 CDS supercell was constructed as shown in Fig. 5.6(a). Beginning from this ideally flat surface, dihydrides were sequentially removed from one row of canted dihydrides, leading to the three relaxed, defective surfaces shown in Fig. 5.6(b-d). A pair of opposing monohydrides filled the gap left by each abstracted dihydride. The relaxations in Fig. 5.6(b-d) were not symmetric about the midpoint of the shortened row because of lattice distortions induced by the adjacent row of canted dihydrides. For example, the two leftmost dihydrides in Fig. 5.6(b) canted by 24.6º and 14.6º, whereas the rightmost hydrogen tilted by 7.6º in the opposite direction. A similar asymmetry is observed in Fig. 5.6(c) in which the left dihydride canted by 16.2º and the right dihydride by -8.5º.

The vibrational mode energies for the structures in Fig. 5.6 were also calculated. Because of the reduced symmetry of the defect structures, most of the modes are expected to be infrared active, although some may have relatively small transition dipole moments. Calculations of the relative absorbances of these transitions are under way. In the absence of these calculations, the two most intense modes are expected to be the in-phase stretch vibrations of the "up" and "down" hydrogens—the highest and lowest energy modes, respectively. The calculated energies of these extreme modes are listed in Table 5.8. The mode splittings in Table 5.8 decreased monotonically from 64.9 cm^{-1} to 13.6 cm^{-1} as the canted dihydride row length was shortened from infinitely long to a single unit. As expected, the vibrational energies of the isolated dihydride in Fig. 5.6(d)

were similar to D_{as}^{u} and D_{ss}^{u} of the MRS. Tagami and Tsukada have also calculated the vibrational mode energies for canted dihydride rows of varying lengths with the empirical tight-binding method.[16] Their models used dihydride rows that were truncated by a single silicon dimer (instead of opposing monohydrides), and the cell size was simply increased to obtain longer row lengths. Tagami and Tsukada calculated a mode splitting that increased monotonically from ~32 cm^{-1} for an isolated dihydride to ~226 cm^{-1} for a row of six dihydrides, but decreased to ~202 cm^{-1} for an infinitely long row. Although the trend of increasing mode splitting for longer rows agrees with the calculations reported here, the splittings calculated by Tagami and Tsukada are much larger than the values in Table 5.8. Furthermore, the 32 cm^{-1} splitting calculated for an isolated dihydride is four times as large as in experiment (~8 cm^{-1}).[28]

Table 5.8. Highest and lowest stretching mode energies calculated for rows of strained canted dihydrides in the 4×2 Si(100) unit cells shown in Fig. 5.6. As the canted dihydride row length was shortened, the mode energies show large shifts and a gradually decreasing splitting. The vibrational calculations were performed with a $1 \times 2 \times 1$ *k*-point mesh and an energy cutoff of 750 eV.

Row Length	**In-phase "up" mode** (cm^{-1})	**In-phase "dn" mode** (cm^{-1})	**Splitting** (cm^{-1})
Infinite row	2165.1	2100.2	64.9
Three dihydrides	2175.3	2137.6	37.7
Two dihydrides	2162.6	2130.5	31.3
One dihydride	2143.4	2129.8	13.6

The pairs of highly strained opposing monohydrides in Fig. 5.6(b-d) were predicted to have symmetric and antisymmetric vibrations between 2170 cm^{-1} and 2185 cm^{-1}, with the highest energy mode for all structures being a coupled symmetric

stretch at 2185 cm^{-1} ± 2 cm^{-1}. These modes were consistently 5-20 cm^{-1} higher than the highest energy mode of the canted dihydrides.

5.3. Discussion

The larger mode splittings calculated for strained species compared to unstrained species on the H/Si(100) MRS agreed with experimental assignments, confirming the significant effect of interadsorbate strain on vibrational mode energies. As discussed below, variations in interadsorbate strain can explain mode broadening observed in experiment; in general, however, the calculated vibrational mode energies of highly strained surfaces displayed significant errors.

5.3.1. The effect of strain on H/Si(100) vibrational mode broadening

The infrared spectrum of NH_4F-etched Si(100) spectra has very broad absorbance modes compared to other wet-chemically etched surfaces. For example, the spectrum in Fig. 3.10(b) shows that the canted dihydride D^c_{dn} mode at 2083.7 cm^{-1} is ~20 cm^{-1} wide at half its maximum intensity, and the D^c_{up} transition at 2142.6 cm^{-1} is ~15 cm^{-1} wide. In contrast, the symmetric and antisymmetric stretching modes for relaxed canted dihydrides at 2092.4 cm^{-1} and 2109.8 cm^{-1}, respectively, on H_2O-etched Si(100) have widths < 4 cm^{-1}.[48] For comparison, the terrace monohydride stretching mode on flat Si(111) has a much narrower linewidth than both of these surfaces—only 0.9 cm^{-1} at room temperature.[49] The band broadness of NH_4F(*aq*)-etched Si(100) was attributed by previous researchers to a heterogeneous mixture of species on atomically rough surfaces;[50] however, the etched surface is now known to be near-atomically flat with a well-defined morphology.[28] If the band broadening is not caused by atomic-scale roughness, what produces the broad absorbance modes?

The broad stretching modes of NH_4F-etched Si(100) spectra can be explained by local variations in interadsorbate strain. The defect structures shown in Fig. 5.6(b) and (c) have finite rows of canted dihydrides with individual dihydrides that are tilted at a variety

of angles. These "semi-canted" dihydrides had calculated vibrational mode energies that were significantly different from mode energies for canted dihydrides in an infinite row. For example, the calculated energy for the lowest energy stretching vibration (*i.e.,* the in-phase "down" mode) varied by ~37 cm^{-1} going from an infinitely long row of canted dihydrides to a row with only two dihydrides, and the highest energy stretching vibration (*i.e.,* the in-phase "up" mode) varied by ~13 cm^{-1}. These row-length-dependent shifts are comparable to the linewidths of the canted dihydride stretching modes on $NH_4F(aq)$-etched Si(100). Variations in the local strain environment may also explain the relatively broad linewidths (~10 cm^{-1}) of the unstrained dihydride stretching modes, D_{as}^{u} and D_{ss}^{u}, on $NH_4F(aq)$-etched Si(100). For instance, the isolated dihydride in Fig. 5.6(d) was distorted from a symmetric geometry because of the adjacent row of strained dihydrides. Consequently, the calculated stretching mode energies (2129.8 cm^{-1} and 2143.4 cm^{-1}) for this isolated dihydride were shifted by 3-4 cm^{-1} from the unstrained dihydride mode energies calculated for the defect-free MRS (2126.9 cm^{-1} and 2138.4 cm^{-1}). Although $NH_4F(aq)$-etched Si(100) is near-atomically smooth, local variations in interadsorbate strain due to defects cause near-surface lattice distortions that may lead to heterogeneous mode broadening for both strained and unstrained species.

Because of the small cell size used to model defect structures, caution must be used when drawing conclusions from the calculated energies in Table 5.8. For example, the canted dihydride row lengths for the structures in Fig. 5.6(b) and (c)—three and two dihydrides, respectively—were significantly shorter than the vast majority of rows observed on $NH_4F(aq)$-etched Si(100). Ideally, structures with much longer row lengths (*i.e.,* 10-20 dihydrides) would have been modeled for comparison; however, cells of that size were computationally prohibitive. In addition, the defect structures in Fig. 5.6 were produced by abstracting silicon atoms from a flat CDS. Because the $NH_4F(aq)$-etched Si(100) morphology is closer (though not equivalent) to a "missing-row" structure, the

specific defect structures that were modeled may in fact be relatively rare on the etched surface.

5.3.2. Accuracy of calculated mode energies for H-terminated silicon

In general, the absolute mode energies calculated for H/Si surfaces had errors between one and two percent. Stretching mode energies were typically overestimated by 20-25 cm^{-1}, whereas wagging/bending modes were systematically underestimated by 10-20 cm^{-1}. For the miscut Si(111) surfaces, the calculated mode splitting between the *B* stretching modes (B_2-B_1) was underestimated by 10-30%, and the splittings between the *C* stretching modes (C_3-C_2 and C_1-C_2) were underestimated by 9-43%. In contrast, the calculated splittings between the unstrained dihydride stretching modes (D^{u}_{as} - D^{u}_{ss}) and canted dihydride stretching modes (D^{c}_{up} - D^{c}_{dn}) on the MRS were overestimated by 49% and 12%, respectively.

The relative mode energies calculated for strained adsorbates were generally less accurate than for unstrained adsorbates. For example, of the three coupled systems simulated [*i.e.* two miscut Si(111) geometries and the Si(100) MRS], the calculated mode order was incorrect for only one structure—Si(111) miscut toward the $\langle \bar{1}\,\bar{1}\,2 \rangle$, which has strained dihydride step species. The calculated order of the C_1 and C_2 mode energies were consistently reversed compared to experiment—a combined error of ~11-12 cm^{-1}. Although the calculated *order* of the Si(100) MRS stretching mode energies agreed with the mode order of NH_4F-etched Si(100), the relative mode *energies* were substantially different. For instance, the unstrained dihydride antisymmetric stretching mode, D^{u}_{as}, is 30.9 cm^{-1} lower than the canted dihydride "up" stretch, D^{c}_{up}, in experiment but was calculated to be only 4.5 cm^{-1} lower by simulation. In contrast, the calculated stretching modes for unstrained monohydrides on stepped Si(111)—the *B* modes—had the correct order and mode splittings that were roughly comparable to experiment.

In spite of the difficulty of calculating mode energies for strained adsorbates, the results obtained for flat H/Si(100) suggest that these simulations were more accurate than previous work. Although flat H/Si(100) has never been experimentally observed, some comparisons can be made between the calculated CDS mode energies and the experimental mode energies for linear rows of canted dihydrides observed on NH_4F(*aq*)-etched Si(100). As shown in Table 5.7, the agreement of the calculated CDS stretching mode order with experiment and the MRS simulations confirms that the D^{c}_{up} mode is higher in energy than the D^{c}_{dn} mode, in contradiction to Tagami *et al.*[15-17] Furthermore, the calculated CDS mode energies and splittings were comparable to the experimental values for canted dihydrides. This agreement stands in contrast to the predicted mode energies in Refs. 18-19, which varied significantly in one or both of these criteria, as shown in Fig. 5.1.

The neglect of anharmonicity, either in the Si–H bands or in coupling to substrate phonon modes, could not explain the ~10-25 cm^{-1} errors in the calculated mode energies. For example, the sum of anharmonic effects for the Si-H stretching mode on flat H/Si(111), estimated from absorbance spectra extrapolated to 0 K, is a net blueshift of only 3 cm^{-1}.[31] Similarly, the stretching-region of NH_4F(*aq*)-etched Si(100) blueshifted by ~3 cm^{-1} after being cooled to liquid-nitrogen temperatures, indicating that anharmonicity is a very small component of the mode energies.[Ch.3]

Instead, the computational methodology constituted the major source of error, in part because even small errors in the relaxed structure produce large errors in the calculated mode energies. Calculations on strained species underscored the importance of the functional. For instance, the large stretching mode splitting (96.8 cm^{-1}) for the CDS obtained by Freking *et al.*[18] may be a result of the LDA exchange-correlation functional used to optimize their structure. The method used in this work yielded a comparable CDS mode splitting of ~100 cm^{-1} after structural relaxation with the LDA functional

(regardless of the functional used for calculating vibrational modes), whereas relaxation with the PBE functional yielded a much different result (55.8 cm^{-1}). The PBE functional and the hard version of the PAW potential were ultimately chosen because this combination produced energies in best agreement with empirical data.

In summary, the vibrational mode energies calculated with DFT cannot yet determine the mode energies of H-terminated silicon to the accuracy necessary for predictive mode assignments. Nevertheless, DFT calculations are still useful for exploring the vibrational properties of complex H/Si surfaces. Calculations of relative trends (*e. g.,* terrace size effects, strain-induced energy shifts) and mode order can identify the structural origin of different vibrational modes and confirm experimental assignments. Predicting accurate vibrational mode energies for highly strained morphologies remains problematic.

5.4. Conclusions

The vibrational mode energies of several H-terminated silicon surfaces were calculated with DFT. Atomically-flat H/Si(111) was used to test the necessary parameters for accurate calculations. Mode energies for stepped H/Si(111) surfaces were also calculated, which yielded incorrect mode orders for some stretching modes of strained species. The calculated vibrational modes for the Si(100) MRS showed that strained dihydride species have large stretching mode splittings, confirming the vibrational mode assignments in Chapter 3 for NH_4F-etched Si(100). Adding defects to rows of canted dihydrides created local variations in the amount of interadsorbate strain. These variable strain-induced distortions caused significant vibrational mode shifts that were consistent with mode broadening observed in spectra of NH_4F(*aq*)-etched Si(100).

Vibrational mode energy calculations with DFT are not yet accurate enough for *a priori* determination of the vibrational spectrum for an arbitrary H/Si surface. Although relative properties (*e. g.,* mode order) were correctly calculated for unstrained structures,

the calculated vibrational mode energies for surfaces with significant interadsorbate strain had greater error in both the absolute and relative mode energies. In spite of these errors, vibrational mode calculations are a useful tool for confirming experimental mode assignments.

REFERENCES

[1] Y. J. Chabal and K. Raghavachari, Surface Science **502,** 41-50 (2002).

[2] W. Kern, in *Handbook of Silicon Wafer Cleaning Technology*, 2nd ed., edited by K. A. Reinhardt and W. Kern (William Andrew Inc., 2008), p. 3-92.

[3] G. S. Higashi, Y. J. Chabal, G. W. Trucks, and K. Raghavachari, Applied Physics Letters **56,** 656-658 (1990).

[4] K. Arima, J. Katoh, S. Horie, K. Endo, T. Ono, S. Sugawa, H. Akahori, A. Teramoto, and T. Ohmi, Journal of Applied Physics **98,** 103525-1 - 103525-8 (2005).

[5] Y. J. Chabal, G. S. Higashi, K. Raghavachari, and V. A. Burrows, Journal of Vacuum Science & Technology A: Vacuum, Surfaces, and Films **7,** 2104-2109 (1989).

[6] P. Jakob and Y. J. Chabal, Journal of Chemical Physics **95,** 2897-2909 (1991).

[7] S. Watanabe, Journal of Chemical Physics **108,** 5965-5974 (1998).

[8] K. Raghavachari, P. Jakob, and Y. J. Chabal, Chemical Physics Letters **206,** 156-160 (1993).

[9] M. K. Weldon, K. T. Queeney, A. B. Gurevich, B. B. Stefanov, Y. J. Chabal, and K. Raghavachari, Journal of Chemical Physics **113,** 2104-2109 (2000).

[10] M. D. Halls and K. Raghavachari, Journal of Physical Chemistry B **108,** 19388-19391 (2004).

[11] G. A. Ferguson, S. Rivillon, Y. Chabal, and K. Raghavachari, Journal of Physical Chemistry C **113,** 21713-21720 (2009).

[12] S. Ciraci, R. Butz, E. M. Oellig, and H. Wagner, Physical Review B **30,** 711-720 (1984).

[13] S. Ciraci and I. P. Batra, Surface Science **178,** 80-89 (1986).

[14] J. E. Northrup, Physical Review B **44,** 1419-1422 (1991).

[15] K. Tagami and M. Tsukada, Surface Science **384,** 308-314 (1997).

[16] K. Tagami and M. Tsukada, Journal of the Physical Society of Japan **68,** 3303-3306 (1999).

[17] K. Tagami, E. Tsuchida, and M. Tsukada, Surface Science **446,** L108-L112 (2000).

[18] U. Freking, P. Krüger, A. Mazur, and J. Pollmann, Physical Review B **69,** 035315-1 - 035315-11 (2004).

[19] J. Fritsch, private communication cited in Ref. 18 as Ref. 37.

[20] K. Raghavachari and M. D. Halls, Molecular Physics **102,** 381-393 (2004).

[21] M. D. Halls and K. Raghavachari, Journal of Physical Chemistry A **108,** 2982-2987 (2004).

[22] G. Kresse and J. Hafner, Physical Review B **48,** 13115-13118 (1993).

[23] G. Kresse and J. Furthmuller, Computational Materials Science **6,** 15-50 (1996).

[24] G. Kresse and J. Furthmuller, Physical Review B **54,** 11169-11186 (1996).

[25] P. E. Blochl, Physical Review B **50,** 17953-17979 (1994).

[26] G. Kresse and D. Joubert, Physical Review B **59,** 1758-1775 (1999).

[27] J. P. Perdew, K. Burke, and M. Ernzerhof, Physical Review Letters **77,** 3865-3868 (1996).

[28] I. T. Clark, B. S. Aldinger, A. Gupta, and M. A. Hines, Journal of Physical Chemistry C **114,** 423-428 (2010).

[29] R. G. Hennig, A. Wadehra, K. P. Driver, W. D. Parker, C. J. Umrigar, and J. W. Wilkins, Physical Review B **82,** 014101-1 - 014101-9 (2010).

[30] H. J. Monkhorst and J. D. Pack, Physical Review B **13,** 5188-5192 (1976).

[31] R. Honke, P. Jakob, Y. J. Chabal, A. Dvořák, S. Tausendpfund, W. Stigler, P. Pavone, A. P. Mayer, and U. Schroder, Physical Review B **59,** 10996-11013 (1999).

[32] H. W. Kattenberg and A. Oskam, Journal of Molecular Spectroscopy **49,** 52-69 (1974).

[33] D. M. Ceperley and B. J. Alder, Physical Review Letters **45,** 566-569 (1980).

[34] J. P. Perdew, A. Ruzsinszky, G. I. Csonka, O. A. Vydrov, G. E. Scuseria, L. A. Constantin, X. L. Zhou, and K. Burke, Physical Review Letters **100,** 136406-1 - 135406-4 (2008).

[35] P. Allongue, Physical Review Letters **77,** 1986-1989 (1996).

[36] S. P. Garcia, H. Bao, and M. A. Hines, Physical Review Letters **93,** 166102-1 - 166102-4 (2004).

[37] P. Dumas and Y. J. Chabal, Chemical Physics Letters **181,** 537-543 (1991).

[38] S. Watanabe and Y. Sugita, Chemical Physics Letters **244,** 105-110 (1995).

[39] Y. Caudano, P. A. Thiry, and Y. J. Chabal, Surface Science **502,** 91-95 (2002).

[40] G. A. Ferguson, K. Raghavachari, D. J. Michalak, and Y. J. Chabal, Journal of Physical Chemistry C **112,** 1034-1039 (2008).

[41] S. Watanabe, Surface Science **415,** 385-391 (1998).

[42] P. Jakob, Y. J. Chabal, K. Kuhnke, and S. B. Christman, Surface Science **302,** 49-56 (1994).

[43] M. A. Hines, Y. J. Chabal, T. D. Harris, and A. L. Harris, Physical Review Letters **71,** 2280-2283 (1993).

[44] M. A. Hines, Y. J. Chabal, T. D. Harris, and A. L. Harris, Journal of Chemical Physics **101,** 8055-8072 (1994).

[45] X. P. Li, D. Vanderbilt, and R. D. Kingsmith, Physical Review B **50,** 4637-4641 (1994).

[46] P. Jakob, Y. J. Chabal, K. Raghavachari, and S. B. Christman, Physical Review B **47,** 6839-6842 (1993).

[47] See Table II of Ref. 18.

[48] M. F. Faggin, S. K. Green, I. T. Clark, K. T. Queeney, and M. A. Hines, Journal of the American Chemical Society **128,** 11455-11462 (2006).

[49] P. Dumas, Y. J. Chabal, and G. S. Higashi, Physical Review Letters **65,** 1124-1127 (1990).

[50] P. Dumas, Y. J. Chabal, and P. Jakob, Surface Science **269/270,** 867-878 (1992).

Chapter 6

The Effects of *p*H on the Steady-state Morphology of Si(100) Surfaces Etched in Buffered HF

Because of the crucial need for clean silicon surfaces in microelectronic device manufacturing, harsh aqueous solutions are routinely used to remove a wide variety of contaminants, including metals, organics, and particulate matter. These solutions, although extremely effective at producing clean surfaces, also oxidize and roughen the silicon wafer.[1] This cleaning-induced surface roughness is detrimental to the performance of microelectronic devices subsequently fabricated on the wafer.[2] For this reason, many industrial cleaning processes utilize another step—etching in a hydrofluoric-acid-based solution. Fluorine-based etchants remove the chemically-produced oxide and terminate the silicon surface with a monolayer of hydrogen. Dilute HF or buffered HF (BHF) solutions etch the underlying silicon at different rates based on their composition.[3]

Because of its industrial importance, BHF etching of silicon has been the subject of intense study. The dramatic *p*H dependence of BHF silicon etching was vividly demonstrated in 1989 by the discovery that *p*H-modified NH_4F/HF solutions at *p*H ≈ 9-10 produce atomically flat, monohydride-terminated Si(111) surfaces,[4] as shown by a single sharp Si-H stretching mode in the infrared absorbance spectrum. This high *p*H version of BHF is extremely anisotropic, preferentially etching defect sites much faster than {111}-terrace sites.[5-7] In contrast, Si(111) surfaces etched in *p*H 5 BHF are rough and have vibrational spectra characterized by a highly structured Si-H stretching region with many overlapping modes.[8] Subsequent infrared spectroscopic studies characterized the dependence of the etched Si(111) surface morphology on the *p*H of the BHF solution by examining stepped (111) surfaces.[9,10] Later work revealed that the *p*H-dependence of Si(111) morphologies etched in BHF is principally caused by unwanted side reactions that

dominate at low etch rates (*i.e.* low concentration of OH^-). For BHF at acidic *p*Hs, the concentration of OH^- becomes low enough that dissolved oxygen, $O_2(g)$, provides a competing oxidation pathway for the etching mechanism.[11] As a consequence, Si(111) surfaces etched in the presence of oxygen at *p*H 7.8 BHF are atomically flat but become rough and pitted after etching with *p*H < 6.0 BHF.

In spite of the almost exclusive use of Si(100) in the microelectronics industry, the *p*H dependence of BHF etching on the Si(100) surface has not been as extensively studied as on Si(111). Initial spectroscopic work by Chabal *et al.* on HF-etched Si(100)[8] was expanded to include surfaces etched in solutions at *p*H 2, 5, and 8[12], resulting in the widely accepted vibrational mode assignments for BHF-etched Si(100). These researchers assigned the prominent Si-H stretching bands to three regions: silicon monohydrides (~2070- 2090 cm^{-1}), dihydrides (~2104-2112 cm^{-1}), and trihydrides (~2125-2140 cm^{-1}).[8] Chabal *et al.* concluded that Si(100) surfaces were atomically rough at low *p*Hs, developing a more "structured roughness" of {111} facets on surfaces etched at higher *p*H. Later work by Niwano *et al.* reported the infrared spectra of HF- and NH_4F-etched Si(100).[13] After observing vibrational modes attributed to {111} facets, these researchers noted that etchants that produce atomically flat Si(111) do not produce flat Si(100). Graf *et al.* examined Si(100) surfaces etched in *p*H 5 and *p*H 8 BHF with high-resolution-electron-energy-loss spectroscopy (HREELS), concluding that the surface coverage of dihydrides decreases at lower *p*H with the formation of {111} facets.[14] The general consensus of these studies is that Si(100) surfaces etched in low *p*H BHF are atomically rough and become {111}-microfaceted with increasing etchant *p*H.

The detailed analysis of *p*H 7.8 $NH_4F(aq)$-etched Si(100) by Clark *et al.* overturned this accepted interpretation.[15] Etched surfaces observed with scanning tunneling microscopy (STM) were near-atomically flat, consisting primarily of rows of unstrained dihydrides alternating with rows of strained dihydrides. This result proved that *p*H 7.8

BHF does not inherently roughen Si(100) surfaces—provided that bubbles are removed during etching. Clark *et al.* also revised the accepted vibrational mode assignments by observing dihydride stretching modes in the regions previously attributed to monohydrides and trihydrides, among other differences.[15] As described in Chapter 3, Cartesian component analysis of the vibrational spectrum enabled a new mode assignment for NH_4F-etched Si(100). This improved understanding of the etched H/Si(100) surface structure and infrared spectrum enabled the study of the *p*H-dependence of BHF Si(100) etching reported in this chapter.

The strong *p*H-dependence of the Si(100) etch rate in BHF must also be considered during *p*H modification experiments in order to make valid conclusions about steady-state morphologies. For example, the etch rate of Si(100) in *p*H 7.8 NH_4F was previously determined to be 12.5 nm/min (~1.5 monolayers/s).[Ch. 3] In contrast, the etch rate of Si(100) in 50% HF (~*p*H 0) is only ~0.1 nm/min for short etch times of a few minutes.[16] Unfortunately, the *p*H-dependence of Si(100) etch rates in intermediate *p*H BHF solutions has not been extensively studied, but some insight can be gained from studies of Si(111) etching. Hu and Kerr reported the etch rates of Si(111) in 48% HF from *p*H 0 to 4, observing a roughly linear increase in the etch rate from 0.29 Å/min to 0.78 Å/min with respect to $[OH^-]$.[17] A linear dependence on $[OH^-]$ was also observed by Newton, who measured the etch rate of Si(111) in BHF between *p*H 6.7 and 9.4 to increase from 0.65 Å/min to 229.3 Å/min.[18] On this basis, it is reasonable to assume that the etch rate of Si(100) in BHF increases monotonically from ~1 Å/min at *p*H 0 to 12.5 nm/min at *p*H 7.8.

In the following, the *p*H-dependent morphology and chemical composition of BHF-etched Si(100) were examined by STM and infrared absorbance spectroscopy. To assess the etch time required to reach steady-state, the time-dependent morphology of Si(100) in *p*H 5 BHF (the lowest *p*H examined) was studied with vibrational spectroscopy.

The prominent Si-H stretching modes observed in the BHF-etched Si(100) surface spectra were then assigned using Cartesian component analysis. From this evidence, the morphology of Si(100) surfaces etched with high *p*H BHF ($11 \geq p\text{H} \geq 7.8$) are shown to have the same near-atomically-flat structure as surfaces etched in pure 40% $NH_4F(aq)$, whereas surfaces etched at lower *p*Hs ($7.8 > p\text{H} \geq 5$) have rougher morphologies. Dissolved oxygen is shown to have, at most, a minor effect on the steady-state morphologies.

6.1. Experimental

Samples for STM analysis were cut from single-side-polished, 0.5-10 Ω cm, nominally-flat wafers cut to within 0.9º of the (100) plane. Samples for infrared absorption experiments were prepared from double-side-polished, high-resistivity (>1000 Ω cm), nominally-flat Si(100) wafers or wafers miscut by 9º toward the [011] direction. The samples were oxidized in a tube furnace to produce a ~1000-Å-thick layer of SiO_2 and were then cleaned as described in Chapter 2.

For the variable duration etching experiments in *p*H 5 BHF, the thermal oxide layer was left intact to ensure a consistent starting surface. The clean samples were etched in buffered oxide etchant (BOE, *p*H 5, 5:1 by volume of 50% HF : 40% NH_4F, J.T. Baker) for durations between 75 s and 20 min.

For *p*H-modification experiments, the 1000-Å-thick thermal oxide layer was first removed by 75 s of etching in BOE, producing a H-terminated surface. Thermal oxide removal prior to etching was necessary because of the extremely slow SiO_2 etch rate at high *p*H. The H-terminated samples were then etched in either 40% NH_4F (*aq,* J.T. Baker), BOE, or a *p*H-modified solution of BHF. The *p*H-modified etchants were synthesized from BOE (*p*H 5) or NH_4F (*p*H 7.8) by gravimetrically adding either concentrated $HCl(aq)$ or $NH_4OH(aq)$ via a pre-cleaned glass Pasteur pipette. An etch time of 2 min was used unless otherwise noted. During etching, the sample was drawn through

the etchant/air interface at ~15 s intervals for BHF in the range of *p*H 7-9 and 10 s intervals for solutions with *p*H ≥ 9. This process dislodged hydrogen bubbles that formed during etching. Few or no bubbles were observed for etchants at *p*H ≤ 7, so withdrawal was not performed. The *p*H of the etchant was measured with *p*H-indicator strips (colorpHast, EMD Chemicals Inc.) after etching to avoid contamination.

For deoxygenation experiments, a small Teflon beaker of etchant was placed in a container that was purged with Ar(*g*) for 30-60 min before etching. An etching duration of 4 min in deoxygenated *p*H 5 BHF was used for a sample with an intact thermal oxide layer. For deoxygenated *p*H 7.8 BHF, the sample was H-terminated in a previous step, and an etch time of only 30 s was used to minimize bubble-induced roughening.

Infrared spectra and STM images for etched Si(100) surfaces were obtained as described in Chapter 2. The *p*- and *s*-polarized spectra were deconvoluted into the Cartesian components of the transition dipole moments, which produced a pair of in-plane, $\mu_{\|}^2$, and perpendicular polarized, μ_z^2/ε_z^2, spectra for each sample. For miscut samples, two pairs of *p*- and *s*-polarized spectra were collected in orthogonal directions. Deconvolution of these spectra into their Cartesian components yielded two orthogonal in-plane components, μ_x^2 and μ_y^2, and one perpendicular component, $\mu_z^2/!_z^2$.

6.2. Results

Several experiments were performed to analyze the steady-state morphologies of Si(100) etched in BHF. First, the time required to reach steady-state etching in the slowest etchant was determined with infrared spectroscopy. Next, the steady-state morphologies of surfaces etched in *p*H-modified BHF solutions were examined with infrared spectroscopy and STM. The effect of miscut surfaces and dissolved oxygen on the etch morphology was also studied.

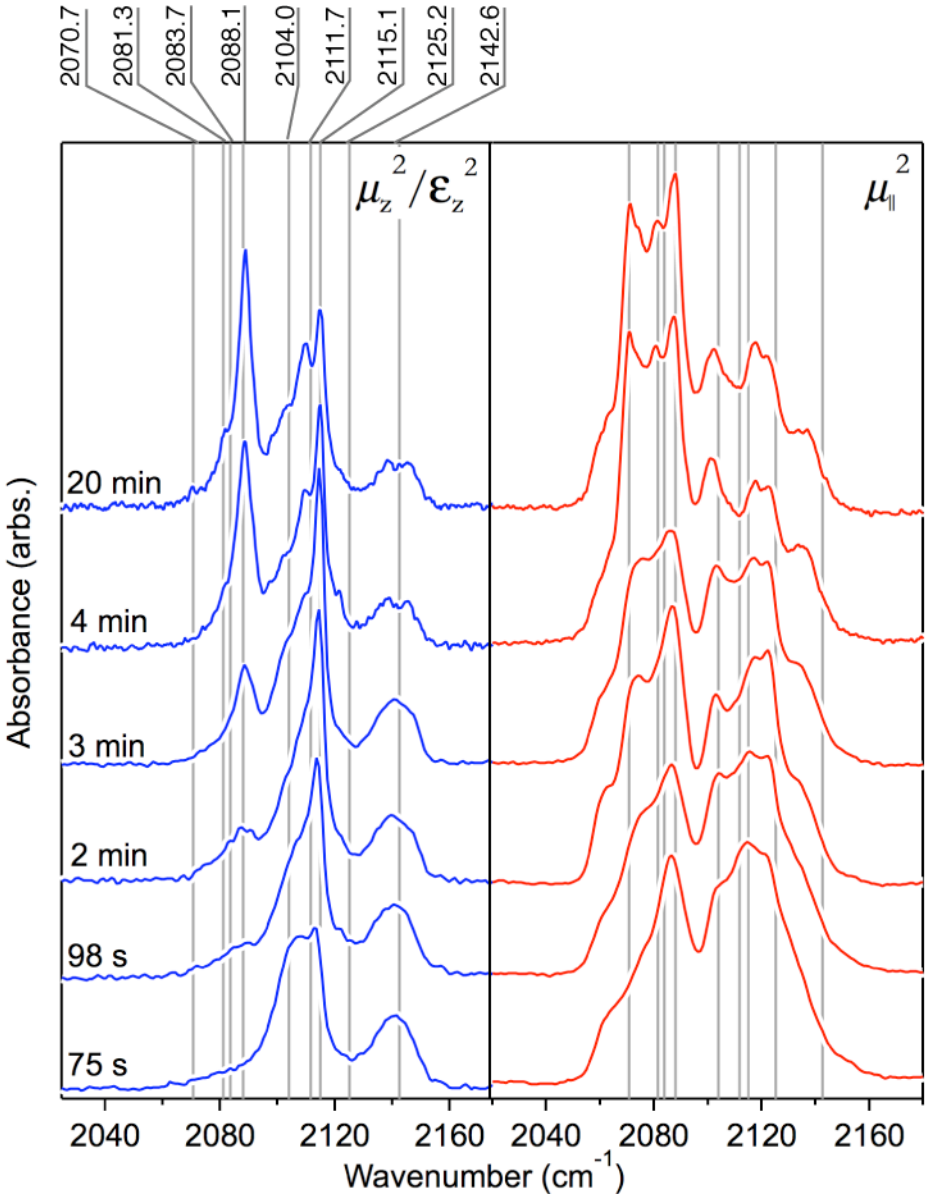

Figure 6.1. Cartesian components of the polarized infrared absorbance spectra for Si(100) surfaces etched in *p*H 5 BHF. The etching duration was measured from the moment of immersion for samples with ~1000 Å of thermal oxide. The grey lines mark the positions of stretching modes assigned in the text.

6.2.1. Determination of steady-state, BHF-etched Si(100) morphologies

To determine the etch time required to reach the steady-state Si(100) morphology in low *p*H BHF, surfaces were etched in *p*H 5 BHF for varying times and analyzed with

vibrational spectroscopy. Figure 6.1 shows the Si-H stretching region (~2050-2160 cm^{-1}) for surfaces etched between 75 s and 20 min, where the etching time, *t*, was measured *from the point of immersion in the etchant*. Because the 1000-Å-thick layer of thermal oxide on each sample was still intact, the first ~75 s of etching removed the oxide layer, as indicated by the sample becoming hydrophobic. After this period, the etchant removed silicon. Both spectral components underwent little change after 4 min of etching. For example, Fig. 6.2 overlays the spectra of the surfaces etched for 4 min and 20 min. The perpendicular mode at 2088.1 cm^{-1} was somewhat more intense for the 20 min etched surface, but no other significant differences were observed. The close similarity between the two spectra in Fig. 6.2 indicates that 4 min of etching was sufficient to reach the steady-state morphology on samples initially coated with 1000 Å thermal oxide.

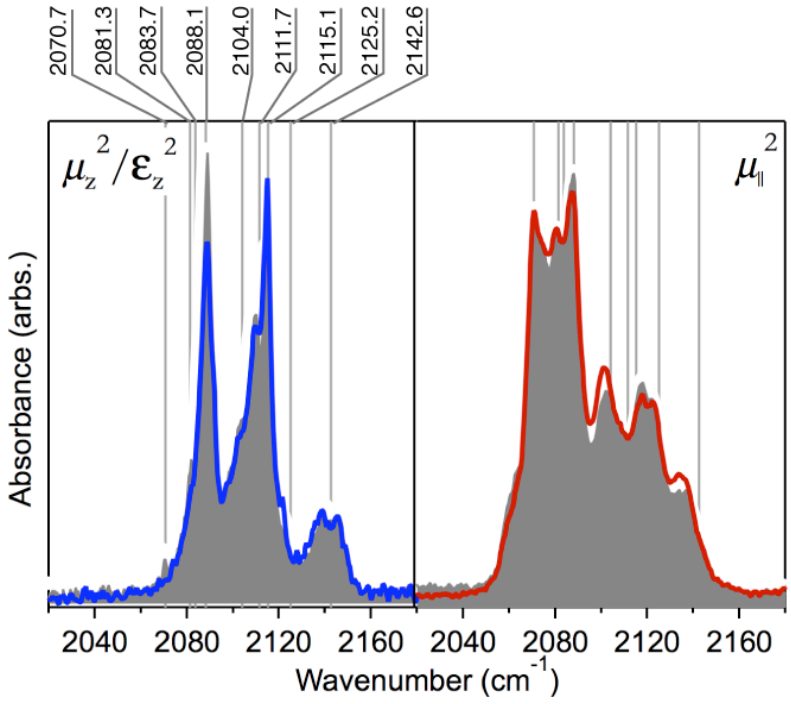

Figure 6.2. Comparison of the Cartesian components of the polarized infrared absorbance spectra for Si(100) surfaces etched for 4 min (traces) and 20 min (grey fill) in *p*H 5 BHF. The etching duration was measured from the moment of immersion for samples with ~1000 Å of thermal oxide. The grey lines mark the positions of stretching modes assigned in the text.

Similarly, initially H-terminated samples would reach steady-state after ~2.5 min of etching. The *p*- and *s*-polarized spectra (not shown) obtained after 4 min of etching were comparable to those reported by Dumas *et al.* for a Si(100) surface with a thin chemical oxide etched for 3 min in *p*H 5 BHF.[12]

Changes in the etch rate for high *p*H BHF were also considered. As discussed in Chapter 4, Si(100) etched in *p*H 7.8 NH_4F reaches steady-state in less than 15 s of etching. Because the silicon etch rate in BHF increases at higher concentrations of [OH^-]

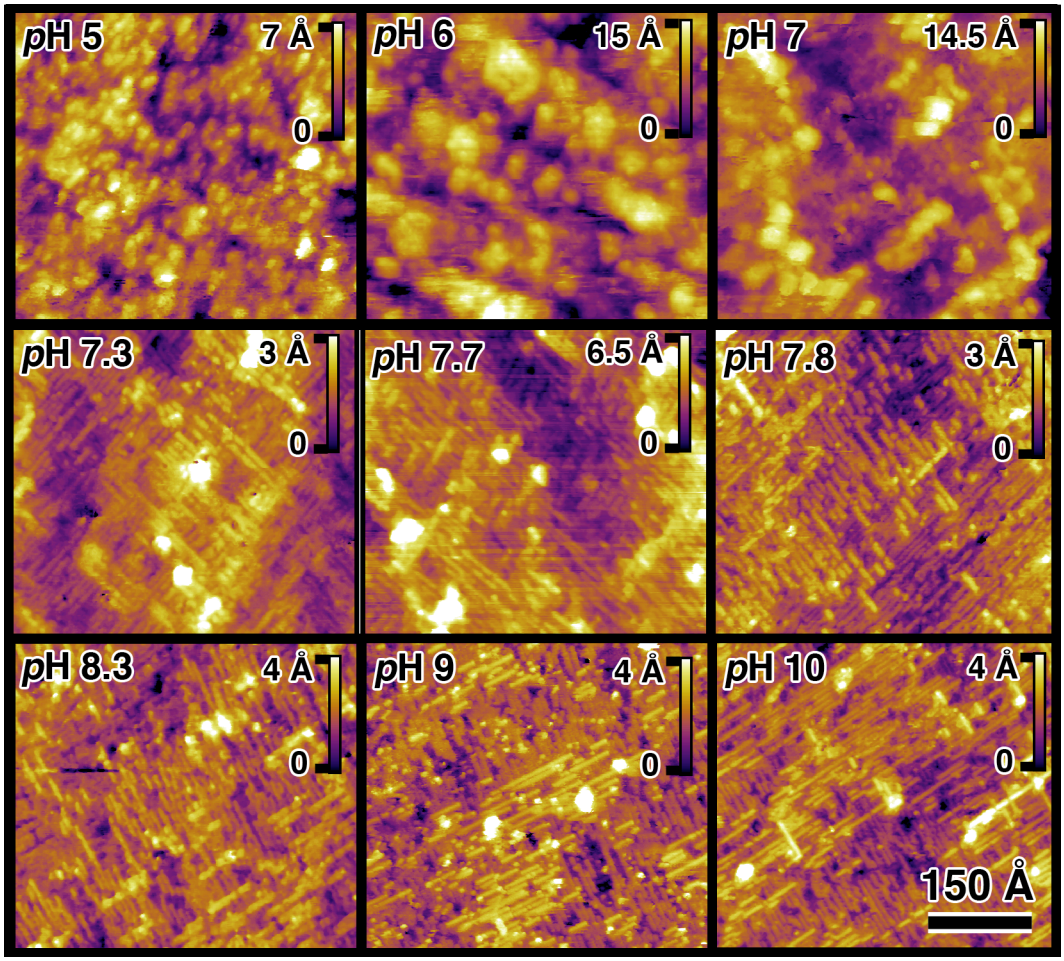

Figure 6.3. STM images of Si(100) surfaces etched for 2 min in *p*H-modified BHF. The samples were H-terminated (*i.e.* the thermal oxide was removed) prior to etching.

(*i.e.* *p*H),[18] etching durations longer than 15 s would be more than sufficient to reach steady-state for surfaces etched in BHF with *p*H ≥ 7.8.

These results show that etch times ≥ 2 min would be sufficient to reach steady-state for all *p*Hs of BHF studied here.

6.2.2. Steady-state morphology of Si(100) etched in *p*H-modified BHF

The steady-state morphology of Si(100) surfaces etched in BHF varied significantly with *p*H, as shown by the STM images in Fig. 6.3. Surfaces etched in *p*H 7.8 BHF (*i.e.* 40% NH_4F) had a near-atomically-flat "missing-row" morphology with long rows of dihydrides running parallel to the $[011]$ and $[01\bar{1}]$ directions, as discussed extensively in Chapter 3. The etched Si(100) morphologies produced by BHF at higher *p*Hs (up to *p*H 10) had morphologies that were virtually identical to the *p*H 7.8 NH_4F-produced surface, as illustrated by Fig. 6.3, except for the presence of a few small, high protrusions. These features are consistent with a low level of contaminants, perhaps from the (non-semiconductor-grade) reagents used to alter the *p*H. Surfaces etched with BHF below *p*H 7.8 (*i.e.* lower *p*H than NH_4F) were rougher than those etched at high *p*H. For example, the STM image in Fig. 6.3 of the surface etched in *p*H 7 BHF was nearly covered by hillocks. For surfaces etched in BHF at *p*H < 7, the surfaces were entirely covered with irregularly shaped hillocks whose size varied with *p*H. For example, the image of the *p*H 6 BHF-etched surface in Fig. 6.3 has significantly taller and wider hillocks than the surface etched in *p*H 5 BHF.

The chemical composition of the etched Si(100) surfaces was also dependent on *p*H, as shown by infrared absorbance spectroscopy. Strong absorbance bands were present in the Si-H stretching region (*i.e.* 2050–2165 cm^{-1}), and no C-H or O-H stretching modes were observed for any sample, indicating that clean, hydrogen-terminated surfaces were produced at all *p*Hs studied. The spectra of surfaces etched in BHF at *p*H 7.8 to 11 were virtually identical to those previously observed for Si(100) etched in pure

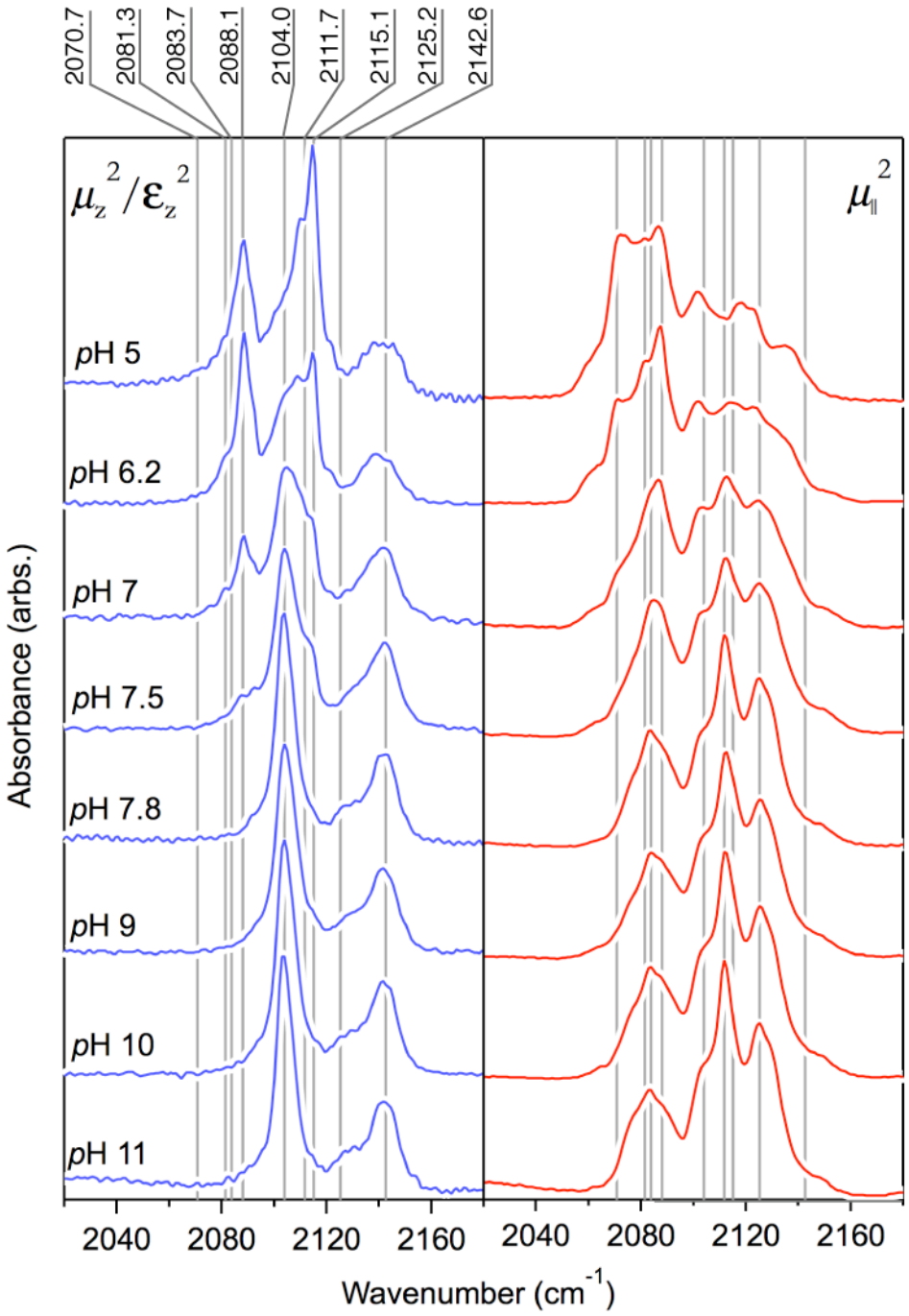

Figure 6.4. Cartesian components of the polarized infrared absorbance spectra for Si(100) surfaces etched for 2 min in *p*H-modified BHF. The samples were H-terminated prior to etching. The grey lines mark the positions of stretching modes assigned in the text.

40% $NH_4F(aq)$.[15, Ch. 3] Five prominent Si-H stretching modes were observed in this *p*H range, as shown by Fig. 6.4. The two modes at 2104.0 cm^{-1} and 2142.6 cm^{-1} were perpendicular polarized, and the modes at 2083.7 cm^{-1} and 2111.7 cm^{-1} were polarized in-plane. The fifth mode at 2125.2 cm^{-1} was primarily in-plane polarized with some perpendicular character. In general, the spectra of Si(100) surfaces etched at *p*Hs < 7.8 had more structure and more absorbance bands than surfaces etched at higher *p*H. As the *p*H was lowered from 7.8, four new modes developed in the spectra. Two of these modes were primarily perpendicular polarized: a sharp mode at 2115.1 cm^{-1} and a weak shoulder at 2138.5 cm^{-1}. One mode was strongly polarized in the (100) plane: the sharp mode at 2070.7 cm^{-1}. One mode was observed in both polarizations: the sharp mode at 2088.1 cm^{-1}. All of these modes increased in intensity as the *p*H was lowered. These observations are summarized in Table 6.1.

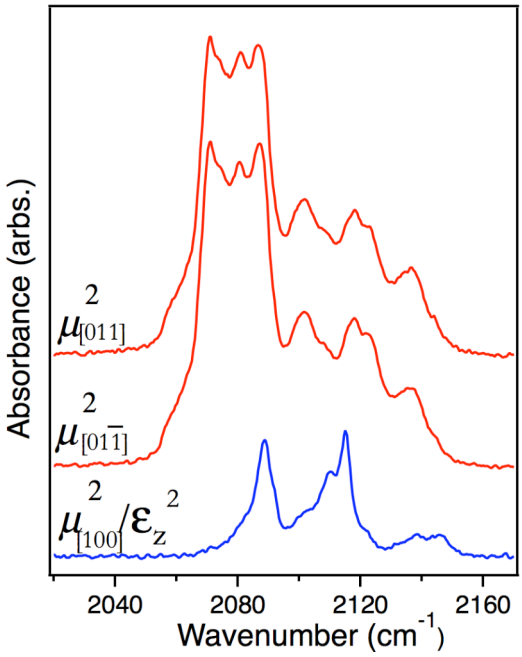

Figure 6.5. Cartesian components of the polarized infrared absorbance spectra for a Si(100) surface miscut by 9° toward the [011] direction that was etched for 4 min in *p*H 5 BHF, from which the thermal oxide had been previously removed. The two in-plane components (red) are nearly identical, indicating that the etch morphology was not affected by the miscut.

Miscut samples were used in an attempt to extract additional morphological information on Si(100) etched in low *p*H BHF. Previously, NH_4F-etching of miscut Si(100) samples spontaneously broke the fourfold rotational symmetry possessed by nominally-flat surfaces, as illustrated by the infrared spectra in Fig. 3.11. This effect was not observed for Si(100) etched in *p*H 5 BHF. Figure 6.5 shows the absorbance spectra of a Si(100) sample with a 9° miscut toward the [011] direction after etching in *p*H 5 BHF for 4 min. There are no significant differences between the two in-plane components in Fig. 6.5, indicating that the etch morphology retained macroscopic symmetry.

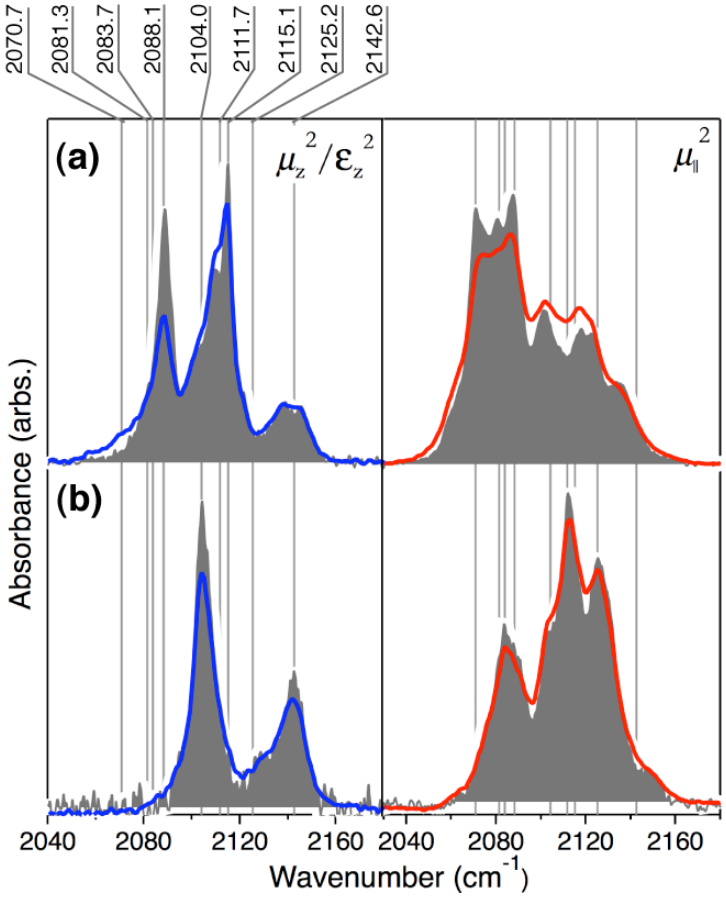

Figure 6.6. Cartesian components of polarized infrared absorbance spectra comparing morphologies etched in oxygenated etchant (grey fill) to morphologies etched in deoxygenated etchant (traces) for Si(100) surfaces etched in (a) *p*H 5 BHF for 4 min and (b) *p*H 7.8 BHF for 30 s. The grey lines mark the positions of stretching modes assigned in the text.

The effect of dissolved oxygen on the steady-state morphologies was also examined. Figure 6.6 compares the spectra of surfaces etched on the benchtop (*i.e.* oxygenated conditions) and in deoxygenated etchant. The spectra in Fig. 6.6(b) for *p*H 7.8 BHF show only small differences between the deoxygenated (trace) and oxygenated (grey fill) surfaces. Larger differences were observed for *p*H 5 BHF in Fig. 6.6(a), including reduced intensity of the 2088.1 cm^{-1} mode for the deoxygenated morphology; however, the same number of modes was observed in both oxygenated and deoxygenated spectra, and the overall spectral shape was comparable. The slight differences between morphologies produced in oxygenated and deoxygenated conditions indicate that dissolved oxygen had a minimal effect.

6.3. Discussion

The steady-state morphologies of Si(100) surfaces etched in *p*H ≥ 7.8 BHF solutions were substantially the same as the near-atomically-flat morphology observed on Si(100) surfaces etched in pure NH_4F. In contrast, the steady-state morphology became progressively rougher at lower *p*H. These changes were used as an aid to vibrational mode assignment and to elucidate the *p*H-dependent changes in the steady-state morphology.

6.3.1. Assignment of Si-H stretching modes on BHF-etched Si(100)

Table 6.1 lists the stretching modes observed on BHF-etched Si(100). The modes observed primarily on Si(100) etched with high *p*H BHF are discussed first, then those prominent after etching with low *p*H solutions.

The five vibrational modes that dominate the spectra of Si(100) surfaces etched in BHF at *p*Hs ≥ 7.8 were assigned in Chapter 3 from the study of highly miscut surfaces. These assignments are to the stretching modes of the "up" and "down" hydrogens of canted dihydrides (2142.6 cm^{-1} and 2083.7 cm^{-1}, respectively), symmetric and antisymmetric vibrations of unstrained dihydrides (2104.0 cm^{-1} and 2111.7 cm^{-1}, respectively), and the stretching mode of strained monohydrides (2125.2 cm^{-1}), which

have been discussed in the context of the missing-row morphology produced by $NH_4F(aq)$ etching of Si(100).[15, Ch.3]

Table 6.1. Mode assignments for nine Si-H stretching transitions on Si(100) surfaces etched with *p*H-modified BHF. The columns denoted || and ⊥ represent in-plane and perpendicular polarization, respectively, and "S" and "W" signify strong and weak mode intensity. The last two columns denote whether the mode is observed primarily at *p*Hs < 7.8 (**↓*p*H**) or at *p*Hs ≥ 7.8 (**↑*p*H**).

Stretching Vibration	Energy	||	⊥	↓*p*H	↑*p*H
{110}-monohydride coupled antisym. mode	2070.7	S		X	
{111}-monohydride mode	2081.3	W	W	X	
Strained canted dihydride "down" mode	2083.7	S			X
{110}-monohydride coupled sym. mode	2088.1	S	S	X	
Unstrained dihydride symmetric mode	2104.0		S		X
Unstrained dihydride antisymmetric mode	2111.7	S			X
Unassigned strained monohydride mode	2115.1		S	X	
Strained monohydride mode	2125.2	S	W		X
Strained canted dihydride "up" mode	2142.6		S		X

The narrow mode at 2081.3 cm^{-1} was assigned to {111}-microfacet monohydrides based on previous analyses of H/Si(111) surfaces as well as the observed polarization dependence. On atomically-flat Si(111) surfaces etched with *p*H ~9-10 BHF, the terrace monohydride stretch occurs at 2083.7 cm^{-1}.[4] The 2.4 cm^{-1} redshift observed here is attributed to reduced dipole-dipole coupling[19,20] due to the finite size of the {111} microfacets. In support of this assertion, the H/Si(111) terrace stretch redshifts by 1.0 cm^{-1} going from infinite planes to 20-Å-wide, semi-infinite terraces,[21] and redshifts of up to 4.6 cm^{-1} are observed for narrow terraces on vicinal Si(111) surfaces with strained step species.[22] Likewise, the {111}-facet monohydride mode on water-etched Si(100) occurs at 2081.3 cm^{-1} [23]— the same mode energy observed in these experiments. The {111}-microfacet monohydride stretch has significant in-plane and perpendicular

character on Si(100) as seen in Figs. 6.1 and 6.4, because {111} facets are oriented at 54.7° from the (100) surface normal.

By similar reasoning, the sharp modes at 2070.7 cm^{-1} and 2088.1 cm^{-1} were assigned to the coupled antisymmetric and symmetric stretches, respectively, of {110}-microfacet monohydrides. On flat NH_4F-etched H/Si(110), the coupled antisymmetric and symmetric monohydride stretches occur at 2070.2 cm^{-1} and 2089.1 cm^{-1}, respectively.[24] The observed blueshift of 0.5 cm^{-1} for the antisymmetric mode and redshift of 1.0 cm^{-1} for the symmetric mode are roughly comparable to the respective 1.8 cm^{-1} blueshift and 0.9 cm^{-1} redshift observed between flat H/Si(110) and the monohydride-terminated steps of $\langle 11\bar{2} \rangle$–miscut Si(111).[10] These shifts can also be explained in terms of reduced dipole-dipole coupling.[21] Because {110} facets are tilted by 45° from the (100) surface normal, the {110}-microfacet monohydride symmetric stretch has significant in-plane and perpendicular character on Si(100). Likewise by geometry, the {110}-microfacet monohydride antisymmetric stretch is polarized entirely in-plane on Si(100).

The very narrow, intense, perpendicularly polarized mode at 2115.1 cm^{-1} observed in Figs. 6.1 and 6.4 was challenging to assign. Previous researchers have assigned this mode to a number of different dihydride structures; however, these assignments are difficult to reconcile with the data. In the assessment of H_2O-etched Si(100) by Faggin *et al.*, the 2115.1 cm^{-1} mode was assigned to strained canted dihydrides,[23] which stands in contradiction to the assignment of the modes at 2083.7 cm^{-1} and 2142.6 cm^{-1}. After etching a Si(100) surface for 3 min in *p*H 5 BHF, Dumas *et al.* assigned a weak mode at 2115 cm^{-1} to the antisymmetric vibration of a "horizontal" dihydride on a {111} facet.[12] This assignment was based on the mode polarization and the assertion that antisymmetric stretches are often ~10 cm^{-1} higher than the corresponding symmetric stretch (which was assigned to a mode at 2104 cm^{-1}). Bjorkman *et al.* observed a strong absorbance at 2114 cm^{-1} after etching Si(100) surfaces in a range of HF/NH_4F mixtures and attributed

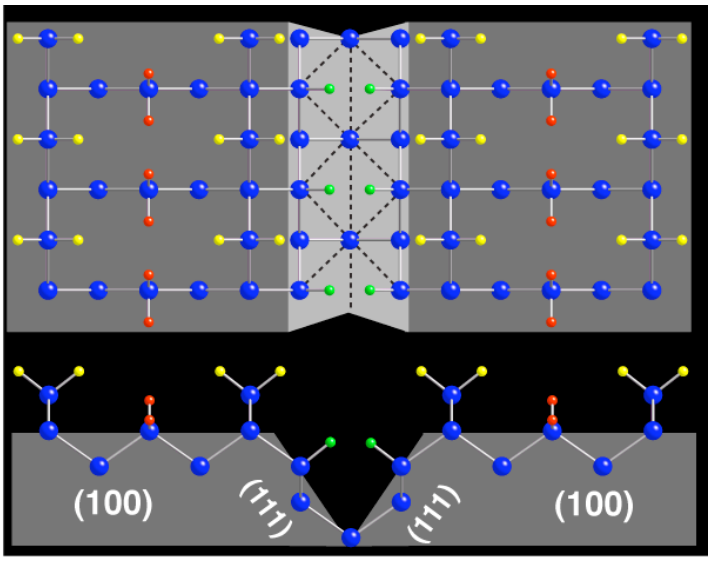

Figure 6.7. Illustration of an etched Si(100) surface with the "missing-row" morphology interrupted by a two-atom-layer-deep trench, which would be terminated by opposing monohydrides. The opposing monohydrides are created by the etching of canted dihydrides. Silicon atoms are in blue, unstrained dihydrides are in yellow, strained dihydrides are in red, and strained monohydrides are in green.

this mode to "asymmetric dihydrides,[25] and Kanaya *et al.* also assigned a mode at 2115 cm^{-1} to a dihydride for surfaces etched for long times (1-45 hr) in ultrapure water.[26] Based on the spectra in Figs. 6.1 and 6.4, the assignment of the 2115.1 cm^{-1} mode to a dihydride does not seem likely. No absorbance mode was correlated in intensity with the sharp mode at 2115.1 cm^{-1}, including the mode at 2104.0 cm^{-1} which was already assigned to the symmetric stretch of unstrained dihydrides. Although a weak in-plane transition at 2122 cm^{-1} may be correlated with the 2115.1 cm^{-1} mode, the 2122 cm^{-1} absorbance directly overlapped the strong mode assigned to strained monohydrides (2125.2 cm^{-1}) and was not consistently observed. Figure 6.7 illustrates another candidate structure that was ultimately rejected—opposing, highly strained monohydrides that are produced by the removal of strained, canted dihydrides. Because of their strong steric interactions, these strained monohydrides would have coupled symmetric and antisymmetric stretching modes, not just the single observed mode. Density functional theory (DFT) calculations

described in Chapter 5 predicted stretching frequencies for opposing monohydrides that were at least 5 cm^{-1} higher in energy than the predicted energy for the canted strained dihydride "up" hydrogen stretch.[Ch. 5] In contrast, the 2115.1 cm^{-1} mode is ~28 cm^{-1} below the observed "up" mode, thereby ruling out the assignment. As a result, the mode at 2115.1 cm^{-1} remains unassigned. Because the sharp transition at 2115.1 cm^{-1} was not correlated in intensity with another mode and occurred at a relatively high energy, the most likely assignment is to a strained monohydride of unknown geometry.

6.3.2. Morphology of Si(100) etched in *p*H-modified BHF

The steady-state morphology was independent of *p*H for $7.8 \leq$ *p*H ≤ 11. As shown in Fig. 6.4, the infrared spectra for surfaces etched with BHF in this *p*H range were identical. This invariance is confirmed by the STM images in Fig. 6.3, which show that BHF at *p*H 7.8-10 produce near-atomically-flat, "missing-row" morphologies.

In contrast, microfaceted hillocks developed on surfaces etched in solutions at *p*Hs < 7.8. As the *p*H was lowered from 7.8, the hillocks covered an increasing fraction of the surface, but did not grow monotonically in size. This transformation was most apparent in the infrared spectra. On Si(100), microfaceted hillocks are bounded by {111} and {110} facets, as illustrated by the sketches in Fig. 6.8. These facets have sharp, distinctive Si–H stretch modes at 2081.3 cm^{-1} for {111}-facet monohydrides, and at 2070.7 cm^{-1} and 2088.1 cm^{-1} for {110}-facet monohydrides. All three of these absorbance modes are clearly observed in the spectra of surfaces etched at *p*H 5 and *p*H 6.2 as seen in Fig. 6.4, indicating substantial hillock formation. In the case of the *p*H 7 BHF-etched surface, only the {110}-monohydride symmetric stretch mode at 2088.1 cm^{-1} was visible. At *p*H 7.5—only a few tenths of a *p*H unit lower than *p*H 7.8—the perpendicular component of the BHF-etched surface spectrum in Fig. 6.4 had a shoulder at 2088.1 cm^{-1}, indicating a small amount of microfaceting. Consistent with this interpretation, the modes

corresponding to the near-atomically flat surface also decreased in intensity as the *p*H was lowered from 7.8.

Hillock formation at low *p*Hs was confirmed by STM. For example, only a few hillocks were observed on the surface etched at *p*H 7.3 in Fig. 6.3. The total number of hillocks increased with decreasing *p*H as the *p*H was lowered past 7.3.

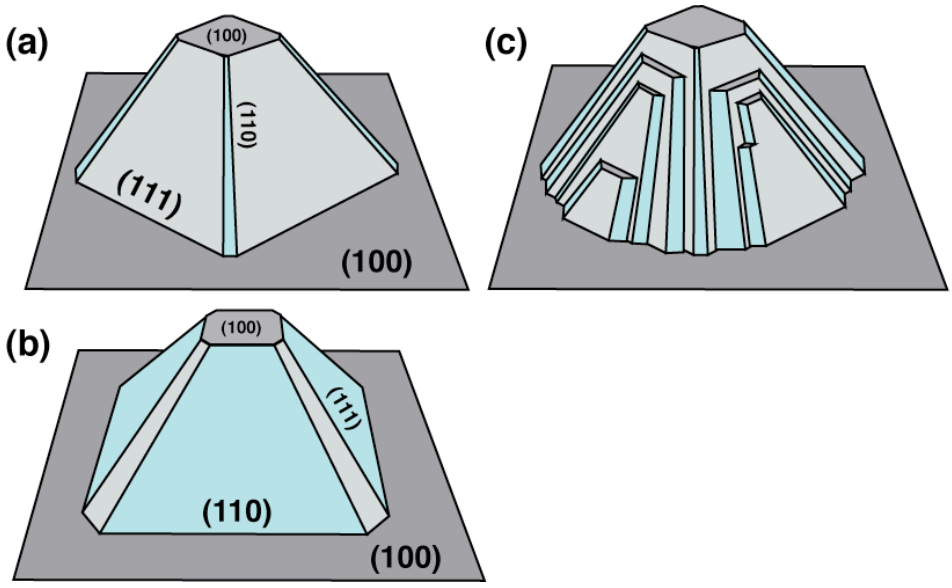

Figure 6.8. Illustration of three possible hillock morphologies on Si(100) surfaces, with (100) surfaces drawn in dark grey, {111} facets in light grey, and {110} facets in light blue. The flat-topped pyramidal hillock in (a) has primarily {111}-faceted sides, whereas the hillock in (b) has primarily {110}-faceted sides. The rounded hillock in (c) has significant areas of both {111} and {110} facets.

The infrared absorbance spectra are consistent with the formation of somewhat rounded, microfaceted hillocks consisting of {110} majority faces and {111} minority faces as sketched in Fig. 6.8(c). Figure 6.4 shows that the {110}-microfacet monohydride modes (2070.7 cm^{-1} and 2088.1 cm^{-1}) are much more intense than the {111}-microfacet monohydride mode (2081.3 cm^{-1})—opposite of what would be expected for the primarily {111}-faceted hillock in Fig. 6.8(a). In contrast, the hillocks depicted in Fig. 6.8(b) and (c)

both have a higher proportion of {110}-facet monohydrides. The absence of discrete facets or a pronounced squarish habit in the STM images in Fig. 6.3 suggested that the rounded hillock depicted in Fig. 6.8(c) is closest to the actual structure.

Previous studies of the *p*H dependence of BHF etching concluded that high *p*H solutions produce rougher Si(100) surfaces, in part by the formation of {111} microfacets.[12,13] This study reached the opposite conclusion: Si(100) surfaces etched with BHF at *p*Hs ≥ 7.8 were near-atomically smooth, whereas surfaces etched at *p*Hs < 7.8 developed hillocks that increased in surface coverage for lower *p*Hs. In this work, microfaceted hillocks were only observed below *p*H 7.8. These rounded hillocks were dominated by {110} facets and had only a minor {111} component, in contrast to the primarily {111}-microfaceted hillocks observed on other etched surfaces. For example, water-etched Si(100) has square-shaped faceted hillocks and vibrational spectra with a more intense {111}-facet monohydride mode[23] than the BHF-etched surface spectra in Fig. 6.4. In addition, some buffered systems (*e.g.,* potassium phosphate, tetramethylammonium phosphate) at near-neutral *p*Hs produce virtually perfect {111}-faceted pyramids on Si(100) after several hours of etching.[27]

6.3.3. *p*H-dependence of the BHF Si(100) etching mechanism

The accepted mechanism for silicon etching in pure NH_4F consists of a slow (rate-limiting) oxidation reaction by OH^- followed by fast removal of the oxidized site by HF:[28]

$$\equiv Si{-}H + OH^-(aq) + H_2O(l) \rightarrow \equiv Si{-}OH + H_2(g) + OH^-(aq) \qquad \text{(oxidation)}$$

$$(\equiv Si)_3Si{-}OH + 3\,HF(aq) + H_2O(l) \rightarrow 3(\equiv Si{-}H) + SiF_3OH(aq) \qquad \text{(etching)}$$

This mechanism is consistent with the increased hydrogen bubble formation, a rough visual indicator of etch rate, observed in higher *p*H solutions as well as the complete H-termination of the surfaces. Nevertheless, the *p*H-dependent morphology of BHF-etched Si(100) raises questions about the validity of this reaction mechanism. Surfaces etched

with BHF at *p*H ≥ 7.8 were characterized by a near-atomically flat missing-row morphology, yet a sharp transition to rougher surface structures was observed at lower *p*Hs. What is the chemical origin of this morphological transition?

In contrast to BHF etching of Si(111), this transition cannot be explained by dissolved O_2, as this impurity had a negligible effect on the steady-state morphology of Si(100) etched in BHF at either high (*p*H 7.8) or low *p*H (*p*H 5). Although some differences in the spectra of surfaces etched in oxygenated and deoxygenated BHF were observed (Fig. 6.6), the dissimilarities were small and inconsistent with significant morphological changes. In contrast, dissolved O_2 nucleates etch pits on flat Si(111) terraces,[29] producing dramatically roughened morphologies for Si(111) surfaces etched in BHF at *p*Hs < 6.0.[11] The difference in O_2 sensistivity between Si(111) and Si(100) is most likely explained by the much faster etch rate of Si(100). The insensitivity of the steady-state morphology to dissolved O_2 suggests that oxidation by O_2 is not competitive with oxidation by OH^-, at least for *p*Hs ≥ 5.

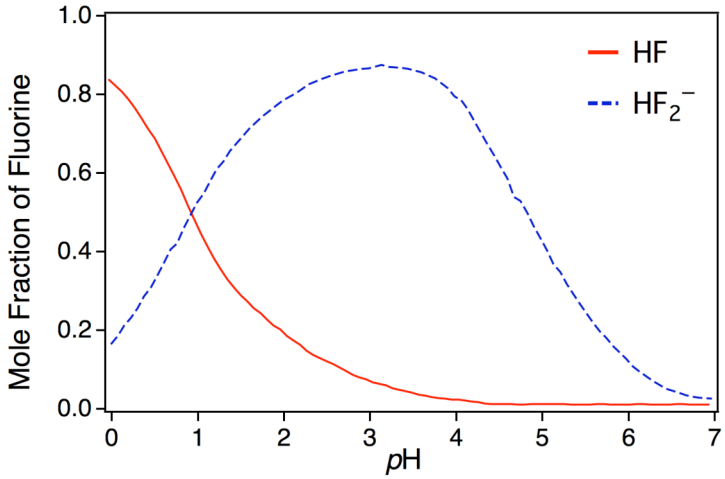

Figure 6.9. Mole fraction of fluorine as HF and HF_2^- for 15 M total [F], as calculated by Judge (Ref. 30).

The *p*H-dependence of the fluorine species in BHF may explain the morphological *p*H-dependence of Si(100). In these experiments, the total amount of fluorine was kept approximately constant while the concentration of OH^- was varied by the addition of small amounts of acid or base; however, the fluorine species present in the BHF solution change with the etchant *p*H. Figure 6.9 shows the relative concentration of fluorine species at *p*Hs < 7. The concentration of HF_2^- becomes significant at *p*Hs lower than 7 and increases to a maximum at *p*H ~3, whereas HF increases in concentration below *p*H 4. These fluorine species are known to have different reactivities towards oxidized silicon. For example, HF_2^- dissolves SiO_2 four times faster than HF at 23ºC.[30] The differing reactivities of fluorine species toward oxidized surface sites may account for the *p*H-dependent morphology (*i.e.* increasing roughness) of Si(100) etched in BHF at *p*Hs < 7. In contrast, almost all of the fluorine in BHF at *p*Hs > 7 exists as the uncombined fluoride ion, F^-.[30] The negligible concentration of HF or HF_2^- at *p*Hs > 7 suggests that the second step of the etching mechanism (as written above) is not valid at high *p*H. In addition, oxidation is most likely not the rate-limiting step for high concentrations of $[OH^-]$. For example, Si(100) etched in 50% KOH (*p*H > 14) becomes hydrophilic (*i.e.* oxidized), whereas surfaces etched with KOH at *p*Hs ~7-11 are hydrophobic.[31] Therefore, the etching mechanism at high *p*H is more complicated than the two reactions written above and requires further study.

6.4. Conclusions

The effects of *p*H on the steady-state morphology of Si(100) etched in fluorine-based solutions were investigated with STM and infrared absorption spectroscopy. Although the etch rate of Si(100) in low *p*H BHF is extremely slow, the etched morphology reached steady-state within several minutes for *p*Hs between 5 and 11. Using Cartesian component analysis, new spectral assignments were made for the prominent Si-H stretching modes observed in the spectra of BHF-etched Si(100). Contrary to accepted

wisdom, near-atomically flat surfaces were produced by etching in BHF at *p*Hs ≥ 7.8—no evidence of {111}-faceting was observed under these conditions. The steady-state morphologies produced at high *p*H were the same as those produced in *p*H 7.8 NH_4F, displaying the characteristic missing-row morphology with rows of unstrained dihydrides alternating with strained dihydrides. In contrast, surfaces etched at *p*H < 7 were covered with microfaceted hillocks. These rounded hillocks were primarily {110}-faceted, with only a small proportion of {111} facets.

The morphological transition between rough (low *p*H) and smooth (high *p*H) regimes was not due to dissolved oxygen. Instead, *p*H-dependent changes in the reaction mechanism were proposed as a possible explanation for the transition.

REFERENCES

[1] Y. J. Chabal, G. S. Higashi, and R. J. Small, in *Handbook of Silicon Wafer Cleaning Technology*, 2nd ed., edited by K. A. Reinhardt and W. Kern (William Andrew Inc., 2008), p. 515-606.

[2] T. Ohmi, K. Kotani, A. Teramoto, and M. Miyashita, IEEE Electron Device Letters **12,** 652-654 (1991).

[3] W. Kern, in *Handbook of Silicon Wafer Cleaning Technology*, 2nd ed., edited by K. A. Reinhardt and W. Kern (William Andrew Inc., 2008), p. 3-92.

[4] G. S. Higashi, Y. J. Chabal, G. W. Trucks, and K. Raghavachari, Applied Physics Letters **56,** 656-658 (1990).

[5] J. Flidr, Y.-C. Huang, T. A. Newton, and M. A. Hines, Journal of Chemical Physics **108,** 5542-5553 (1998).

[6] H. Zhou, J. Fu, and R. M. Silver, Journal of Physical Chemistry C **111,** 3566-3574 (2007).

[7] H. Zhou, J. Fu, and R. M. Silver, Journal of Physical Chemistry B **109,** 23386-23394 (2005).

[8] Y. J. Chabal, G. S. Higashi, K. Raghavachari, and V. A. Burrows, Journal of Vacuum Science & Technology A: Vacuum, Surfaces, and Films **7,** 2104-2109 (1989).

[9] G. S. Higashi, R. S. Becker, Y. J. Chabal, and A. J. Becker, Applied Physics Letters **58,** 1656-1658 (1991).

[10] P. Jakob and Y. J. Chabal, Journal of Chemical Physics **95,** 2897-2909 (1991).

[11] S. P. Garcia, H. Bao, and M. A. Hines, Surface Science **541,** 252-261 (2003).

[12] P. Dumas, Y. J. Chabal, and P. Jakob, Surface Science **269/270,** 867-878 (1992).

[13] M. Niwano, Y. Takeda, Y. Ishibashi, K. Kurita, and N. Miyamoto, Journal of Applied Physics **71,** 5646-5649 (1992).

[14] D. Gräf, S. Bauer-Mayer, and A. Schnegg, Journal of Vacuum Science & Technology A: Vacuum, Surfaces, and Films **11,** 940-944 (1993).

[15] I. T. Clark, B. S. Aldinger, A. Gupta, and M. A. Hines, Journal of Physical Chemistry C **114,** 423-428 (2010).

[16] G. Willeke and K. Kellermann, Semiconductor Science and Technology **11,** 415-421 (1996).

[17] S. M. Hu and D. R. Kerr, Journal of the Electrochemical Society **114,** 414 (1967).

[18] T. A. Newton, Ph. D. Dissertation, Cornell University, 2000.

[19] P. Jakob, Y. J. Chabal, and K. Raghavachari, Chemical Physics Letters **187,** 325-333 (1991).

[20] T. A. Newton, J. A. Boiani, and M. A. Hines, Surface Science **430,** 67-79 (1999).

[21] P. Jakob, Y. J. Chabal, K. Kuhnke, and S. B. Christman, Surface Science **302,** 49-56 (1994).

[22] P. Jakob, Y. J. Chabal, K. Raghavachari, and S. B. Christman, Physical Review B **47,** 6839-6842 (1993).

[23] M. F. Faggin, S. K. Green, I. T. Clark, K. T. Queeney, and M. A. Hines, Journal of the American Chemical Society **128,** 11455-11462 (2006).

[24] I. T. Clark, B. S. Aldinger, A. Gupta, and M. A. Hines, Journal of Chemical Physics **128,** 144711-1 - 144711-9 (2008).

[25] C. H. Bjorkman, M. Fukuda, T. Yamazaki, S. Miyazaki, and M. Hirose, Japanese Journal of Applied Physics **34,** 722-726 (1995).

[26] H. Kanaya, K. Usuda, and K. Yamada, Applied Physics Letters **67,** 682-684 (1995).

[27] M. F. Faggin and M. A. Hines (unpublished work).

[28] M. A. Hines, International Reviews in Physical Chemistry **20,** 645-672 (2001).

[29] C. P. Wade and C. E. D. Chidsey, Applied Physics Letters **71,** 1679-1681 (1997).

[30] J. S. Judge, Journal of the Electrochemical Society **118,** 1772-1775 (1971).

[31] B. S. Aldinger, K. Hallman, and M. A. Hines (unpublished work).